FACULTY OF ENGINEERING AND ARCHITECTURE

Novel Lower-Cost System Design for High-Resolution Extended Axial Field-of-View Positron Emission Tomography

Maya Abi Akl

Doctoral dissertation submitted to obtain the academic degree of
Doctor of Biomedical Engineering

Supervisors

Prof. Stefaan Vandenberghe, PhD* - Prof. Othmane Bouhali, PhD**

* Department of Electronics and Information Systems
Faculty of Engineering and Architecture, Ghent University

** College of Engineering, Texas A&M University at Qatar, Qatar

December 2025

GHENT UNIVERSITY

ISBN 978-94-93464-92-6
NUR 954
Wettelijk depot: D/2025/10.500/152

Members of the Examination Board

Chair

Prof. Hennie De Schepper, PhD, Ghent University

Other members entitled to vote

Prof. Michel Koole, PhD, KU Leuven
Qiyu Peng, PhD, Shenzhen Bay Laboratory, China
Cédric Revel, PhD, Centre Hospitalier Universitaire de La Réunion, France
Prof. Donatienne Van Weehaeghe, PhD, Ghent University
Prof. Christian Vanhove, PhD, Ghent University

Supervisors

Prof. Stefaan Vandenberghe, PhD, Ghent University
Prof. Othmane Bouhali, PhD, Texas A&M University at Qatar, Qatar

Acknowledgements

"Trust in dreams, for in them is hidden the gate to eternity"

Khalil Gibran

Reaching the end of this long journey still feels a bit surreal. Each phase of my PhD brought its own challenges, but also countless moments of learning, progress and fulfillment. Starting my doctoral work remotely and part-time, while holding a full-time teaching job and being physically distant from our group except for brief visits, was undoubtedly intense. The COVID period only amplified these difficulties, as even those short visits stopped, and the time seemed to slip away amid unprecedented circumstances. Regaining momentum and eventually moving to Ghent was far from easy, but it turned out to be both rewarding and transformative. Looking back on these past years, I am fully aware that I wouldn't be writing this manuscript without the unwavering support of my promoters, my family, my friends and my colleagues.

First, I would like to thank my promotors, Stefaan Vandenberghe and Othmane Bouhali. **Stefaan**, thank you for not only giving me the opportunity to join your research group but also for your continuous support, understanding and guidance throughout every stage of this journey. I have learned so much from you: independence, critical thinking, efficiency, and decisiveness when needed. Most importantly, you reinforced that a thesis is meant to be completed, not perfected, a mindset that allowed me to move forward with confidence. You made my move to Ghent possible and remarkably smooth, and you helped make my time here truly enjoyable with your advice and recommendations about this beautiful city and country. Outside of work, our group felt like a family, and I am grateful for the many activities you organized that brought us all together. **Othmane**, my research journey after earning my Master's degree began with you. You gave me the opportunity to work with the CMS collaboration at CERN and created a research environment at

Texas A&M University at Qatar that kept me motivated, even when teaching sometimes felt repetitive and work-related challenges arose. I have truly enjoyed our scientific and social discussions. You introduced me to Stefaan, supported me throughout my PhD, and inspired me with your passion for science and research. The lessons I've learned from you are countless.

Second, I want to thank **Hennie** De Schepper and **Patrick** De Baets for chairing my PhD jury and guiding me through the process. I appreciate the jury members **Donatienne** Van Weehaeghe, **Cedric** Revel, **Qiyu** Peng, **Michel** Koole, and **Christian** Vanhove for taking the time to review my manuscript and for their valuable comments and feedback. I truly enjoyed the discussion during my internal defense.

I'm also grateful to the other professors whom I had the opportunity to get to know and interact with throughout this journey. **Roel**, we only had a brief chance to talk during my early visits to Ghent, and you had already left MEDISIP by the time I moved. Still, I'm glad we connected again. Your drive and the way you consistently build something successful before moving on to a new challenge is truly impressive. **Chris**, a different kind of thank you this time! Even though you weren't directly involved in my research at the start and we didn't know each other well initially, I appreciate having come here and gotten to know you. You've always been available to discuss, help, and offer perspective. Your positivity made a difference during challenging times. **Pieter** and **Vincent**, I enjoyed learning from the courses I took with you, especially as someone with a background in Physics. **Patrick**, **An**, and **Charlotte**, it was a pleasure getting to know you and conversing with you about different topics, whether during team-building activities, over a lunch at the UZ resto, or simply in the hallways of Block B. It is a pity we didn't share the same office space in the past year, but you always managed to organize something that brought everyone from MEDISIP and BioMMedA together, and I truly appreciated that. **Brent**, even though we didn't have many scientific interactions, I always valued our conversations about Lebanon. I was often impressed by how much you knew, sometimes even more than I did!

From the University of Pennsylvania, I would like to thank Joel Karp, Margaret Daube-Witherspoon and Varsha Viswanath. **Joel**, getting to know you and learning from you has been a true privilege. Your depth of knowledge and the clarity with which you share it make every conversation engaging and inspiring. Thank you for your comments,

feedback, and advice over the years. You were also an exceptional host during my research visit to UPenn, a stay that was unfortunately cut short because of the COVID pandemic. **Margaret**, I always knew you were just an email away, and your quick responses and willingness to help made a real difference. I enjoyed getting to know you better during my visit to UPenn. **Varsha**, you also made my research stay smooth and productive, and working with you was genuinely motivating.

Saskia, thank you for all your help with the administrative work and arrangements. I enjoyed our conversations back when we were still in Block B; they always added a nice touch to the day. **Jurgen**, I used to only catch a glimpse of you during my short visits, but it wasn't until I moved to Ghent that I realized you're the person I can rely on when a technical issue arises. I still remember the mattentaart you once brought to the office; it was the best I've ever had!

Karel, we first met at the MIC conference in Manchester and later at the FTMI in Valencia, where our conversations somehow shifted to various topics, with Qatar frequently coming up. I'm glad you've been working with MEDISIP almost every Friday; it has helped us connect better. Your passion for cycling is impressive-truly that of a typical Gentenaar!

Nadia, our first encounter at the PSMR conference in Elba felt familiar, as though we had known each other for years. Talking with you has always been comforting and genuinely enjoyable. You also helped make my move to Ghent smoother, and I am grateful that living here has allowed me to get to know you better and see you more often. Hearing how deeply you care for your patients, how dedicated you are to your work, and how gracefully you manage so many responsibilities has been truly inspiring. I am lucky and proud to call you a friend.

To my colleagues and friends: **Jens**, my experience in the office would have not been the same without you. From our scientific discussions in which you made complex topics seem simple and smooth, and everything I learned from you, to all the laughter we shared; you made my time in the office memorable. I will always look back on it with a wide smile. **Florence**, I still remember our first meeting: I was visiting, you were a Master's student, and we connected instantly. It felt as though I had known you for years. I'm grateful that our long voice notes (podcasts) turned into regular face-to-face interactions and working with you has

been a real pleasure. Thank you for all the memories in the office, across Ghent and beyond-from jogging, tennis, and basketball to our conference trips. You always brought energy and warmth. **Boris**, you've been a wonderful colleague. I enjoyed our research-related discussions and the last-minute exchanges of feedback on submissions. You've also become a great friend and tennis buddy! I look forward to more practice sessions together. **Rabia**, even though our projects didn't overlap much, and we didn't work closely together, thank you for always offering help and recommending great food spots around Ghent. **Thibault**, it was fun to exchange glances whenever we heard strange noises in the office. I also enjoyed teaming up with you in tennis matches. **Melissa**, you're so much fun to be around. Thank you for organizing the MEDISIP meetings and for sharing your delicious baked cakes. I also admire how you care for all your plants sitting in our office. **Luna**, although we first met through the MEDISIP meetings that you joined remotely, it was nice meeting you in person at XEOS and hear more about the work you do there. **Elise**, I'm glad you joined MEDISIP for your PhD, as it allowed me to get to know you better. I enjoyed our quiet morning conversations when we were the only ones in the office. I wish you all the best with your PhD, I'm sure your work will be nothing short of excellence. **Robine**, although we only shared the office for a few months, I loved having a coffee buddy. Talking with you was always easy and refreshing. I would always wonder how you sit in short sleeves in the office while I was wrapped in layers! I wish you all the best on your journey. **Charlotte**, once a colleague and now a dear friend, your positive energy could brighten the entire fifth floor in Block B the moment you walked in. I'm grateful that we still make time to meet each month. Our moments together always fly by, filled with laughter, warmth and lightness. **Sara**, now I see why Chris calls you "Toppy". Your energy and efficiency are really impressive. I'm glad you joined the Infinity Lab around the same time I was in the office. I've enjoyed our conversations and tennis matches, and I look forward to more. **Jens** (Mincke), even though our office encounters were few, we connected immediately. Our conversations, often about our kids, were always relatable and refreshing. I hope you're enjoying your new job and spending plenty of quality time with your family.

My former MEDISIP colleagues, whom I often confused with BioMMedA because you were always sitting together: **Emma**, **Jolan** and **Amir**, running into you in Block B or chatting in the kitchen was always a pleasant break. I really enjoyed talking with you. **Mariele**,

we didn't spend much time together because I was working remotely when I first started, but you were always welcoming whenever I visited. **Milan**, we rarely crossed paths in the office, especially since you were usually in a different office when I visited, but it was always fun to catch up during conferences and events. And **Paulo**, I'm glad we stayed in touch and that you managed to return to Belgium. If only you lived closer to Ghent, but now that I've finished my PhD, hopefully we'll have more time and opportunities to meet up. To my current BioMMedA colleagues: even though we didn't see each other often because we were in offices at opposite ends of the UZ campus, every conversation we had was easy and enjoyable. **Amith**, you've always brought fun and light energy to the office. Finishing our PhDs around the same time made the journey smoother. It's funny how you managed to be one day ahead of me for both the internal and public defenses. Thank you for being that special friend.

I also want to thank my former colleagues in Qatar: **Yassine**, I learned so much from your guidance when I first started my research journey in this field. You have always been supportive and ready to help whenever needed. I wish you all the best in your future endeavors. **Zakaria**, it has been a pleasure working with you and exchanging ideas. I think of you every time I see of crow in Ghent. I remember how amazed you were by the number of them when you visited in the summer of 2024.

My dear friends around the world: Though not named individually, each of you knows the role you have played. Your presence and support have been felt even from afar. Thank you for your encouraging messages, your calls to check on me, and the ways you've made sure I was managing through every phase. I will always carry your support with me.

At the heart of this journey is my family, and to them I owe the deepest thanks. **Marie**, and **Manal**, I can never thank you enough for your care, love and support. You went above and beyond in every possible way. And to you **Chadi**, I cannot fully put into words how deeply grateful I am. To have walked this path with you, through every challenge, every low moment, and every joyful milestone has been one of the most meaningful parts of this journey. We truly faced it all together, just as we vowed when we chose to walk through life side by side. Your unconditional love and support kept me going during moments when everything felt overwhelming and uncertain, reminding me I was never alone. And to our dearest **Elena** and **Jad**, this book is dedicated to you.

You might not understand its pages just yet, but I hope that one day, when you are a little older, you will read it and feel proud of the journey that shaped it. You were very much part of it all! You have been my greatest source of motivation, and everything I do, I do with YOU in my heart.

Maya Abi Akl
December 2025, Gent

Summary

Positron emission tomography (PET) is an advanced molecular imaging technique that visualizes physiological and metabolic processes within the human body. It is routinely used in oncology for cancer diagnosis, staging, monitoring of disease progression, and guiding treatment response. It also has widespread applications in neurology and cardiology. As global cases and mortality from cancer, as well as cardiovascular and neurological diseases, continue to rise, early and accurate detection has become increasingly essential for improving patient outcomes.

PET imaging relies on biologically relevant compounds labeled with positron-emitting radionuclides, most commonly ^{18}F-fluorodeoxyglucose (^{18}F-FDG) in oncological applications, which accumulates in tissues with high glucose metabolism, such as malignant tumors and enables their visualization. When a positron emitted by the tracer annihilates with an electron from the surrounding tissue, they produce two high-energy 511 keV photons traveling in nearly opposite directions. These photons are detected by an array of scintillation detectors surrounding the patient, and the recorded data are reconstructed into tomographic images showing the distribution of tracer activity. Image quality strongly depends on the number of detected photons: the higher the count, the better the resulting image. Increasing the injected dose or acquisition time can enhance image quality but also raise radiation exposure, impact patient comfort, and affect workflow efficiency. Producing high-quality images is the main, but not the only, focus for everyone involved in the PET imaging process. Radiologists and nuclear medicine physicians aim for maximum diagnostic accuracy, while patients prioritize comfort, safety, and shorter scan times. Hospitals seek high throughput, smaller footprint and efficient use of resources. Therefore, modern PET imaging involves an optimization challenge, balancing image quality, dose, scan duration, cost and throughput. Conventional PET scanners practically need at least 15 minutes per acquisition and yet produce images with

limited spatial resolution. Systems with longer axial field-of-view (AFOV) are still limited in resolution but offer greater sensitivity and faster throughput, but their high manufacturing and operational costs limit widespread clinical use. To overcome these challenges, this dissertation focuses on designing and evaluating affordable, high-resolution PET systems using monolithic detector technology. The work investigates new system geometries, simulation-based performance evaluation, and deep learning-based image enhancement to develop a PET system that delivers high performance, enhances accessibility of PET imaging and increases operational efficiency.

Chapter 2 establishes the foundational background, covering the relevant physics processes and detector instrumentation. It also discusses the characteristics and limitations of the collected data, along with the statistical reconstruction methods, thereby covering the entire pipeline from radioactive decay inside the body to the formation of clinical PET images.

Chapter 3 provides an overview of two major recent advances in detector technology: time-of-flight (TOF) and depth-of-interaction (DOI) measurements. These innovations provide additional information about the emission positions, which enhances lesion detectability, particularly for small or early-stage tumors. The chapter also discusses recent developments in scanner design, including long AFOV geometries and sparse PET configurations with inter-detector gaps, which are proposed as cost-effective alternatives to fully populated systems. Flat-panel designs are also reviewed. These are gaining attention as cost-effective and flexible options as they use fewer detectors than ring-based systems to achieve the same axial coverage. The Monte Carlo simulation framework used to model PET acquisitions is explained, along with the evaluation metrics based on NEMA standards. Adaptations of these standards in the context of unconventional geometries are discussed where relevant. Finally, a brief overview of recent deep learning applications in PET for denoising and artifact reduction is presented, setting the stage for their integration into the current work.

In Chapter 4, we propose two medium AFOV ring-based PET designs with monolithic LYSO detectors: a single 36 cm module and a 72 cm configuration formed by combining two such modules. We model them in GATE and evaluate their performance through simulation. This modular approach allows the AFOV to be adjusted, providing flexibility for different clinical applications. Monolithic detectors provide distinct advantages

over pixelated ones, including higher intrinsic spatial resolution and DOI capability, which help mitigate parallax errors in both the radial and axial directions, the latter being more pronounced in long AFOV systems. In this chapter, we assess the spatial resolution and image quality of the two designs and investigate how detector resolution performance translates at the system level, considering the fundamental limits imposed by positron range and photon non-collinearity. To further extend the AFOV, we introduce a design variant that incorporates detector gaps arranged in a checkered pattern, effectively doubling the axial length to 145 cm without increasing detector count. The gaps allow reconfiguration into pediatric mode, by reducing the system diameter and thus moving the detectors closer together. For this configuration, we evaluate how the increased solid angle coverage impacts system sensitivity. For the two main compact designs, the most notable outcome is the uniform sub-2 mm spatial resolution achieved across the entire FOV, made possible by the DOI-capable monolithic detectors. Additionally, we show that sensitivity scales with axial extent. Some limitations are encountered in the reconstruction software used, highlighting the need for software optimization. Therefore, in the following chapters, we adopt a different iterative reconstruction framework that allows more controlled and reliable tuning of reconstruction parameters and sensitivity correction.

In Chapter 5, we address the limitations of the previous chapter and take the optimization of PET system design a step further by aiming not only for high sensitivity, spatial resolution, and performance, but also for affordability and throughput. The chapter introduces the **Walk-Through PET (WT-PET)** concept, upon which two flat-panel configurations are modeled and evaluated: a long flat panel (L-FP) design with an AFOV of 106 cm, sufficient to cover the brain and torso, and a sparse medium-AFOV flat panel (SpM-FP) design featuring a reduced AFOV of 60 cm (a little over half that of the L-FP) arranged with axial gaps. This configuration reduces the number of detectors by a factor of 2.5 compared to the L-FP. The SpM-FP requires limited panel translation to sequentially image the brain and torso. The main motivation for these designs is cost reduction by fewer detectors arranged in a flat-panel geometry rather than a conventional ring-based one. With vertically oriented panels spaced 50 cm apart, the patient can simply step between them for a quick scan, thereby increasing throughput. The same monolithic LYSO detectors used in Chapter 4 are employed, offering DOI capability, an essential feature given the close detector proximity to

the patient. However, the flat-panel geometry inherently limits angular coverage, leading to elongation artifacts in the direction perpendicular to the panels due to the missing lines of response (LORs). Nonetheless, previous studies indicate that systems with good TOF performance can tolerate partial angular sampling. The monolithic LYSO detectors are expected to achieve a TOF resolution of around 300 ps (based on measurements reported in the literature). Performance evaluation is conducted according to NEMA standards with adaptations suitable for flat-panel geometry and extended AFOV. Image reconstruction is performed using software specifically optimized for the WT-PET geometry, which incorporates sensitivity and attenuation corrections, as well as point spread function (PSF) modeling to account for the system's intrinsic resolution. The limitations encountered in Chapter 4 were effectively resolved in this stage of the work. Both designs achieve uniform sub-2 mm spatial resolution in the directions parallel to the panels and an average of 3 mm in the perpendicular direction due to limited-angle effects. The SpM-FP demonstrates cost-efficiency, estimated to be roughly 30% less expensive than the PET component of the Siemens Biograph Vision 600, while maintaining excellent image quality and a stable noise profile minimally affected by the panel gaps. Good quality IQ and XCAT phantom images are obtained with three-minute scans. Despite its limited transverse coverage, the flat-panel design provides a broader axial sampling compared to cylindrical systems of similar AFOV, thanks to its closer panel spacing. The oblique LORs contribute valuable information along the perpendicular direction, helping to partially compensate for limited-angle artifacts.

In Chapter 6, the detection capabilities of the SpM-FP system are further examined using a digital high-resolution torso phantom with small spheres, down to 2 mm in diameter. This study assesses how the system's superior spatial resolution enhances the signal-to-noise ratio (SNR) and lesion contrast for a given number of detected counts. The results demonstrate that the SpM-FP can identify a 4-mm sphere at a sphere-to-background activity concentration ratio of 8:1 in less than two minutes. Owing to is high spatial resolution, the SpM-FP achieves this even at low count levels, whereas systems with lower resolution need significantly higher statistics to achieve similar detectability. Comparisons with the Siemens Biograph Vision 600 emphasize the critical role of TOF performance in improving lesion detectability and reducing limited-angle artifacts in flat-panel geometries.

Given the SpM-FP's expected 300 ps TOF resolution which does not fully mitigate the limited-angle artifacts, Chapter 7 introduces a deep learning-based approach to denoise and correct these artifacts. These issues mainly result from short acquisition times and the side gaps of the flat-panel geometry, which restrict angular sampling in the transverse direction. Building on previous work by our group, a 2D convolutional neural network (CNN) is trained on data from 30 patients from the *Ultra Low Dose Challenge*, using PET images acquired on the Siemens Biograph Vision Quadra as ground truth. The SpM-FP reconstructed images from GATE simulated data, serve as input, while the actual Quadra images serve as targets. The trained model effectively reduces noise and mitigates limited-angle artifacts in reconstructed images. However, some anatomical details, especially in the torso and brain regions, appeared slightly blurred compared to the reference images. Future improvements include extending the model to 3D CNNs for more spatial information, and expanding the training dataset to include more diverse patient cases, particularly those with malignancies.

Considering the entire PET image pipeline, expanding the AFOV and using DOI-capable monolithic detectors must be paired with design optimization to ensure cost-effectiveness and clinical practicality. The SpM-FP, combined with deep learning-based correction, emerges as a promising alternative to existing long-AFOV PET systems offering superior resolution, enhanced sensitivity, affordability, and higher patient throughput. With the future directions outlined in the concluding chapter, the SpM-FP concept represents a step toward a new generation of accessible, high-performance PET systems, bridging the gap between technological innovation and clinical application.

Samenvatting

Positronemissietomografie (PET) is een geavanceerde moleculaire beeldvormingstechniek waarmee fysiologische en metabole processen in het menselijk lichaam in kaart worden gebracht. Deze techniek wordt veelvuldig gebruikt in de oncologie voor de diagnose van kanker, het vaststellen van het stadium van de ziekte, het volgen van het ziekteverloop en het sturen van de behandeling. Ook in de neurologie en cardiologie wordt deze techniek op grote schaal toegepast. Aangezien het aantal diagnoses en de mortaliteit geassocieerd met kanker blijft stijgen, net als deze van cardiovasculaire en neurologische aandoeningen, is vroegtijdige en nauwkeurige detectie essentieel geworden voor het verbeteren van de klinische uitkomsten voor patiënten.

PET-beeldvorming maakt gebruik van biologisch actieve moleculen die zijn gemerkt met positron-emitterende radionucliden. In oncologische toepassingen is ^{18}F-fluorodeoxyglucose (^{18}F-FDG) een veelgebruikte radiotracer, aangezien deze zich ophoopt in weefsels met een hoog glucosemetabolisme, zoals kwaadaardige tumoren, en deze zichtbaar maakt. Wanneer een positron wordt uitgezonden door de tracer en annihileert met een elektron uit het omliggende weefsel, worden twee hoogenergetische fotonen (511 keV) gegenereerd die in bijna tegengestelde richtingen voortbewegen. Deze fotonen worden gedetecteerd met behulp van scintillatiedetectoren die rondom de patiënt geplaatst worden, en de geregistreerde gegevens worden gereconstrueerd tot tomografische beelden die de verdeling van de traceractiviteit weergeven. De beeldkwaliteit hangt sterk af van het aantal gedetecteerde fotonen: hoe hoger het aantal, hoe beter het resulterende beeld. Het verhogen van de geïnjecteerde dosis of de acquisitietijd kan de beeldkwaliteit verbeteren, maar kan tegelijkertijd ook de blootstelling aan straling verhogen, het comfort van de patiënt beïnvloeden en de efficiëntie van de workflow aantasten. Het produceren van beelden van hoge kwaliteit is het belangrijkste, maar niet het enige aandachtspunt voor iedereen die betrokken is bij het PET-

beeldvormingsproces. Radiologen en nucleair geneeskundigen streven naar maximale diagnostische nauwkeurigheid, terwijl patiënten prioriteit geven aan comfort, veiligheid en kortere scantijden. Ziekenhuizen streven naar het scannen van een groot aantal patiënten per uur, systemen met een geringe omvang, en een efficiënt gebruik van middelen. Daarom brengt moderne PET-beeldvorming een optimalisatie-uitdaging met zich mee, waarbij een evenwicht moet worden gevonden tussen beeldkwaliteit, dosis, scantijd, kosten en doorvoer. Conventionele PET-scanners hebben praktisch gezien minstens 15 minuten per acquisitie nodig en produceren toch beelden met een beperkte ruimtelijke resolutie. Systemen met een langer axiaal gezichtsveld (axial field-of-view, AFOV) hebben nog steeds een beperkte resolutie, maar bieden een grotere gevoeligheid en een snellere doorvoer. Hun hoge productie- en operationele kosten beperken echter het wijdverbreide klinische gebruik ervan. Om deze uitdagingen het hoofd te bieden, richt dit proefschrift zich op het ontwerpen en evalueren van betaalbare PET-systemen met hoge resolutie die gebruikmaken van monolithische detectortechnologie. Het onderzoek richt zich op nieuwe systeemgeometrieën, simulatiegebaseerde prestatie-evaluatie en deep learning-gebaseerde beeldverbetering om een PET-systeem te ontwikkelen dat hoge prestaties levert, de toegankelijkheid van PET-beeldvorming verbetert en de operationele efficiëntie verhoogt.

Hoofdstuk 2 beschrijft het fundamentele kader en behandelt de relevante fysische processen en detectorinstrumentatie. Daarnaast worden ook de kenmerken en beperkingen van de verzamelde gegevense en statistische reconstructiemethoden besproken, zodat de volledige pijplijn van radioactief verval in het lichaam tot de vorming van klinische PET-beelden behandeld wordt.

Hoofdstuk 3 geeft een overzicht van twee belangrijke recente ontwikkelingen op het gebied van detectortechnologie: time-of-flight (TOF) en diepte-van-interactie (depth-of-interaction, DOI) metingen. Deze innovaties bieden aanvullende informatie over de emissieposities, waardoor laesies beter detecteerbaar zijn, met name voor tumoren in een vroeg stadium of met een beperkte grootte. Het hoofdstuk bespreekt ook recente ontwikkelingen in scannerontwerp, waaronder geometrieën met een lang AFOV en schaarse PET-configuraties met tussenruimtes tussen detectoren, die worden voorgesteld als kosteneffectieve alternatieven voor systemen met een volledige detectorbezetting. Ook ontwerpen op basis van vlakke panelen worden besproken. Deze krijgen steeds meer aandacht als kosteneffectieve en flexibele opties, omdat ze minder detectoren

gebruiken dan systemen gebaseerd op detectorringen om dezelfde axiale dekking te bereiken. Ook, het Monte Carlo-simulatiekader dat wordt gebruikt om PET-acquisities te modelleren, wordt uitgelegd, samen met de evaluatiemethodes op basis van NEMA-normen. Aanpassingen van deze normen in de context van onconventionele geometrieën worden waar relevant besproken. Ten slotte wordt een kort overzicht gegeven van recente deep learning-toepassingen in PET voor ruisonderdrukking en artefactreductie, waarmee de weg wordt vrijgemaakt voor de integratie ervan in het huidige werk.

In hoofdstuk 4 stellen we twee ringgebaseerde PET-ontwerpen voor met een gemiddeld gemiddelde axiale lengte op basis van monolithische LYSO-detectoren: een configuratie op basis van één enkele module met een lengte van 36 cm, en een configuratie die wordt gevormd door twee dergelijke modules te combineren. Deze worden gemodelleerd in GATE, en hun prestaties worden geëvalueerd door middel van simulaties. De modulaire aanpak staat toe het AFOV te herconfigureren, wat flexibiliteit biedt voor verschillende klinische toepassingen. Monolithische detectoren bieden duidelijke voordelen ten opzichte van gepixelde detectoren, waaronder een hogere intrinsieke ruimtelijke resolutie en DOI-capaciteit, die helpt om parallaxfouten in zowel de radiale als axiale richting te verminderen, waarbij de laatste meer uitgesproken zijn in systemen met een lang AFOV. In dit hoofdstuk beoordelen we de ruimtelijke resolutie en beeldkwaliteit van de twee ontwerpen en onderzoeken we hoe de resolutieprestaties van de detector zich vertalen naar het systeemniveau, rekening houdend met de fundamentele beperkingen verbonden aan het bereik van positronen en de niet-collineariteit van fotonen. Om het AFOV verder uit te breiden, introduceren we ook een ontwerpvariant met openingen tussen de detectoren die in een dambordpatroon zijn gerangschikt, waardoor de axiale lengte effectief wordt verdubbeld tot 145 cm zonder het aantal detectoren te verhogen. De openingen maken daarnaast ook herconfiguratie naar pediatrische modus mogelijk, waarbij de diameter van het systeem verkleint en de detectoren dichter bij elkaar komen. Voor deze configuratie evalueren we hoe de grotere dekking van de ruimtehoek de sensitiviteit van het systeem beïnvloedt. Voor de twee standaardconfiguraties ontwerpen is het meest opvallende resultaat dat een uniforme ruimtelijke resolutie wordt bereikt van minder dan 2 mm over het gehele gezichtsveld dankzij het gebruik van de DOI-compatibele monolithische detectoren, mogelijk gemaakt door de DOI-compatibele monolithische detectoren. Daarnaast laten we zien dat de gevoeligheid

evenredig is met de axiale omvang. Ten slotte constateren we enkele beperkingen in de gebruikte reconstructiesoftware, wat de noodzaak van software-optimalisatie onderstreept. Daarom hanteren we in de volgende hoofdstukken een ander iteratief reconstructiekader dat een meer gecontroleerde en betrouwbare afstemming van reconstructieparameters en sensitiviteitscorrectie mogelijk maakt.

In hoofdstuk 5 gaan we in op de beperkingen van het vorige hoofdstuk en gaan we nog een stap verder in het optimaliseren van het ontwerp van PET-systemen door niet alleen te streven naar hoge sensitiviteit, ruimtelijke resolutie en prestaties, maar ook naar betaalbaarheid en doorvoercapaciteit. In dit hoofdstuk wordt het **Walk-Through PET (WT-PET)** concept geïntroduceerd, op basis waarvan twee vlakkepaneelconfiguraties worden gemodelleerd en geëvalueerd: een lang ontwerp (long flat panel, L-FP) met een AFOV van 106 cm, voldoende om de hersenen en de romp te omvatten, en een schaarse medium-AFOV configuratie (sparse medium flat panel, SpM-FP) met een verminderd AFOV van 60 cm (iets meer dan de helft van die van de L-FP) met axiale tussenruimtes. Deze configuratie vermindert het aantal detectoren met een factor 2,5 in vergelijking met de L-FP. Deze SpM-FP vereist een beperkte paneelverplaatsing om achtereenvolgens de hersenen en de romp in beeld te brengen. De belangrijkste motivatie voor deze ontwerpen is kostenreductie aangezien minder detectoren nodig zijn in configuraties op basis van vlakke panelen dan conventionele ringvormige opstellingen. Dankzij de verticaal georiënteerde panelen op een afstand van 50 cm van elkaar kan de patiënt eenvoudigweg de scanner inlopen voor een snelle scan, waardoor de doorvoer wordt verhoogd. Er wordt gebruik gemaakt van dezelfde monolithische LYSO-detectoren als in hoofdstuk 4, die DOI-functionaliteit bieden, een essentiële eigenschap gezien de nabijheid van de detector tot de patiënt. De vlakkepaneelgeometrie beperkt echter inherent het interval van de bemonsterde hoeken, wat leidt tot verlengingsartefacten in de richting loodrecht op de panelen als gevolg van de ontbrekende responslijnen (lines of reponse, LORs). Niettemin wijzen eerdere studies uit dat systemen met goede TOF-prestaties gedeeltelijke hoekbemonstering kunnen tolereren. De monolithische LYSO-detectoren zullen naar verwachting een TOF-resolutie van ongeveer 300 ps bereiken (op basis van metingen die in de literatuur worden vermeld). De prestatie-evaluatie wordt uitgevoerd volgens NEMA-normen, met aanpassingen voor de evaluatie van systemen met een lang AFOV en een vlakkepaneelgeometrie. De beeldreconstructie wordt uitgevoerd met behulp van

software die specifiek is geoptimaliseerd voor de WT-PET-geometrie, waarin sensitiviteits- en attenuatiecorrecties en dempingscorrecties zijn opgenomen, evenals point spread function (PSF)-modellering om rekening te houden met de intrinsieke resolutie van het systeem. De beperkingen die in hoofdstuk 4 werden vastgesteld, werden in deze fase van het werk effectief opgelost. Beide ontwerpen bereiken een uniforme ruimtelijke resolutie van minder dan 2 mm in de richtingen parallel aan de panelen en gemiddeld 3 mm in de loodrechte richting, als gevolg van beperkte-hoekeffecten. De SpM-FP is kostenefficiënt en naar schatting ongeveer 30% goedkoper dan de PET-component van de Siemens Biograph Vision 600, terwijl de uitstekende beeldkwaliteit en het stabiele ruisprofiel behouden blijven, met een minimale invloed van de paneelopeningen. Met scans van drie minuten worden IQ- en XCAT-fantoombeelden van goede kwaliteit verkregen. Ondanks de beperkte transversale dekking biedt het vlakkepaneelontwerp een bredere axiale bemonstering in vergelijking met cilindrische systemen met een vergelijkbaar AFOV, dankzij de kleinere paneelafstand. De schuine LOR's leveren waardevolle informatie in de loodrechte richting, waardoor artefacten als gevolg van de beperkte hoekbemonstering gedeeltelijk worden gecompenseerd.

In hoofdstuk 6 worden de detectieprestaties van het SpM-FP-systeem verder onderzocht met behulp van een digitaal torsofantoom met hoge resolutie en kleine sferen met een diameter tot 2 mm. In deze studie wordt beoordeeld hoe de superieure ruimtelijke resolutie van het systeem de signaal-tot-ruisverhouding (signal-to-noise ratio, SNR) en het contrast van laesies voor een vast aantal meetwaarden verbetert. De resultaten tonen aan dat de SpM-FP een sfeer van 4 mm kan identificeren bij een activiteitsconcentratieverhouding tussen een laag aantal meetwaarden en achtergrond van 8:1 in minder dan twee minuten. Dankzij de hoge ruimtelijke resolutie bereikt de SpM-FP dit zelfs bij een laag aantal meetwaarden, terwijl systemen met een lagere resolutie aanzienlijk hogere statistieken nodig hebben om een vergelijkbare detecteerbaarheid te bereiken. Vergelijkingen met de Siemens Biograph Vision 600 benadrukken de cruciale rol van TOF-prestaties bij het verbeteren van de detecteerbaarheid van laesies en het verminderen van artefacten bij beperkte hoekbemonstering in vlakkepaneelgeometrieën.

Gezien de verwachte TOF-resolutie van 300 ps de beperkte-hoekartefacten van de SpM-FP niet volledig compenseert, wordt in hoofdstuk 7 een op deep learning gebaseerde aanpak geïntroduceerd om deze artefacten te verwijderen en te corrigeren. Deze problemen zijn voornamelijk

het gevolg van korte acquisitietijden en de zijdelingse openingen van de vlakkepaneelgeometrie, die de hoekbemonstering in de transversale richting beperken. Voortbouwend op eerder werk van onze groep, wordt een 2D-convolutionaal neuraal netwerk (CNN) getraind op basis van gegevens van 30 patiënten uit de *Ultra Low Dose Challenge*. Hierbij worden PET-beelden die werden verkregen met de Siemens Biograph Vision Quadra gebruikt als referentiewaarden. De SpM-FP reconstructies verkregen na GATE-simulatie dienen als invoer, terwijl de daadwerkelijke Quadra-beelden als doel dienen. Het getrainde model vermindert effectief ruis en beperkt artefacten geassocieerd met beperkte-hoekbemonstering in gereconstrueerde beelden. Sommige anatomische details, vooral in de romp en hersengebieden, leken echter enigszins wazig in vergelijking met de referentiebeelden. Mogelijke toekomstige verbeteringen omvatten onder meer het uitbreiden van het model naar 3D CNN's voor het bieden van meer ruimtelijke informatie, en het uitbreiden van de trainingsdataset met meer diverse patiëntgevallen, met name die met ziektebeelden.

Binnen het kader van de volledige PET-pijplijn, moet de moet de uitbreiding van het AFOV en het gebruik van DOI-compatibele monolithische detectoren gepaard gaan met ontwerpoptimalisatie om kosteneffectiviteit en klinische bruikbaarheid te garanderen. De SpM-FP, in combinatie met op deep learning gebaseerde correctie, komt naar voren als een veelbelovend alternatief voor bestaande PET-systemen met een lange-AFOV en biedt een superieure resolutie, verbeterde sensitiviteit, betaalbaarheid en een hogere doorvoer van patiënten. Met de toekomstige richtingen die in het slothoofdstuk worden geschetst, vertegenwoordigt het SpM-FP-concept een stap in de richting van een nieuwe generatie toegankelijke, hoogwaardige PET-systemen, die de kloof tussen technologische innovatie en klinische toepassing overbruggen.

List of Abbreviations

AFOV	axial field-of-view
AI	artificial intelligence
BGO	bismuth germanate
BMI	body mass index
BN	batch normalization
BV	background variability
CAE	convolutional autoencoder
CNN	convolutional neural network
CNR	contrast-to-noise ratio
CRC	contrast recovery coefficient
CT	computed tomography
CTR	coincidence time resolution
CTW	coincidence time window
DL	deep learning
DOI	depth-of-interaction
FBP	filtered-back-projection
FDG	fluorodeoxyglucose
FWHM	full width at half maximum
GAN	generative adversarial network
GATE	Geant4 Application for Tomographic Emission
HU	Hounsfield Units

IQ	image quality
LOR	line of response
LSO	lutetium oxyorthosilicate
LYSO	lutetium-yttrium oxyorthosilicate
MAE	mean absolute error
MC	Monte Carlo
MLEM	maximum likelihood expectation maximization
MRD	maximum ring difference
MRI	magnetic resonance imaging
MSE	mean squared error
NEMA	National Electrical Manufacturers Association
NLM	non-local means
OSEM	ordered subset expectation maximization
PDE	photon detection efficiency
PET	positron emission tomography
PMT	photomultiplier tube
PSF	point spread function
PVE	partial volume effect
QETIR	Quantitative Emission Tomography Iterative Reconstruction
ReLu	rectified linear unit
ROI	region of interest
SD	standard deviation
SiPM	silicon photomultiplier
SNR	signal-to-noise ratio
SPAD	single-photon avalanche diode
SPECT	single photon emission computed tomography

SPTR	single photon time resolution
SSS	single scatter simulation
STB	sphere-to-background
SUV	standardized uptake value
TOF	time-of-flight
VOI	volume of interest
WT-PET	Walk-Through PET

Contents

Chapter 1

Introduction

1.1 Context

This dissertation focuses on positron emission tomography (PET), a functional imaging technique widely used in nuclear medicine for applications in oncology, cardiology and neurology. In contrast to computed tomography (CT) and magnetic resonance imaging (MRI), which primarily provide anatomical information, PET offers unique insights into physiological and molecular processes such as metabolism, perfusion, and tumor activity. Alongside PET, single-photon emission computed tomography (SPECT) is also employed for molecular imaging; however, PET provides superior resolution and higher sensitivity.

The most commonly used tracer in PET is ^{18}F-fluorodeoxyglucose (^{18}F-FDG), a glucose analog that accumulates in tissues with high glucose metabolism. FDG uptake is typically elevated in the brain, myocardium, and bladder (where it is excreted), and most importantly, in malignant tumors. PET has therefore become an indispensable tool for diagnosing, staging, and monitoring treatment response in cancer, a disease that has become a leading cause of death worldwide. Moreover, PET plays an important role in the evaluation of cardiovascular and neurological diseases, both of which also account for a significant proportion of global mortality, broadening its clinical impact. Early detection and treatment significantly improve patient outcomes, highlighting the importance of ensuring global access to high-quality PET imaging.

Over the last three decades, PET has reached several milestones, including the transition to fully 3D acquisitions and advancements in detector technology and computational power. Recently, international

collaborations have led to the development of long axial field-of-view (AFOV) PET/CT scanners, also called total-body PET/CT systems. These scanners have significantly increased sensitivity compared to conventional systems, allowing for shorter scan times, lower radiopharmaceutical doses, and/or better image quality through a higher signal-to-noise ratio. Several long AFOV systems have been developed with axial lengths reaching up to 2 meters and time-of-flight (TOF) resolutions as low as 214 ps. Despite these advances, spatial resolution is still limited by the discrete pixelation of the scintillation crystals used and the cost of acquiring such large systems remains high.

Motivated by these challenges, this dissertation explores alternative, cost-effective PET system designs based on monolithic scintillation detectors. Monolithic crystals inherently provide superior intrinsic spatial resolution and depth-of-interaction (DOI) capabilities, offering a way to surpass the resolution limits of pixelated detectors. The designs feature medium axial fields-of-view that achieve higher sensitivity than conventional PET scanners while being more affordable than the large, expensive long-AFOV systems currently available. In this work, we evaluate the performance of several innovative PET geometries through simulations, analyze the trade-offs between cost, sensitivity, and resolution, and explore solutions to balance these factors. At the same time, we recognize that the unconventional geometries present their own challenges, which we aim to characterize and address throughout this thesis.

To guide this work, this dissertation addresses the following key research questions:

- How much improvement in spatial resolution can be achieved using monolithic detectors with intrinsic DOI capabilities and to what extent can this resolution advantage be leveraged to improve contrast recovery, detection of small lesions, and overall image quality under clinical-like conditions?
- To what extent can unconventional medium-AFOV geometries improve sensitivity compared to conventional clinical PET scanners?
- What performance trade-offs arise when jointly optimizing cost, sensitivity, and spatial resolution, and how can these be balanced to enable practical system implementation?
- What image-quality limitations result from the proposed geometries, and how can these be characterized and mitigated in reconstruction and through deep learning-based methods?

1.2 Outline

Chapter 2 covers the basics of PET imaging, starting with the underlying physics processes, including radioactive decay and how radiation interacts with matter to produce photons. It then provides an overview of the instrumentation, focusing on detector components used to capture the emitted photons and the difference between pixelated and monolithic detectors. The chapter also explains the nature of collected PET data, the key performance metrics and their dependencies, and the principles of image reconstruction, with a focus on statistical iterative reconstruction and the necessary corrections. **Chapter 3** reviews recent advancements in PET technology such as time-of-flight (TOF) and depth-of-interaction (DOI) capabilities, as well as system design developments focusing on long-AFOV PET systems, sparse configurations and flat-panel geometries, relevant to this study. It also describes the Monte Carlo simulation framework that is central to this work, as well as the methods used to evaluate the performance of PET systems based on NEMA (National Electrical Manufacturers Association) standards with modifications where deemed necessary. The chapter concludes with a brief overview of deep learning applications in PET, particularly those employed for denoising and artifact reduction for limited-angle tomography.

The remaining chapters present the results of the work that has been accomplished. Various PET systems designs are proposed and performance-evaluated, with a focus on moderate extension of the AFOV for cost-effectiveness and the use of superior-resolution and DOI-capable monolithic detectors. Some performance metrics of the evaluated systems were benchmarked against current leading clinical PET systems, such as the Siemens Biograph Vision 600 and Quadra, whenever possible. The advantages, as well as the challenges and limitations were discussed while testing a possible deep learning-based solution. **Chapter 4** presents the simulation of two modular ring-based medium-AFOV PET designs featuring monolithic LYSO detectors. The axial extent of these systems is moderate compared to the long-AFOV systems, making them more cost-efficient and affordable. The superior spatial resolution they achieve is a property that current conventional and long-AFOV systems cannot yet match. This work has been published [1], [2]. **Chapter 5** builds on the same detector technology and thoroughly investigates a novel, non-cylindrical geometry, offering further cost reduction and higher throughput. Two vertical-flat-panel systems also featuring monolithic LYSO scintillators, based on the Walk-Through PET (WT-PET) concept

[3] were simulated and evaluated with emphasis on the sparse medium flat-panel (SpM-FP) design that can operate in a static mode or with limited panel motion depending on the study of interest. Its performance and specifically the presence of gaps was evaluated against the long flat panels (L-FP), a longer and fully populated design with the dimensions of the originally proposed WT-PET. This study was also published [4]. **Chapter 6** presents an in-depth investigation of the spatial resolution limits of the SpM-FP and the impact of achieving improved spatial resolution on lesion contrast and signal-to-noise ratio. These resolution limits are compared to a Monte Carlo model of the Siemens Biograph Vision 600 and measurements from other conventional scanners. Then, in **Chapter 7**, the limitations of the SpM-FP design, mainly the noise and elongation artifacts due to the side gaps that prevent a complete angular coverage in the transverse direction are addressed using image-based deep learning. A 2D U-Net, convolutional neural network is trained on PET patient-data from the *Ultra-Low Dose Challenge* [5]. The PET/CT images acquired on a Siemens Biograph Vision Quadra are used as ground truth data for simulation in the SpM-FP geometry. Three-minute acquisitions were reconstructed and used as input data to the network with the actual Quadra images used as targets. The goal is to reduce noise and elongation artifacts in the SpM-FP images. Finally, **Chapter 8** concludes this dissertation and discusses some future perspectives.

Chapter 2

Positron emission tomography

Since the discovery of X-rays in 1895, medical imaging has revolutionized healthcare and become indispensable for diagnosis, patient monitoring, and surgical guidance by allowing the visualization of internal structures of the human body. Over time, many imaging techniques have been developed, which can generally be divided into two categories:
Anatomical modalities focus on visualizing the structural anatomy of organs, tissues, and systems. These include traditional radiography and its three-dimensional version, computed tomography (CT). CT works by transmitting X-rays through the body, detecting variations in attenuation to produce contrast between tissues. Since X-rays are a form of ionizing radiation, dose reduction strategies are vital to minimize potential harm. CT is especially effective for identifying bone disorders, lung diseases, and strokes after trauma. Another key imaging method is magnetic resonance imaging (MRI), which uses strong magnetic fields and radiofrequency waves to excite hydrogen nuclei in water molecules within the body. Unlike CT, MRI does not involve ionizing radiation and offers superior soft tissue contrast. However, it is more expensive and requires longer scan time, making it less suitable for emergency situations. Ultrasound (sonography) uses high-frequency sound waves to create real-time images. It is commonly used in obstetrics and gynecology, echocardiography, and abdominal imaging (e.g., for gallstones or kidney stones), as well as for guiding minimally invasive procedures like biopsies or catheter insertions. Ultrasound is inexpensive, fast, portable, and radiation-free, making it highly adaptable in clinical practice.

Functional or molecular modalities complement anatomical imaging by providing insights into physiological processes such as blood flow, metabolism, and tumor activity. While techniques like functional MRI (fMRI) and CT perfusion can offer information on blood oxygenation and tissue perfusion, respectively, they were introduced later and have more limited clinical uses. In contrast, nuclear medicine techniques, specifically positron emission tomography (PET) and single-photon emission computed tomography (SPECT), were developed earlier to address the need for functional and molecular imaging, and they offer insights into metabolism, perfusion, and tumor activity. SPECT uses gamma-emitting radioisotopes like technetium-99m and iodine-123 for perfusion imaging in cardiology and neurology, as well as for detecting bone metastases and neuroendocrine tumors. Despite its relatively moderate cost, SPECT is limited by low spatial resolution, reduced sensitivity, and a lack of tumor-specific tracers, which restricts its utility in oncology. PET overcomes many of these limitations and has therefore gained increasing prominence in nuclear medicine. It enables in vivo visualization and measurement of physiological and metabolic processes. While mainly used in oncology for cancer diagnosis, staging and therapy monitoring, PET also plays an important role in cardiovascular disorders as well as neurological disorders such as dementia and Parkinson's disease. The technique relies on biologically relevant compounds labeled with positron-emitting radionuclides, such as fluorine-18 (^{18}F), carbon-11 (^{11}C), Gallium-68 (^{68}Ga), and oxygen-15 (^{15}O), to serve as tracers for specific physiological processes. In oncological applications, the most widely used tracer is ^{18}F-fluorodeoxyglucose (^{18}F-FDG), a glucose analog that accumulates in tissues with high glucose metabolism, such as malignant tumors [6]. To provide accurate anatomical information for diagnostic and localization purposes, PET is typically combined with an anatomical modality, most commonly CT and less frequently MRI, to form a multimodality PET/CT or PET/MR. Figure 2.1, adapted from [7] shows ^{18}F-FDG PET/CT and PET/MR images illustrating the distribution of the radiopharmaceutical within the body.

In this chapter, we explore the foundational physical principles underlying PET imaging, the detector technology that enables its operation, and the nature of the data it produces. We also examine the reconstruction process that converts raw detection events into clinically meaningful images, highlighting both the performance capabilities and inherent limitations of PET systems.

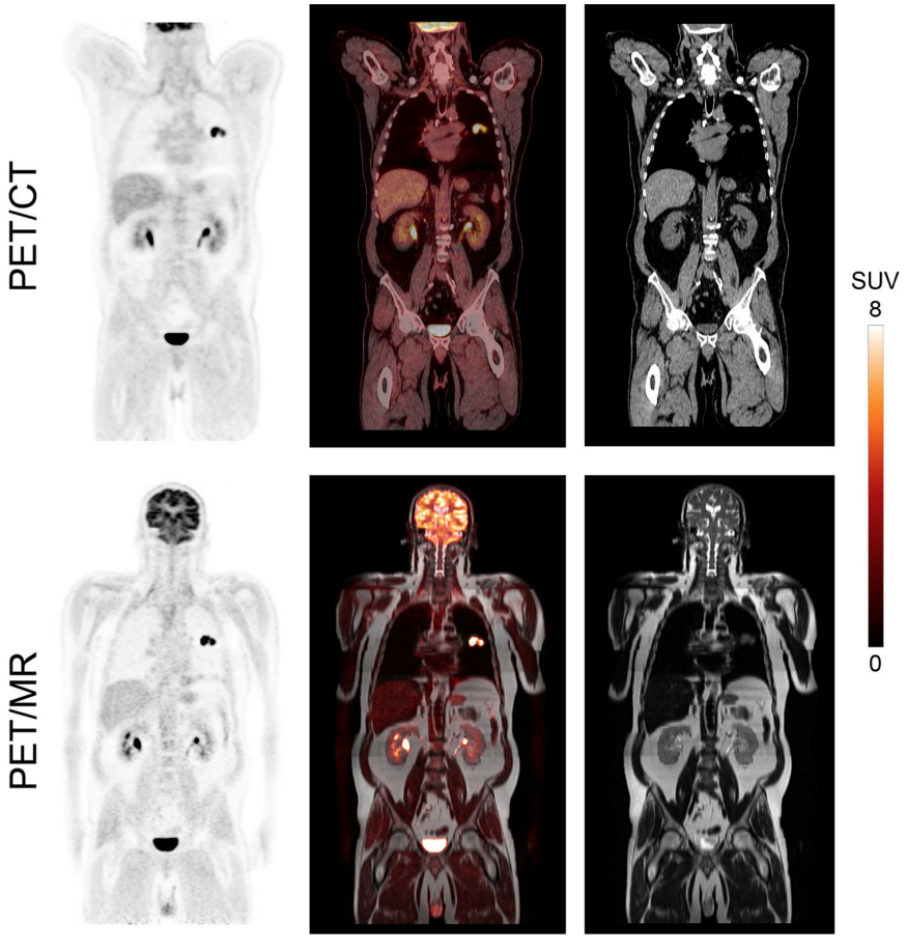

Figure 2.1: Left panel shows only PET images - middle panel: top row is a fused PET/CT image and bottom row is a fused PET/MR image - right panel: top row is only CT image and bottom row is only MR image. Adapted from [7].

2.1 PET physics

2.1.1 Radioactive decay

A nucleus with an excess number of protons or neutrons is unstable and undergoes radioactive decay, a spontaneous process in which energy is emitted in the form of ionizing radiation, allowing the nucleus to

transition to a more stable state. There are various modes of radioactive decay, each characterized by the emission of different particles or photons. The mode most relevant to PET imaging is beta-plus (β^+) decay, in which nuclei with an excess of protons decay through the emission of a positron. In this process, a proton is converted into a neutron, releasing a positron (e^+) and an undetected neutrino. The most commonly used radionuclide in PET imaging is fluorine-18 (^{18}F), produced in a cyclotron via proton irradiation of enriched oxygen-18 (^{18}O) water. ^{18}F decays to stable ^{18}O via positron emission, as shown below:

$$^{18}\mathrm{F} \rightarrow {}^{18}\mathrm{O} + e^+ + \nu \tag{2.1}$$

Radioactive decay is characterized by the half-life of the radionuclide, the time required for half of the nuclei in a sample to decay, following an exponential pattern. For ^{18}F, the half-life is approximately 110 minutes, which represents an optimal balance: long enough to allow for radiotracer injection and uptake for patient imaging, yet short enough to minimize radiation exposure.

2.1.2 Positron range

The emitted positron travels a finite distance before annihilating with an electron from the surrounding tissue. The median distance it travels, called the positron range, depends on the positron's kinetic energy, which varies with the radionuclide. For example, ^{18}F emits positrons with relatively low kinetic energy, about 0.63 MeV, resulting in a short positron range in tissue. Since PET measures the annihilation location, it is best for this point to be as close as possible to the emission site. This makes the short positron range of ^{18}F beneficial by minimizing its impact on the spatial resolution of PET images. A Monte Carlo simulation study reported the median range of ^{18}F positrons to be 0.44 mm in soft tissue and 1.41 mm in lung tissue. In comparison, for ^{68}Ga the corresponding ranges are significantly larger: 2.4 mm in soft tissue and 8 mm in lung tissue, which can lead to greater degradation in spatial resolution compared to ^{18}F [8]. Table 2.1 lists selected radionuclides that decay by positron emission along with their corresponding half-lives and maximum kinetic energy of the emitted positrons, as reported in [9].

Table 2.1: Positron-emitting radionuclides relevant to PET imaging, with their half-lives and the maximum kinetic energy of emitted positrons. Data adapted from [9].

Radionuclide	Half-life	$E_{\max}$ (MeV)
^{18}F	110 min	0.63
^{68}Ga	68.3 min	1.90
^{11}C	20.4 min	0.96
^{13}N	10 min	1.19
^{15}O	123 s	1.72
^{124}I	4.18 d	1.50

2.1.3 Positron-electron annihilation & photon non-collinearity

Following β^+ decay, the emitted positron rapidly loses its kinetic energy through inelastic interactions with bound electrons of the surrounding tissue. Once it has dissipated all its energy, the positron combines with an electron, and the two particles annihilate. This annihilation event produces two high-energy photons, each with an energy of 511 keV, emitted in approximately opposite directions to ensure the conservation of energy and momentum in this process. A key advantage of the simultaneous back-to-back emission of the two photons is that the location of the annihilation event, and thus, approximately, the site of positron emission, is known to be along the line connecting the two detected photons, referred to as the line of response (LOR). However, because the positron and electron are not entirely at rest when they annihilate, a small net momentum exists in the system. As a result, the two photons are not emitted at exactly 180 degrees, but with a slight angular deviation. This phenomenon, known as **non-collinearity**, introduces an error in determining the LOR, which in turn leads to an uncertainty in the annihilation position and ultimately contributes to spatial resolution degradation in PET imaging. The angular distribution of the annihilation photons is approximated by a Gaussian with a full width at half maximum (FWHM) of 0.5 degrees. This angular deviation contributes to the blurring in the reconstructed image and can be estimated by:

$$R_{180^\circ} = 0.0022 \times D \tag{2.2}$$

where D is the diameter of the PET scanner. For a typical scanner with a diameter of 80 cm, this results in a blurring of approximately 2 mm, which

is greater than the contribution of positron range on spatial resolution. In pre-clinical scanners, which have much smaller diameters (10-20 cm), the effect of non-collinearity is minimal and does not significantly limit spatial resolution [9].

2.1.4 Interaction of radiation with matter

To understand how the emitted 511-keV photons interact with the surrounding tissue, get attenuated in the patient, and are ultimately stopped and detected by scintillators, it is essential to explain the photoelectric and Compton effects. Other interactions, such as Rayleigh scattering and pair production, also exist but are not dominant at this energy level. Rayleigh scattering is more prominent at lower photon energies (less than 50 keV), while pair production becomes relevant only at much higher energies (higher than 1.022 MeV) than those encountered in PET imaging.

Photoelectric effect

The photoelectric effect involves the complete absorption of a photon by the surrounding medium through its interaction with an atom. The photon transfers all its energy to an inner-shell electron, which is then ejected from the atom. This ionization leaves the atom in an excited state. To return to its ground state, an electron from a higher shell drops into the lower vacant shell, emitting either a characteristic X-ray or an Auger electron in the process. The probability of photoelectric absorption depends on both the photon's energy and the atomic number Z of the absorbing material. This probability increases when the photon energy is near the binding energy of electrons in a particular shell and is significantly higher in materials with a high atomic number. Figure 2.2 taken from [9] shows the dominating interactions as a function of photon energy for different values of absorber atomic number Z. The photoelectric effect is predominant at energies below 100 keV and less likely at 511 keV.

Compton scattering

The Compton effect refers to the inelastic scattering of a photon by a free or loosely bound electron in the medium. During this interaction, the photon transfers some of its energy to the electron and is deflected from its original path. The resulting scattered photon may subsequently undergo

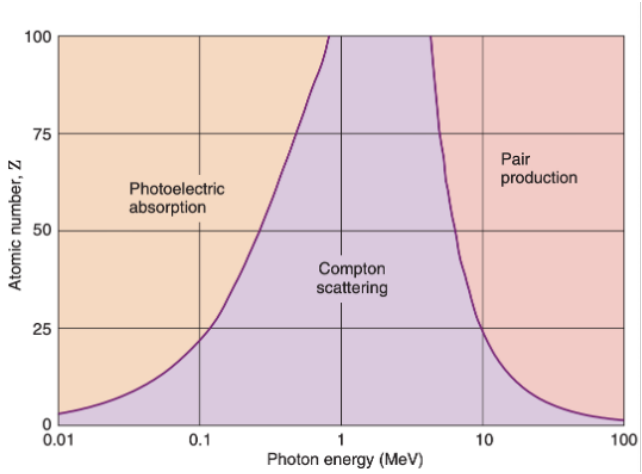

Figure 2.2: Dominant radiation-matter interactions as a function of the photon energy for different atomic number of the absorbent material [9].

additional Compton scattering or be absorbed via the photoelectric effect. As can be seen in Figure 2.2, this effect dominates photon interactions in human tissues in the energy range of 100 keV to just below 10 MeV. This makes it particularly relevant in PET imaging, where the photon energy is 511 keV. Based on conservation of energy and momentum, the energy of the scattered photon E_{sc} can be expressed as a function of the initial photon energy E, the electron rest mass energy $m_{\mathrm{e}}c^2$, and the scattering angle θ as shown in Figure 2.3:

$$E_{\mathrm{sc}} = \frac{m_e c^2}{\frac{m_e c^2}{E} + 1 - \cos\theta} \tag{2.3}$$

Since the photon energy in PET is 511 keV, the same as the rest mass energy of an electron, equation 2.3 simplifies to:

$$E_{\mathrm{sc}}\,(\mathrm{keV}) = \frac{511}{2 - \cos\theta} \tag{2.4}$$

As shown in Figure 2.4, the angular distribution of the scattered photons at 511 keV favors small-angle forward scattering. According to equation 2.4, this results in scattered photons whose energies deviate only slightly from the original 511 keV.
Photons that are either absorbed via the photoelectric effect or scattered

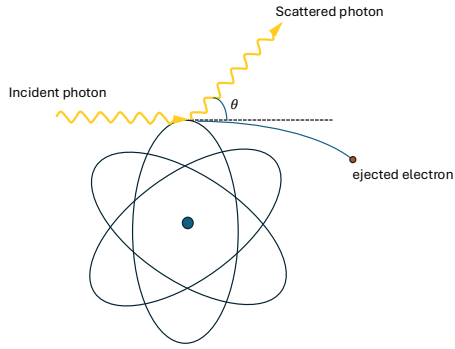

Figure 2.3: Schematic representation of the Compton scattering showing the angle θ of the scattered photon after interacting with a loosely bound outer-shell electron of an atom.

through Compton interactions are considered attenuated, following an exponential attenuation law described by:

$$I(x) = I(0)\exp(-\mu x) \tag{2.5}$$

where I_0 is the initial intensity of the photon beam, I(x) is the intensity after the beam has traveled a distance x through a material, and μ is the linear attenuation coefficient, which is a measure of the attenuation per unit distance. At an energy of 511 keV, the attenuation coefficient μ is predominantly composed of contributions from both Compton scattering and the photoelectric effect, such that:

$$\mu \approx \mu_{\text{Compton}} + \mu_{\text{photoelectric}} \tag{2.6}$$

The primary media affecting photon attenuation in PET imaging are the human body and the detector material. Within biological tissues such as soft tissue and bone, attenuation is mainly due to Compton scattering. The linear attenuation coefficient μ depends on both the energy of the incident photons and the physical properties of the medium, particularly its density and effective atomic number (Z). Table 2.2 presents the attenuation coefficients at 511 keV for representative biological tissues and commonly used PET scintillators, including bismuth germanate (BGO), lutetium oxyorthosilicate (LSO), and lutetium-yttrium oxyorthosilicate (LYSO). Based on the attenuation coefficients for soft tissue and bone, and assuming average photon path lengths of approximately 8 cm in the

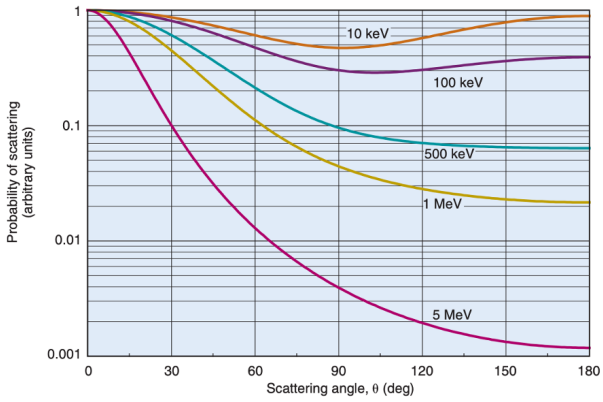

Figure 2.4: Relative probability of Compton scattering (normalized per unit of solid angle) versus scattering angle θ for different incident photon energies. Adapted from [9].

Table 2.2: Linear attenuation coefficients at 511 keV for soft tissue, bone and common PET scintillators. Values adapted from [10].

Material	μ (cm^{-1})
Soft tissue	0.096
Bone	0.17
BGO	0.96
LSO	0.87
LYSO	0.82

brain and 20 cm in the torso, roughly 60% of photons are expected to be attenuated in the brain and 85% in the body.

2.2 PET instrumentation

To detect the coincident 511 keV photons emitted from positron annihilation within the patient, PET systems typically employ a ring arrangement of detectors that surrounds the patient, ensuring complete transverse coverage. Early PET scanners featured a single ring of detectors, with the axial field-of-view (AFOV) determined by the number and arrangement of available detector modules. Modern systems use multiple rings or extended axial coverage to provide a bigger solid angle coverage. Because 511 keV photons are highly penetrating, detector materials with high

stopping power are crucial for effectively absorbing these photons. Once absorbed, the photon interaction must be converted into an electrical signal that accurately records the time, position, and energy of the event, enabling precise coincidence detection and image reconstruction. Accordingly, PET detectors are composed of three primary components: the scintillation crystal, the photodetector, and the readout electronics, see Figure 2.5.

2.2.1 PET detector components

Scintillation detectors: inorganic crystals with activators

Scintillators can be organic or inorganic compounds and may exist in solid or liquid forms. For PET imaging, the preferred scintillators are dense, inorganic, and in solid form, as they offer sufficient stopping power to efficiently absorb the 511 keV annihilation photons. Upon interaction, primarily through the photoelectric effect, Compton scattering, or a combination of both, the incident photon deposits its energy in the crystal, promoting electrons from the valence band to the conduction band, thereby creating electron-hole pairs. The number of such pairs is proportional to the energy deposited. In pure crystals, when electrons return from the conduction band to the valence band, the resulting photon emission typically lies outside the visible spectrum and occurs with low efficiency. To address this, activator ions referred to as impurities are introduced into the crystal. These dopants create intermediate energy levels within the band gap, facilitating the de-excitation of electrons to the valence band by emitting lower-energy optical photons through the process of luminescence. The key properties of an ideal PET scintillator include:

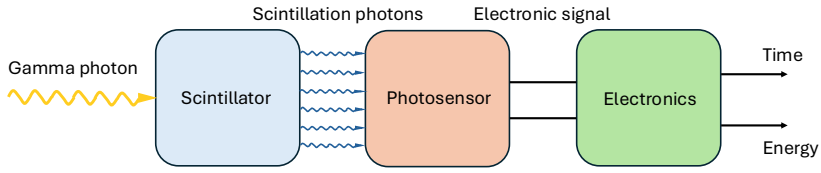

Figure 2.5: Schematic representation of a PET detector showing its three main components.

- **High stopping power**: This depends on the scintillator's physical density and effective atomic number Z_{eff}. A high Z_{eff} increases the probability of interaction via the photoelectric effect over the Compton scattering which is advantageous for accurate photon detection. For instance, **BGO** has a density of **7.1 g/cm**^{3} and $\boldsymbol{Z}_{\text{eff}} \approx 75$, providing a high probability of photoelectric interactions at 511 keV. A sufficiently thick scintillator is required to ensure efficient photon absorption, but excessive thickness may degrade spatial resolution. High stopping power also reduces intercrystal scattering, thereby improving LOR determination [11] and helps mitigate parallax errors by minimizing the depth of penetration of obliquely incident photons [12].

- **High light yield** or scintillation brightness: This refers to the number of optical photons produced per unit of absorbed energy, typically per MeV. A higher light yield improves the energy resolution by enabling more accurate estimation of the deposited energy. For example, LSO and LYSO crystals typically produce approximately 26000-32000 photons/MeV whereas for BGO it is in the order of 8500 photons/MeV [13], [14].

- **Fast rise and decay times**: Short scintillation rise and decay times enable the detector to respond rapidly to incoming photons, offering high temporal resolution and reducing signal pile-up. While BGO has a decay time of 300 ns, LSO and LYSO provide much shorter decay times of about 40 ns and have a fast rise time of approximately 70 ps, making them well-suited for time-of-flight (TOF) applications [13], [14].

- **Refractive index compatibility**: To ensure efficient light transmission to the photodetector, the scintillator's refractive index should closely match that of the photodetector.

Table 2.3 compares BGO, LSO, and LYSO scintillators, given their relevance to the work presented in this manuscript and supporting specific design and detector decisions.

Table 2.3: Characteristics of common PET scintillators. Values taken from [15], [16].

Material	Effective Z	Density (g/cm^3)	Light yield (photons/MeV)	Decay time (ns)	μ_{511} keV/cm
BGO	73	7.13	8500	300	0.96
LSO	65	7.35	30000	40	0.87
LYSO	64	7.19	30000	40	0.82

Photodetectors

The scintillation light emitted by the crystals must be efficiently collected, amplified and converted into an electrical signal. This process is carried out by photodetectors, with the most common types being the photomultiplier tubes (PMTs) and silicon photomultipliers (SiPMs). Historically, PMTs were the standard in PET imaging due to their high gain and fast response. However, their usage is gradually being phased out due to several limitations: they are bulky, fragile, require high operating voltages and exhibit relatively low quantum efficiency (i.e., the probability that an absorbed photon generates a signal). Additionally, their size and sensitivity to magnetic fields limit integration into multimodal PET/MRI systems. In contrast, SiPMs, solid-state, semiconductor-based detectors are increasingly becoming the preferred choice for modern PET systems as they overcome many of the challenges posed by PMTs. SiPMs are significantly more compact and robust, making them ideal for high-density detector configurations. They operate at much lower voltages, typically around 20-70 V, and are immune to magnetic fields. Furthermore, their higher quantum efficiency, especially in the blue-green spectrum where many scintillators emit, enhances signal detection. Most importantly, they exhibit excellent timing performance, including a very good single-photon time resolution (SPTR), which has enabled commercial PET scanners to achieve coincidence time resolutions (CTR) as low as 200 ps FWHM [17]. A SiPM consists of an array of microcells connected in parallel, with each consisting of a single-photon avalanche diode (SPAD) in series with a quenching resistor. A SPAD is a type of p-n junction diode operated at a reverse bias above its breakdown voltage. When an optical photon hits the active area of the diode, it generates an electron-hole pair. In the presence of a high electric field, the electron and hole will accelerate and gain enough energy to knock out other electrons and holes, which will trigger an avalanche of more

charge carriers, leading to a current growing to a macroscopic level from just a single absorbed photon. This current continues to flow until the avalanche is quenched by reducing the bias voltage down to or below the breakdown voltage. Then the SPAD is ready to detect another photon [18]. The collective signal from the array of SPADs is proportional to the number of incident photons, allowing for both accurate energy estimation and precise timing. Despite their advantages, SiPMs require careful optimization of parameters such as temperature sensitivity, dark count rates and optical crosstalk, all of which can affect performance in PET systems.
The electronics will read out the output signal from the photodetector and further process it to extract key information, such as the timestamp and the energy measured by each SiPM. Therefore, the selection of suitable electronic components is critical to achieving good time resolution in PET imaging.

2.2.2 Pixelated and monolithic detectors

PET scintillation detectors are primarily categorized into two types: pixelated and monolithic. An overview of each type, including its respective advantages and limitations is provided below.

Pixelated detectors

The standard in current clinical PET systems is the use of pixelated detectors. In this configuration, scintillator blocks are subdivided into arrays of smaller crystals called pixels separated by a white reflective material that prevents inter-pixel optical photon transfer. This arrangement confines the scintillation light to the pixel where the 511 keV photon interaction occurred, effectively minimizing light spread and enabling straightforward estimation of the 2D interaction position and timing. Because the light is channeled through a single pixel, the interaction can be localized using the signal from just one SiPM, which allows for accurate time stamping due to the rapid rise of the waveform above the noise level. As a result, pixelated detectors can achieve excellent timing performance. In pixelated detectors, two factors limit the spatial resolution: the finite size of the pixels and the lack of depth-of-interaction (DOI) information. The intrinsic resolution of a pixelated detector can be approximated by a Gaussian function whose FWHM is determined by the pixel size. At the midpoint between opposing detectors, the coin-

cidence response function has a triangular shape with a FWHM equal to half the detector width. This FWHM increases as the source is moved toward one of the detectors. In clinical PET systems, typical pixel sizes range from 3 to 4 mm, imposing a limit on the achievable system spatial resolution. Although reducing pixel size can improve spatial resolution, it often compromises energy and TOF performance due to decreased light output [19]. Smaller pixels also reduce detector sensitivity, as the increased use of reflective coatings between pixels introduces more dead space. Additionally, thick crystals, usually 15 to 30 mm, are required to effectively stop the 511 keV photons. This introduces radial parallax or DOI effects as illustrated in Figure 2.6 where increased radial offsets lead to asymmetry in the point spread function. When the source is at a radial offset, the detectors are at an angle which causes the coincidence response function to become broader and asymmetric.

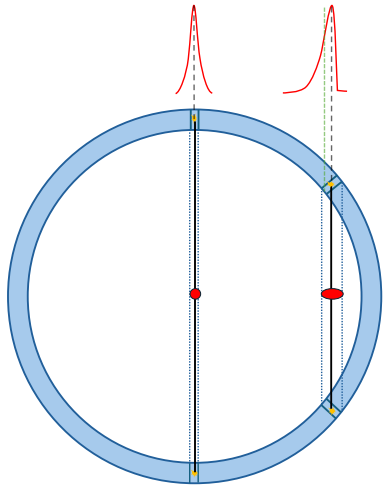

Figure 2.6: Schematic representation of radial parallax error for a source at a radial offset showing the asymmetry of the point spread function due to the lack of DOI.

This asymmetry results from discrepancies between the true interaction site and the assumed LOR, which is inferred from the crystal surface entry point. Moreover, the absence of DOI information imposes further limits on the spatial resolution in long AFOV PET systems, particularly due to axial parallax affecting centrally located events with highly oblique

LORs. Typically, pixelated detectors do no provide DOI information unless modifications are made to the detector design. Dual-ended readout is a well-established method [20], but it increases costs and manufacturing complexity because photodetectors are coupled to both ends of the scintillator array, and DOI is estimated from the ratio of light collected at the two ends. Alternatively, DOI can be encoded in a single-ended readout design by utilizing controlled light sharing where the distribution of light across multiple pixels depends on DOI and allows depth estimation [21].

Monolithic detectors

A monolithic detector consists of a large continuous block of scintillation material without any segmentation or gaps, typically a few centimeters wide. When a gamma photon interacts within the crystal, the resulting scintillation light spreads throughout the block and is collected by an array of photodetectors (e.g., SiPMs). By analyzing the spatial distribution of the detected light, both the 2D position and the depth-of-interaction (DOI) of the event can be estimated. A concentrated light spread over a small number of photodetector pixels indicates that the interaction occurred near the photodetectors, deep in the crystal. Conversely, a broader light spread suggests that the interaction took place further away from the detector array, as illustrated in Figure 2.7.

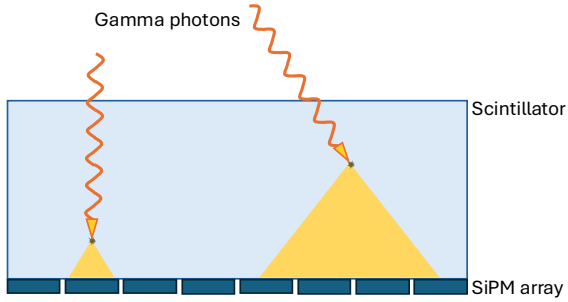

Figure 2.7: Schematic representation of the 2D light spread inside a monolithic scintillator.

In monolithic detectors, the intrinsic spatial resolution depends on the number of available scintillation photons. The response function is typically approximated by a Gaussian with a FWHM that depends on how close the source is to the monolithic detector. Half-way between

the two detectors the coincidence response function is approximated as FWHM $\approx \frac{R_{\text{int}}}{\sqrt{2}}$ and closer to the detector face FWHM $\approx R_{\text{int}}$, where R_{int} is the individual intrinsic detector resolution. Despite their advantages, monolithic detectors present two main challenges. First, accurate positioning requires an extensive calibration process, which becomes increasingly complex near the crystal's edges and corners, where light behavior becomes less predictable. Second, the timing resolution is degraded due to the spreading of scintillation light over multiple photodetector channels, resulting in fewer detected photons per SiPM and an increased contribution from dark counts.

2.3 PET data collection and system performance

2.3.1 Types of events

PET scanners detect pairs of 511 keV photons in coincidence, eliminating the need for absorptive collimation to determine the origin and trajectory of the emitted photons. This is referred to as electronic collimation, which avoids the substantial sensitivity loss associated with mechanical collimators, making PET the most sensitive imaging modality in nuclear medicine. However, the two photons emitted following the positron-electron annihilation within the subject do not always reach the PET detectors without interaction. Along their paths, one or both photons may undergo Compton scattering, which alters their direction and reduces their energy. Less frequently, photons are absorbed by the photoelectric effect and are not detected. Additionally, some photons may escape detection entirely if their paths do not intersect the detectors, due to the limited coverage of the detectors. As a result, detected events are categorized into true, scattered, and random coincidences with a typical rate of 50-70%, 20-40%, and 5-15%, respectively. The exact proportions depend on administered activity concentration, patient size, scanner design and acquisition parameters. Scattered and random events degrade image quality, requiring correction techniques to ensure that the reconstructed image accurately reflects the tracer distribution within the patient.

True coincidences

True coincidences occur when both gamma photons originate from the same annihilation events, traverse the patient's body without undergoing any interaction, and are detected within the same coincidence time window (CTW). These events provide accurate spatial information about the radiotracer distribution within the body and are essential for high-quality PET image reconstruction. However, this represents an ideal scenario. In practice, PET data also include scattered and random coincidences.

Scattered coincidences

Scattered coincidences occur when one or both photons undergo Compton scattering inside the patient, resulting in a deflection from their original paths. In the human body where tissue density is similar to that of water, the mean free path of a 511 keV photon is approximately 7 cm [22]. However, the cross-section of the human body, even for low BMI, typically exceeds 7 cm and is even larger for high BMI individuals, making it likely that many of the photons will undergo Compton scattering before reaching the PET detectors. As a result, the LORs associated with these events no longer accurately represent the true annihilation locations. This mispositioning introduces noise and reduces image contrast. While scattered photons lose energy upon interaction, which allows for their identification using energy discrimination, practical limitations in detector energy resolution do not permit perfect rejection. Therefore, dedicated correction techniques are required during image reconstruction to mitigate the impact of scatter.

Random coincidences

Random coincidences occur when two unrelated photons, originating from separate annihilation events, are detected within the same CTW. These false coincidences do not represent valid LORs and contribute to an increased background noise, reducing image contrast and quantitative accuracy. The rate of random coincidences increases with both the CTW width and the injected activity, as shown in equation:

$$R = 2\tau N_1 N_2 \tag{2.7}$$

where 2τ is the width of the CTW, N_1 and N_2 are the individual detection rates, which directly depend on the activity in the scanner's

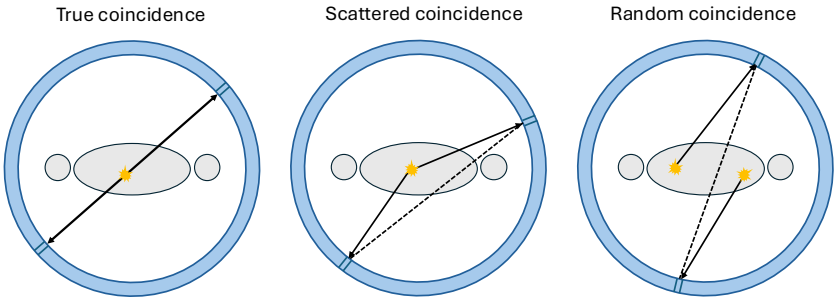

Figure 2.8: Schematic representation of true, scattered and random coincidences.

FOV. Random events increase with the square of the injected activity. Therefore, optimizing the width of the CTW and maintaining a proper activity level are essential for balancing sensitivity and avoiding random events. Random correction algorithms are used during reconstruction to reject these events. Figure 2.8 is a schematic representation of true, scattered and random coincidence events.

2.3.2 PET system performance

Having covered the fundamental physics of PET imaging and the core components of a PET scanner, it is essential to examine the system performance metrics that guide the design and optimization of PET systems. A well-informed approach requires identifying the key performance priorities and understanding the trade-offs involved. Design and instrumentation choices inevitably impact various metrics, enhancing one aspect often comes at the expense of another. Sensitivity is among the most critical metrics. Even with perfect spatial, temporal, and energy measurements, poor sensitivity, i.e., an insufficient number of detected events will result in poor image quality. High sensitivity ensures enough counts are acquired to produce accurate and clinically useful images. Another major consideration is spatial resolution, which determines the system's ability to distinguish small structures, detect fine details, and accurately localize lesions. This is vital across virtually all PET imaging applications. Time resolution plays a crucial role, especially in TOF-PET as it helps limit the propagation of noise in the image reconstruction process. Better timing translates to improved signal-to-noise ratio (SNR) and more precise event localization along the LOR. Energy resolution

is equally important, as it helps eliminate scattered photon events and reduces background counts, further enhancing image contrast and accuracy.
Ultimately, a key question remains: how close can current technology bring us to the physical limits of spatial, temporal, and energy precision? The following sections explore these performance metrics in greater detail, examining the factors that influence them, the current technological capabilities, and the remaining limitations.

Sensitivity and SNR

The sensitivity of a PET scanner is defined as the ratio of detected to emitted gamma photons for a known activity in the absence of attenuation, expressed in counts per second per kilobecquerel (cps/kBq). Sensitivity plays a central role in determining the image SNR and is mainly influenced in by the system's geometric efficiency, which depends on the overall solid angle coverage of the detectors and their intrinsic detection efficiency. To put this in context, the number of detected events n in a PET scan, which directly influences the SNR, with SNR $\propto \sqrt{n}$, can be approximated by:

$$n \approx kAG\varepsilon^2 T \tag{2.8}$$

where A is the activity in the scanner's FOV, G is the average geometric coverage of the scanner, ε is the detector efficiency (squared because the photons should be detected in coincidence), T is the acquisition time and k accounts for losses due to attenuation and scatter which vary with patients. While increasing the injected activity A or extending the acquisition time T can improve sensitivity, both options come with drawbacks. Higher activity raises radiation exposure, which is especially concerning for pediatric or vulnerable populations. Longer scan durations increase patient discomfort and limit scanner throughput. The state-of-the-art whole-body PET scans already require up to 15 minutes. This leaves geometric coverage G and detector efficiency ε as the most practical levers for improving sensitivity. Detector efficiency is largely dictated by the scintillator's stopping power and thickness. Increasing scintillator thickness improves photon absorption but introduces trade-offs: it can degrade timing resolution, increase system cost, and offer only marginal benefits due to the exponential nature of photon attenuation. To overcome these limitations, many research efforts have focused on enhancing sensitivity by increasing solid angle coverage, particularly by extending the scanner's AFOV. However, the sensitivity gain resulting

from expanding the AFOV depends on the size and axial extent of the imaged object. For single-organ imaging, the gain follows roughly that of a point source, increasing linearly with scanner length until it reaches a plateau. In contrast, for extended objects or whole-body, sensitivity increases approximately quadratically with AFOV. Depending on the scanner design and object dimensions, sensitivity gains can range from a factor of 10 to 40 [23], [24]. Ultimately, the decision to extend the AFOV should be guided by the specific imaging application and the potential benefits in terms of sensitivity and image quality for the targeted use case.

Timing resolution, TOF and SNR

With the same number of detected events, the SNR of a PET image can be improved if the system can extract more information from each event, particularly precise timing information. In PET imaging, three key measurements are recorded for each event: the interaction positions of the gamma photons in the detectors, their arrival times, and the deposited energies. Each of these contributes to localizing the annihilation event and reconstructing the radiotracer distribution in the body, but they are all subject to uncertainties due to detector limitations and statistical fluctuations. In an ideal system, the difference in arrival times of the two photons is measured accurately ($\Delta t = t_2 - t_1$), and the position of the annihilation event along the LOR can be precisely localized relative to the midpoint between the two detectors according to $\Delta x = \frac{c\Delta t}{2}$ where c is the speed of light (see Figure 2.9). In practice, however, the arrival time of each photon cannot be measured perfectly due to the statistical nature of scintillation light emission and transport, as well as limitations of detectors and electronics. The resulting uncertainty in the time difference between the two detected photons is referred to as the coincidence time resolution (CTR) or the system's TOF resolution. This uncertainty is typically modeled as a Gaussian distribution as shown in Figure 2.9, with its FWHM equal to the TOF resolution. Incorporating TOF information replaces the uniform probability assumption used in non-TOF PET, where all voxels along the LOR are equally probable to be the source of emission, with a Gaussian kernel centered around the estimated annihilation point. The time resolution of a PET system mainly depends on the scintillator's decay time and light yield, the photodetector photon detection efficiency (PDE), single photon time resolution (SPTR), and the related electronics [25]. The current state-

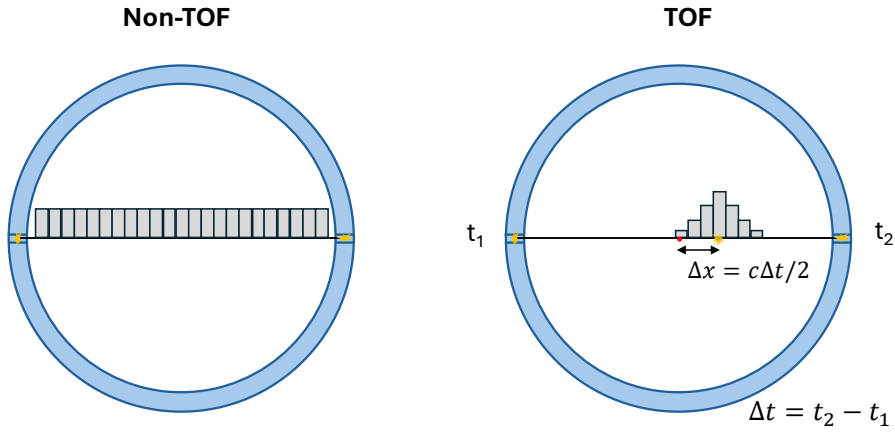

Figure 2.9: Illustration of the effect of time-of-flight on event localization with a certain probability.

of-the-art clinical PET systems typically achieve a TOF resolution of approximately 200 ps FWHM, corresponding to a spatial uncertainty of about 3 cm along the LOR. This localization, when incorporated in the image reconstruction process, reduces the noise and accelerates its convergence. By constraining the probable annihilation location, TOF information enhances SNR compared to non-TOF systems, thereby increasing the system's effective sensitivity. The benefit of TOF increases with timing resolution and becomes more pronounced for larger patients, where the spatial uncertainty Δx constitutes a smaller fraction of the patient's diameter D, which gives a strong localization advantage. The SNR gain from non-TOF to TOF is proportional to $\sqrt{\frac{D}{\Delta x}}$ [26], [27], [28].

Spatial resolution

Spatial resolution in PET imaging refers to the system's ability to accurately localize annihilation events and distinguish two closely spaced points as separate entities. It is a critical performance metric that depends on the intrinsic resolution of the detectors, as well as physical effects such as positron range and photon non-collinearity. The combined effect of these factors can be modeled as the convolution of their respective resolution response functions. The following quadratic summation commonly approximates this:

$$R_{\text{sys}} \approx \sqrt{R_{\text{det}}^2 + R_{\text{range}}^2 + R_{180^\circ}^2} \tag{2.9}$$

Here, R_{det} represents the intrinsic detector resolution, R_{range} the contribution from the positron range, and R_{180° accounts for the deviation from perfect 180° photon emission (non-collinearity). The positron range depends primarily on the selected radiotracer and its positron energy, while non-collinearity is a geometric limitation that scales with the PET system's diameter. Since both the positron range and photon non-collinearity are fundamental physical limitations largely dictated by tracer choice and system geometry, optimizing the detector resolution becomes the primary avenue for improving overall spatial resolution. One additional factor that can degrade spatial resolution is the parallax error, which arises when photons enter the detector at oblique angles. This effect varies across the FOV, with greater degradation toward the edges. It is also important to note that the limited number of detected events in a PET scan results in a low SNR, which in turn contributes to reduced image resolution. Therefore, efforts to enhance detector performance, increase sensitivity, and improve event localization, all contribute to a superior reconstructed image quality. Another important consequence of limited spatial resolution is the **partial volume effect (PVE)**, which poses a significant challenge when quantifying activity in small lesions or anatomical structures [29]. Due to the blurring introduced by the system's point spread function (PSF), small objects appear smeared out in the reconstructed image and consequently exhibit a lower measured activity concentration than their true value as shown in Figure 2.10 adapted from [30]. The peak activity recovered from such a structure is directly influenced by its size relative to the image resolution; smaller objects suffer more pronounced losses. Therefore, improved spatial resolution not only enhances visual detail and the ability to resolve adjacent structures but also plays a vital role in accurate quantification. A study has shown that if the object's size is at least three times greater than the system's spatial resolution, then a small region of interest (ROI) placed within the object can provide a reliable estimate of its true activity concentration [10]. Consequently, minimizing the PVE through superior system resolution is essential for both qualitative interpretation and quantitative accuracy in PET imaging.

Energy resolution

Energy resolution refers to the ability of a PET system to accurately measure the energy of incoming photons and distinguish between radiation of different energies. Good energy resolution enables effective

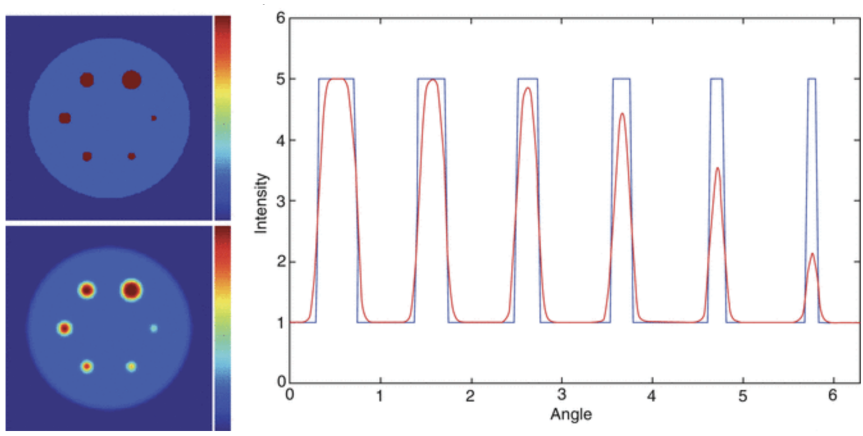

Figure 2.10: Illustration of the partial volume effect in a cylindrical phantom containing six spherical inserts (diameters 6, 9, 12, 15, 18 and 24 mm) with a sphere-to-background contrast ratio of 4:1. The phantom was blurred with a 3D Gaussian PSF with a 6-mm FWHM. The images on the left show a transaxial slice of the original image (top) and the blurred image (bottom) and the graph on the right shows a profile through the spheres. The blue line represents the true data and the red line represents the blurred data. Adapted from [30].

rejection of scattered coincidences, whose photon energies are reduced relative to the 511 keV photons that reach the detector without prior interaction. The energy resolution of a PET detector mainly depends on the scintillator's light output, as producing more optical photons during scintillation allows for a more precise estimate of the deposited energy. The interaction point within the crystal also influences this, since optical photons might escape the crystal before detection. Moreover, statistical fluctuations in the photodetector response add to the broadening of the energy spectrum. This energy distribution is usually represented as a Gaussian curve, with a photopeak at 511 keV and a FWHM indicating the system's energy resolution. Due to the finite energy resolution of real systems (typically 10%), many of the scattered photons have energies that fall within the broadened photopeak, making them indistinguishable from true coincidences. The narrower the photopeak, the better the system can discriminate against scattered events. Scattered events, similar to random events, contribute to the image background and reduce contrast because they result in mispositioned LORs that do not accurately

reflect the true activity distribution within the FOV. Therefore, improved energy resolution directly contributes to a reduction in background noise and enhanced image contrast.

2.4 PET image reconstruction

Following data acquisition (measured LORs), the next step is image reconstruction which aims to produce an accurate representation of the tracer activity distribution λ in the subject based on the measured data y. Mathematically, this process can be represented as

$$y = H\lambda + e \tag{2.10}$$

where H is the system model or response matrix, which accounts for the physics and geometry of the PET system, and e represents the additive noise present in the measured data y. y consists of projection data, commonly referred to as sinograms. While data acquisition is three-dimensional, Figure 2.11 shows a two-dimensional representation as a function of the radial distance and projection angle. To recover the tracer distribution λ, various reconstruction methods are employed in PET. These methods are broadly classified into two categories: analytic and iterative techniques.

2.4.1 Analytic reconstruction

The filtered-back-projection (FBP) algorithm is one of the most commonly used analytic reconstruction methods to approximate a solution to equation 2.10, as the inverse problem is ill-posed and does not have a unique exact solution. FBP works by back-projecting the measured data uniformly along each LOR, because the original activity distribution along the LOR is lost during the forward projection [31]. By repeating this process for all measured projection angles and applying a filter (typically a ramp filter) before backprojection to compensate for undersampling of mid- to high-spatial frequencies, FBP generates a superposition of back-projections that approximates the true activity distribution. Modifying the ramp filter by adjusting the cutoff frequency allows control over noise (represented by high-frequency components) while preserving spatial resolution. Although FBP is straightforward to implement, computationally efficient, and a linear method, it does not account for the noise statistics of the data or model non-ideal effects of the

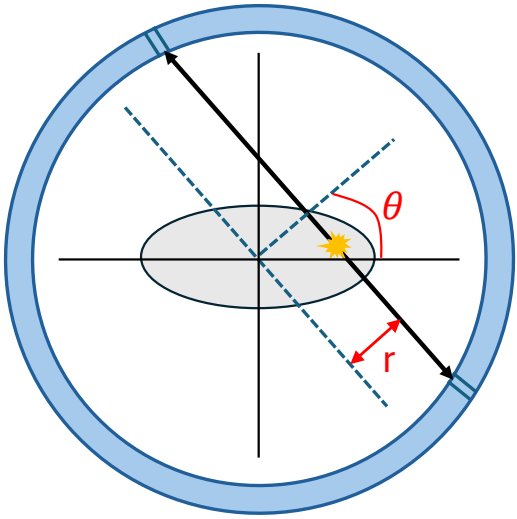

Figure 2.11: Illustration of the sinogram coordinates θ and r.

scanner, such as intercrystal scatter, positron range and non-collinearity of annihilation photons. Since analytic reconstruction methods were not used in this work, and are rarely used in modern PET scanners, we will not discuss them further.

2.4.2 Statistical iterative reconstruction: MLEM

Statistical iterative reconstruction methods have largely replaced analytic approaches in nuclear medicine because of their ability to model the noise characteristics of the measured projection data and incorporate the physics of PET and the acquisition process. Among these, the most widely used algorithms are the maximum likelihood expectation maximization (MLEM) and its accelerated variant, the ordered subset expectation maximization (OSEM). The goal is to estimate the activity distribution λ that best explains the measured projection data y. This is achieved by defining an objective or cost function that measures the similarity between the estimated projections and the measured data. Since the radioactive decay follows a Poisson process, the appropriate choice for this objective function is the Poisson log-likelihood which is maximized using the expectation maximization (EM) framework. This

leads to the MLEM algorithm, mathematically expressed as:

$$\lambda^{(\mathbf{k+1})} = \frac{\lambda^{(\mathbf{k})}}{\mathbf{H^T 1}} \mathbf{H^T} \left(\frac{\mathbf{y}}{\mathbf{H}\lambda^{(\mathbf{k})} + \mathbf{e}} \right) \tag{2.11}$$

where:

- $\mathbf{H}$ is the system response matrix that describes the physics and geometry of the imaging process.
- $\lambda^{(k+1)}$ is the updated estimate of the activity distribution after iteration k, starting from an initial uniform estimate $\lambda^{(0)}$.
- $\mathbf{H}\boldsymbol{\lambda}^{(k)} + \mathbf{e}$ is the forward projection of the current estimate of the activity distribution with the noise contribution.
- $\frac{\mathbf{y}}{\mathbf{H}\lambda^{(\mathbf{k})}+\mathbf{e}}$ is the ratio of the measured to estimated projections, representing the mismatch in projection space.
- $\mathbf{H^T}(\frac{\mathbf{y}}{\mathbf{H}\lambda^{(\mathbf{k})}+\mathbf{e}})$ is the backprojection operation, which maps this mismatch from projection space back into image space and serves as a correction term for the current image estimate.
- $\mathbf{H^T 1}$ represents the sensitivity image, accounting for the system's spatially varying detection sensitivity (normalization term).

Figure 2.12 shows the flow of the algorithm. The OSEM algorithm accelerates convergence by dividing the projection data into subsets and updating the estimate after each subset rather than using all the projections.
While the MLEM algorithm offers significant advantages over analytic reconstruction methods, it also has certain limitations that are important to highlight in the context of this work. As the number of iterations increases, image contrast improves; however, this also leads to amplification of noise, which degrades the overall SNR. Additionally, MLEM enforces non-negativity constraints on the reconstructed image, which can cause overestimation of activity in regions with low counts. Finally, compared to FBP, MLEM requires substantially more computation time due to its iterative nature. To address some of these limitations and further enhance reconstruction quality, specific implementations such as time-of-flight (TOF) and resolution modeling can be incorporated into the MLEM framework. The time-of-flight (TOF) implementation involves convolving the system matrix with a TOF kernel modeled as a

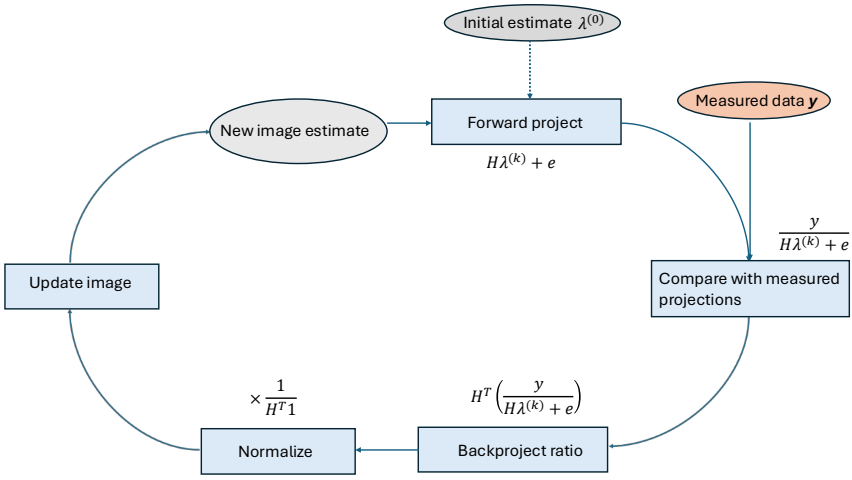

Figure 2.12: Flow diagram of the maximum likelihood expectation maximization algorithm.

Gaussian with FWHM corresponding to the system's timing resolution. This limits the backprojection and forward-projection contributions to a spatially localized region along each LOR. The resolution modeling implementation uses a Gaussian kernel with a FWHM matching the system's spatial resolution, which is applied to the image estimate at each iteration before the forward projection step.

In this work, two MLEM-based algorithms were employed to process data from the various simulated system designs. Initially, the Quantitative Emission Tomography Iterative Reconstruction (QETIR) software, an in-house developed tool, was used for the ring-based scanner simulations. However, by the time the flat-panel design was studied, another in-house developed package, PETRecon, was adopted. This tool is optimized for non-conventional geometries and leverages GPU acceleration to handle the computationally intensive components of image reconstruction.

2.4.3 Image-degrading effects

While considerable effort is invested in optimizing the design of PET systems to improve sensitivity, spatial resolution, timing and energy resolution, image quality is still affected by various physical and techno-

logical limitations. These image-degrading effects stem from fundamental physics, such as positron range, photon non-collinearity, photon absorption and scatter, as well as imperfections in the instrumentation and detection process. Recent image reconstruction algorithms play a crucial role in mitigating these effects. As was just discussed, statistical reconstruction methods, for instance, can incorporate models of the imaging system through the system matrix $\boldsymbol{H}$, as well as account for noise through a noise term e. These models enable the correction of several image-degrading factors, such as attenuation, scatter, random coincidences, and detector response non-uniformities. However, the reconstruction process is complex, and the system models are only approximations. Therefore, ongoing developments aim to improve both the modeling accuracy and computational efficiency to ensure that the reconstructed image more closely resembles the true radiotracer distribution.

Attenuation

Attenuation occurs when one or both annihilation photons fail to reach the detector, typically because they are scattered out of the FOV via Compton scattering. Photoelectric absorption in soft tissue is negligible at the high energy of PET photons (511 keV). Based on equation 2.5, the probability of a single photon traveling a distance x in tissue without interaction and reaching the detector is:

$$P_1 = \frac{I(x)}{I(0)} = \exp(-\mu x) \tag{2.12}$$

where μ is the linear attenuation coefficient at 511 keV. Similarly, the second photon traveling the remaining distance D-x has a probability:

$$P_2 = \frac{I(D-x)}{I(0)} = \exp(-\mu(D-x)) \tag{2.13}$$

where D is the total path length for both photons along the LOR. The joint probability that both annihilation photons are detected (i.e., a coincidence event) is the product of both probabilities:

$$P_{coinc} = P_1 \times P_2 = \exp(-\mu D) \tag{2.14}$$

This expression depends only on the total path length $\boldsymbol{D}$ through the object along the LOR, not on the annihilation location. This property greatly simplifies attenuation correction in PET. Currently, the most

common method for attenuation correction uses Computed Tomography (CT) data from hybrid PET/CT systems. A CT scan performed at lower X-ray energies (typically 20-150 keV) is used to generate an attenuation map, which is then scaled to 511 keV to account for the energy of PET photons.

Scatter and randoms

Although scattered photons lose energy upon interaction, discriminating them from unscattered (true) events is challenging due to the limited energy resolution of PET detectors. Additionally, true events may deposit only a portion of their energy within the detector, leading to energy measurements that overlap with those of scattered events. Consequently, energy-based discrimination alone is insufficient to fully eliminate scattered coincidences. To address this, most PET systems use a relatively wide energy window, typically between 450 and 650 keV, balancing between rejecting scattered events and retaining true coincidences. Various scatter correction techniques have been developed to reduce the impact of scattered photons on image quality, including single scatter simulation (SSS) and energy-based methods [32], [33]. Regarding random coincidences, their rate can be estimated from the singles count rate using equation 2.7, which requires direct measurement of singles at the detector level. An alternative approach involves implementing a delayed coincidence time window, where only random events are recorded, provided the delay is sufficiently long to exclude true coincidences.
A detailed discussion of these scatter and random correction techniques is beyond the scope of this work. To maintain focus on other aspects influencing PET design and performance, scattered and random events were excluded prior to reconstruction using Monte Carlo simulation tags. This choice avoids introducing additional uncertainties inherent to imperfect correction methods.

2.5 Multimodal imaging: Hybrid PET/CT

Most current clinical PET systems are integrated with a CT component, enabling the acquisition of both functional and anatomical information in a single imaging session, which is beneficial for patients. The anatomical details provided by CT enhance the localization of tracer uptake seen in the PET image, allowing clinicians to more accurately identify the anatomical structures associated with metabolic activity. In addition to

localization, CT also provides an attenuation map derived from tissue density information acquired at X-ray energies (typically 20-150 keV). This map is then converted to the PET photon energy of 511 keV to perform attenuation correction during image reconstruction - an essential step for quantitative PET imaging. To ensure proper alignment, the CT and PET components are arranged sequentially in the same scanner gantry. The patient remains on the same bed and undergoes the CT scan first, followed immediately by the PET scan, minimizing motion and simplifying image co-registration.

Having reviewed the fundamentals of PET physics, instrumentation and image formation, in the next chapter, we will review recent advancements in PET, with a detailed discussion of Monte Carlo simulation and performance evaluation standards, both of which serve as key tools used throughout this thesis.

Chapter 3

Recent advancements in PET

3.1 Introduction

Over the past three decades, PET has undergone transformative advancements that have significantly enhanced its clinical and research capabilities. One major milestone was the introduction of fully 3D acquisition and reconstruction by removing the interplane septa [34], which allowed for improved sensitivity. This was followed by the implementation of statistical iterative reconstruction algorithms that model the Poisson nature of PET data [35]. Another key development was the integration of CT imaging for attenuation correction [36]. In parallel, significant advances in detector technology have enabled PET to make a substantial leap forward in the field of molecular imaging. The introduction of fast, high light-yield LSO scintillators enabled the implementation of TOF-PET [37], [38], a concept initially proposed in the 1980s. Furthermore, the evolution of PET photodetectors from PMTs to SiPMs [39], [40] brought substantial improvements in timing resolution and compactness, establishing SiPMs as the detector of choice for the new generation of (TOF-)PET systems. More recently, efforts to enhance spatial resolution and retrieve DOI information have intensified, with monolithic detectors gaining attention due to their superior intrinsic resolution and DOI capabilities. At the system level, the pursuit of higher sensitivity has revived interest in extended AFOV designs, initially proposed in the 1990s. Several long AFOV systems have been developed, offering higher image quality, and acquisitions at lower injected dose or shorter times.

However, the high cost of the additional detectors required to extend the AFOV has limited the widespread adoption of these systems, prompting research into more affordable alternatives. To address this, several groups have proposed and simulated PET designs incorporating axial and transverse detector gaps, enabling AFOV extension without significantly increasing system cost. In addition, flat-panel PET configurations, first introduced in the 1990s, have been revisited for their potential to reduce costs further and provide the flexibility of an open PET geometry for various applications. Furthermore, the growing integration of artificial intelligence (AI) and in particular, deep learning (DL) in medical imaging has driven the development of advanced algorithms across multiple levels of the PET imaging chain. At the detector level, DL techniques have been applied to signal processing tasks; at the system level, they have been utilized to enhance and/or accelerate image reconstruction; and at the image level, they have been implemented for post-processing tasks such as denoising and image restoration.

In this chapter, we cover the most relevant advancements in PET detectors, system design and deep learning-based image restoration. We also describe the details of Monte Carlo simulations and the NEMA standards to evaluate the performance of PET systems, including modifications proposed for emerging PET designs.

3.2 PET technology advancements

3.2.1 Time-of-flight

Time-of-flight information reduces the localization uncertainty along the LOR by constraining the annihilation site. Rather than assuming a uniform probability across all voxels along the LOR, the emission probability is modeled with a kernel of finite width determined by the timing uncertainty. This distribution is typically Gaussian with a FWHM given by the localization uncertainty $\Delta x = \frac{c\Delta t}{2}$. For example, a timing resolution of 300 ps corresponds to a localization uncertainty of 4.5 cm (FWHM). Although the intrinsic spatial resolution of PET systems is on the order of millimeters, TOF measurements do not directly improve spatial resolution; instead, they improve the image SNR. Although the concept of TOF-PET dates back to the 1980s, early systems were limited by the available detector technology. The introduction of fast scintillators, such as lutetium oxyorthosilicate (LSO) and lutetium-yttrium oxyorthosilicate (LYSO), with high light output and stopping power,

enabled the real benefit of TOF-PET systems to be explored with the first commercial TOF-PET scanner (Philips Gemini TF) in 2006, which used LYSO crystals. In [41] Conti highlighted that the benefits of TOF become more pronounced in larger patients, and is essential in studies with low counts or limited transaxial coverage. Building on this, Karp et al. [42] demonstrated, using clinical data, that TOF reconstruction offers higher contrast recovery for lesions and faster reconstruction convergence, particularly in larger patients. Similarly, another clinical study [43] found a correlation between patient body mass index (BMI) and SNR gain, noting improvements in lesion definition, image uniformity, and noise reduction with TOF. Since limited-angle reconstruction is an area of interest for this work, it is relevant to consider the impact of TOF in scenarios where the angular coverage is limited. Such configurations have been explored for applications including breast imaging, in-beam PET requiring open geometries, and cost-effective designs using partial rings or flat panels. A simulation by Vandenberghe et al. [44] demonstrated that improved timing resolution reduces the number of angular views needed for a good data reconstruction. Likewise, a Monte Carlo simulation for a breast scanner design [45] showed that a two-thirds ring scanner with 300 ps timing resolution achieved performance comparable to a full-ring non-TOF scanner, as the TOF gain compensated for sensitivity losses due to missing LORs. Although this work does not explicitly compare TOF and non-TOF designs, TOF reconstruction was implemented due to the documented benefits and the suitability of the detectors used in these systems, which possess the necessary characteristics for TOF measurements.

3.2.2 Depth-of-interaction

One of the main limitations affecting spatial resolution in PET is the lack of depth-of-interaction (DOI) information, which causes radial parallax error in the transverse plane for off-center sources, and axial parallax error for oblique LORs in 3D PET or systems with extended AFOV. Several DOI-encoding methods have been developed for pixelated detectors, including multilayer crystal arrays [46], phoswich detectors [47], configurations with multiple scintillator layers each coupled to a photosensor [48], and dual-ended readout systems [49]. However, each of these methods faces drawbacks such as degraded timing resolution, reduced light collection efficiency, complex signal readout, and high manufacturing costs. Blinder et al. [50] demonstrated that using DOI information with

dual-layer LSO-LYSO crystals in a high-resolution research tomograph improved spatial resolution and partially corrected for the parallax error. A simulation study further showed that while DOI encoding improves spatial resolution in all dimensions, the most significant benefit lies in reducing radial parallax error compared to axial parallax error [12]. Thus, whether in standard AFOV or long AFOV systems, DOI capability is crucial for optimizing spatial resolution. Monolithic scintillator detectors have gained increasing attention in recent years due to their inherent DOI capability and superior intrinsic spatial resolution. These detectors have been implemented in various research prototypes and commercial small-animal PET scanners. For example, monolithic LYSO crystals measuring 25.4 mm x 25.4 mm x 8 mm have been used in preclinical scanners, achieving a volumetric spatial resolution of $1\,\mathrm{mm}^3$ in the β-cube system [51]. The performance of larger monolithic scintillators has also been widely studied. A 22-mm-thick LYSO detector achieved 1.7 mm FWHM spatial resolution using back-side readout only [52] and 1.1 mm FWHM with dual-sided readout [53]. A 15-mm-thick LYSO crystal achieved 1.8 mm resolution [54]. Moreover, a study employing a 50 mm x 50 mm x 16 mm LYSO detector with a neural network and mean nearest neighbor positioning algorithms [55] reported a 2D spatial resolution of 1.14 mm with DOI encoding across up to six layers. Despite these advances, monolithic scintillators present two major challenges: the lengthy calibration procedures required for accurate event positioning and limitations in timing estimation due to the spreading of the scintillation light over multiple SiPMs. Several studies have addressed these challenges and proposed solutions to improve both calibration efficiency and timing performance [56], [57], [58].

After presenting the key roles of TOF and DOI encoding in overcoming major limitations of PET systems, it is evident that the development of detectors with both excellent CTR and precise DOI capability is fundamental for the next generation of high-performance PET scanners.

3.3 PET design advancements

3.3.1 Long axial field-of-view PET

The pursuit of longer AFOV PET systems has been driven by two key advantages: a substantial increase in system sensitivity and the ability to perform simultaneous whole-body imaging. Extending the AFOV allows for greater solid angle coverage, enabling a large fraction of the

patient to be imaged within the same time frame. As mentioned in the previous chapter, the sensitivity gain from extending the AFOV strongly depends on the size and axial extent of the imaged object. This is well illustrated in the study by Vandenberghe et al. [23], which provides detailed calculations of sensitivity gain for both point and line sources of varying lengths as the AFOV increases. From a purely geometric perspective, for a central point source, the largest gain occurs within the first 50 cm to 1 m of scanner length, where up to 80% of the solid angle can be covered. A similar trend is observed for a 10-cm line source, representative of single-organ imaging. For longer line sources, representing volume sensitivity, the increase is less pronounced. For a 1-m line source, roughly corresponding to combined brain and torso imaging, only about 50% of events intersect the detector ring with a 1-m AFOV system, decreasing to 25% with a 2-m source. Thus, to further increase geometric sensitivity, the AFOV must be extended beyond 1 m. The authors also examined more realistic imaging situations by accounting for attenuation within the object and limited detector efficiency, both of which become increasingly important at long AFOVs due to the higher fraction of oblique LORs. These oblique LORs suffer greater attenuation in the body because of their longer photon path length in the body, while more detector material is traversed, increasing detection efficiency. However, this effect is outweighed by the increased absorption in tissue. The combined effects, including event selection criteria, are summarized in Figure 3.1 adapted from [23]. The graphs compare the sensitivity gain of extended AFOV scanners relative to a conventional 20-cm system for both a central point source and a 2-m line source. For a point source, gains of up to threefold are achieved with an AFOV of 70-80 cm. For extended sources, 1-m and 2-m AFOV systems achieve gains of approximately 15-fold and 40-fold, respectively. While single-organ imaging and lesion quantification benefit from increased point source sensitivity, the primary motivation for extending AFOVs has been to increase volume sensitivity, which is essential for comprehensive brain to torso imaging in clinical practice.

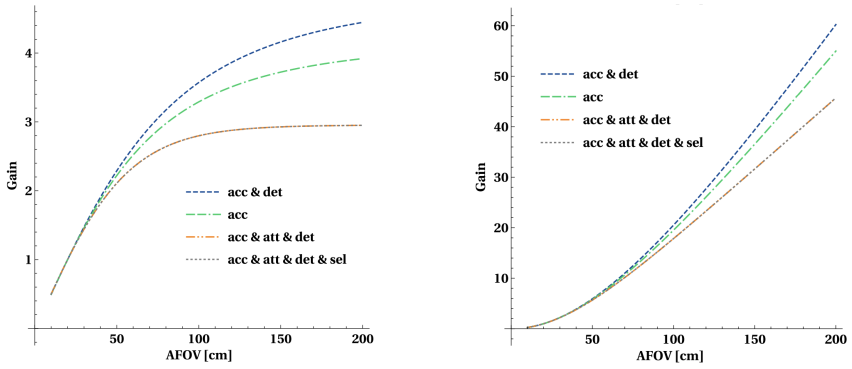

Figure 3.1: Sensitivity gain for different AFOVs versus a 20-cm AFOV PET system for a central point source (left) and for a 200-cm-long line source (right). The different curves correspond to combined effects where **acc** refers to detector acceptance, **det** refers to the detection with 20-mm-thick LYSO crystals, **att** is the attenuation caused by a 20-cm phantom and **sel** corresponds to the event selection criteria. Adapted from [23].

While the concept of long AFOV PET was first proposed in the 1990s and a few prototypes were built, it was only about a decade ago that the idea was revived with significant momentum. The EXPLORER consortium spearheaded this resurgence, a collaboration between the University of California Davis (UC Davis), United Imaging Healthcare Shanghai, and the University of Pennsylvania, which developed the first long AFOV systems. The uExplorer PET/CT scanner, completed in 2018 at UC Davis, was the first of its kind with an AFOV of 194 cm and a CTR of 505 ps. It uses LYSO crystals measuring 2.76 mm in width and 18.1 mm in depth, achieving a spatial resolution of approximately 3 mm at the center of the axial and transverse FOV, increasing to 4.7 mm at radial and axial offsets [59]. Another system of the EXPLORER collaboration, the PennPET Explorer developed at the University of Pennsylvania, initially featured an AFOV of 64 cm that was later extended to 142 cm [60]. More recently, Siemens introduced the Biograph Vision Quadra PET/CT system, a commercially available scanner with a long AFOV of 106 cm. This system, based on the Biograph Vision 600 PET/CT technology with a 26.3 cm AFOV, initially operated with a limited acceptance angle (maximum ring difference MRD=85) and was later upgraded to support

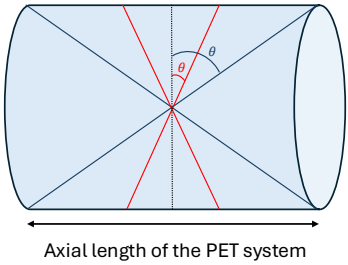

Figure 3.2: Schematic showing the axial acceptance angle in a PET system.

the full angle (MRD=322) [61]. Figure 3.2 shows a schematic of the acceptance angle θ and how it increases with the AFOV of the PET system. A comparison between images from both systems is shown in Figure 3.3 taken from [62].
To show the effect of extending the AFOV using a given detector technology, Table 3.1 compares the performance of the PennPET Explorer with three and six rings, and the Siemens Biograph Vision Quadra with MRD 85 and MRD 322. General Electric (GE) also entered this field with the digital Omni Legend PET-CT system, which features a 32 cm AFOV and is the first commercially available clinical PET/CT system using BGO crystals integrated with SiPM [63]. Furthermore, United Imaging recently expanded its portfolio beyond the uEXPLORER by introducing two additional systems based on updated technology: the uMI Panorama GS with an AFOV of 148 cm [64] and the uMI Panorama with a shorter AFOV of 35 cm [65]. The construction of PET scanners with varying AFOV lengths reflects the fact that the optimal scanner length depends strongly on the intended clinical or research application. While longer AFOV systems provide unparalleled sensitivity and enable total-body dynamic imaging, they also introduce certain challenges. These include higher rates or random and scattered coincidences from the oblique events and increased axial parallax errors due to the detection of very oblique LORs [12]. Moreover, the high cost of these systems remains a significant barrier, limiting widespread adoption in most clinical centers, which instead opt for standard AFOV PET. As a result, trade-offs between AFOV length, system performance, and affordability continue to shape the design and deployment of PET scanners.

In this thesis, we first propose and evaluate a medium-cost extended

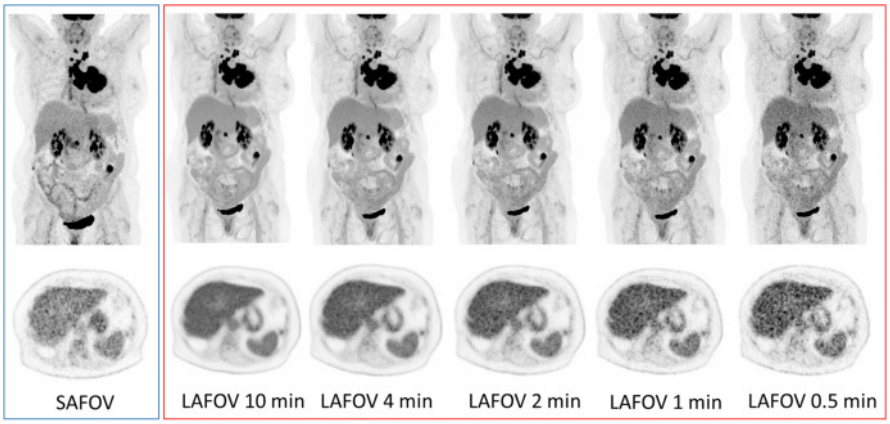

Figure 3.3: Maximum intensity projection (top) and axial (bottom) PET images of a 57-year-old female with non-small cell lung cancer. The SAFOV refers to the Biograph Vision 600 with an acquisition time of 16 minutes, while the LAFOV refers to the Biograph Vision Quadra with varying acquisition times. Adapted from [62].

Table 3.1: Characteristics and performance of the PennPET Explorer with three and six rings, and the Biograph Vision Quadra with MRD 85 and MRD 322. Values are taken from [60], [61], [66], [67].

PET system	**PennPET Explorer**		**Biograph Vision Quadra**	
	3 rings	6 rings	MRD 85	MRD 322
Crystal type & size	LYSO: 3.86 x 3.86 x 19 mm^3		LSO: 3.2 x 3.2 x 20 mm^3	
AFOV (cm)	64	142	106	
Axial acceptance angle	40°	62°	18°	52°
TOF resolution (ps)	256	250	225	228
NEMA sensitivity @ center (cps/kBq)	54	140	83	176
Spatial resolution @ center (FWHM)				
Transverse (mm)	3.9	3.9	3.1	3.4
Axial (mm)	3.9	4.4	3.4	5.5

AFOV ring-based PET design based on monolithic LYSO detectors. The system combines cost-effectiveness, modularity, superior spatial resolution, and enhanced sensitivity compared to the state-of-the-art PET systems. Detailed descriptions and performance evaluation are provided in Chapter 4.

3.3.2 Sparse PET designs

The long AFOV systems described above represent the most effective, but also the most expensive solution for increasing system sensitivity. Their cost roughly scales with the axial length, making them too expensive to most clinical centers. To achieve similar benefits without incurring such significant costs, researchers have explored optimizing system geometry. One such approach involves introducing detector gaps in the transverse and/or axial directions, enabling extension of the AFOV without adding detectors and resulting in a sparse configuration. Although this reduces sensitivity and creates a non-uniform sensitivity profile, it still allows for simultaneous imaging of multiple organs. Beyond cost reduction, sparse PET designs have been motivated by applications such as in-beam PET. The first open-type PET system, "OpenPET", was developed to accompany therapeutic beams and monitor the interactions between beam ions and irradiated tissue [68]. In another study, a Monte Carlo simulation doubled the AFOV of the Siemens Biograph mCT by introducing 4 mm physical gaps between LSO crystals within each detector block. While the extended mCT exhibited increased noise compared to the original mCT, the noise distribution remained relatively uniform [69]. The same group conducted a similar simulation study on the Siemens Biograph Vision, doubling the AFOV by adding 32 mm gaps between detector module rings, yielding an AFOV of 48 cm. However, they reported degradation in the axial spatial resolution. Continuous bed motion of the extended sparse design, with an axial extent equal to twice the axial detector block width, helped correct for the non-uniform sensitivity profile caused by these gaps [70]. In a more clinical setting, the PennPET explorer initially operated with three rings of 16.4 cm active length due to data readout limitations, leaving 7.6 cm gaps between rings. This setup inspired a simulation study where their group varied gap sizes from 1 cm to 10.9 cm and assessed performance metrics for each configuration [71]. They concluded that gap sizes should ideally not exceed half the width of a detector ring and that the optimal design depends on the intended application and clinical performance needs. Ultimately, sparse

PET designs involve a trade-off between sensitivity improvements and increased axial coverage. The configuration should be chosen based on the specific application it is intended for.

3.3.3 Flat-panel PET

Since all the systems described earlier use ring-shaped detector configurations, extending their AFOV typically requires adding numerous detectors, which significantly increases system cost. In the pursuit of further cost reductions, the concept of a flat-panel PET geometry, first introduced at IEEE MIC in 1990, has been revisited by several groups. A key limitation of this design is the missing data in the transverse direction, which results in elongation artifacts in the reconstructed image in the direction towards the panels. While ring-based PET systems provide full 2D angular coverage with a 180° projection range, flat-panel geometries inherently suffer from a reduced angular coverage due to gaps between the panels. The percentage of the projection range available is determined by both the size of the flat panels and the separation distance between them. Figure 3.4 illustrates the angular projection range in the transverse view. The limited angular coverage results in elongation artifacts in the direction of the detector panels, as shown in Figure 3.4a where the obscured regions are visible. Figure 3.4b highlights some of the missing projections (i.e., undetected LORs) caused by the gaps between the panels.

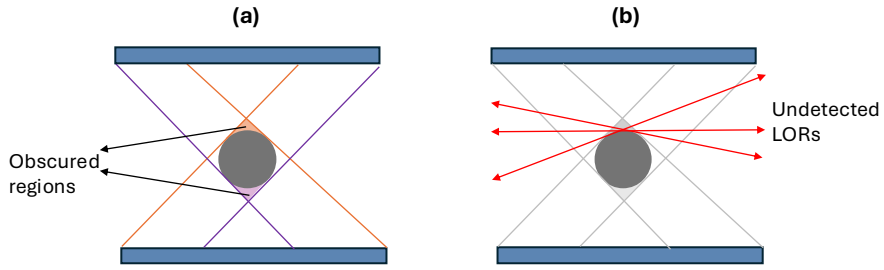

Figure 3.4: Transverse view of a dual flat panel PET illustrating (a) the obscured regions and (b) the undetected LORs due to limited angular coverage.

However, studies have shown that with sufficiently good TOF resolution, full angular coverage is not strictly necessary [45]. Various research

groups have simulated and developed flat-panel systems to benefit from the flexibility of an open geometry. Applications include breast PET systems [72], MRI-compatible PET inserts [73], and systems designed to facilitate biopsy guidance and clinical intervention during acquisition [74]. Large-scale flat-panel PET systems have also been simulated for whole-body imaging, featuring an adjustable transaxial FOVs to enhance sensitivity [75]. A recent simulation study evaluated configurations with varying DOI resolutions and TOF resolution down to 70 ps aiming to match the performance of the Siemens Biograph Vision used as a reference. The results demonstrated that reducing the panel separation increased sensitivity and improved spatial resolution, particularly when combining DOI capability with 70 ps TOF. Nevertheless, it is important to note that achieving a system-level TOF resolution of 70 ps remains beyond current technological capabilities. Our MEDISIP group previously proposed the Walk-Through PET (WT-PET), a monolithic-based flat-panel design with an extended AFOV that combines cost-effectiveness, compactness, high patient throughput and superior spatial resolution [3]. The design features two vertical flat panels, each 106 cm high and 71 cm wide, separated by a 50-cm gap. This compact design reduces detector volume and surface area, contributing to lower costs while eliminating the need for bed positioning, which supports higher patient throughput. The panels are based on monolithic detectors with DOI capabilities, allowing them to be as close as reasonably possible to the patient to maximize solid angle coverage and thus sensitivity, and to minimize non-collinearity effects, improving spatial resolution. A simulation study evaluated the performance of a TOF-capable BGO-based WT-PET design [76]. BGO was initially chosen for its cost advantage, being 2-3 times cheaper than LYSO. However, LYSO's superior TOF resolution [77] makes it a more promising candidate for this geometry, as it can mitigate elongation artifacts arising from limited angle coverage.

In this thesis, we will simulate and evaluate a LYSO-based WT-PET design, including a variant with gaps and a reduced AFOV. The methodology and results will be detailed in Chapter 5.

3.4 Performance evaluation standards: NEMA with modifications

Computer simulation has been an essential tool for designing and evaluating PET systems, whether developing new systems or modifying

existing ones. It allows for the creation of detailed models of medical imaging system design and detectors, followed by virtual data acquisition. The simulated output can then be analyzed to assess various performance metrics, providing a comprehensive evaluation before physical implementation.

3.4.1 Monte Carlo methods

Monte Carlo (MC) methods are numerical techniques based on stochastic sampling and statistical analysis, widely used in medical physics to develop nuclear imaging and therapy treatment planning systems [78]. Given the random nature of the radioactive decay and the complex interactions of radiation and particles with matter, which is the basis of medical imaging physics, analytical or experimental solutions are rarely easy to achieve. MC methods have therefore found extensive applications across nuclear medicine imaging, diagnostic radiology, radiation therapy planning, and dosimetry. In PET, MC simulations have proven to be a powerful tool, adopted by research groups worldwide. Several software packages have been developed for this purpose, with GATE (Geant4 Application for Tomographic Emission) [79] being one of the most widely used. GATE leverages the well-validated physics models of Geant4 for use in medical imaging, while also offering user-friendly features and advanced visualization tools.

GATE Monte Carlo simulations

GATE is an open-source software platform that is continuously being developed and refined to address the evolving needs of its broad user community, particularly in response to advances in imaging and radiotherapy. For PET applications, GATE enables comprehensive modeling of the entire imaging chain, from radioactive decay of the source to event detection and data processing. It allows users to define scanner design parameters, select crystal materials and properties, specify relevant physics processes, and incorporate various phantoms for simulation studies. Due to the computational demands of these processes, GATE is best utilized on high-performance computing clusters. In addition to system-level PET simulations, it supports detailed detector-level modeling, including scintillation processes and optical photon transport within the crystal [80]. These simulations are valuable tools for exploring design trade-offs and estimating what could realistically be achieved if the systems were

built. While simulations represent idealized scenarios and cannot fully capture the complexities of real-world imaging, these models have proven to be highly accurate when validated against experimental measurements from actual systems, showing good agreement with empirical data [70], [81]. As a result, they are widely used by the research community to predict detector and system performance, guide technological decisions, and optimize design parameters before prototyping. In this work, GATE is employed to simulate various PET system designs, model the entire acquisition process, and evaluate system performance through a series of phantom studies. The simulation pipeline is structured to replicate the components of a PET imaging system. First, the **scanner geometry** is defined, including dimensions and configurations (ring-based or flat-panel geometries), with support for static and dynamic setups. This stage also specifies the detector material, arrangement, and repetitions to match realistic system architectures. Second, the **source** characteristics are specified, from simplified gamma back-to-back sources to positron emitters with defined activity distributions. Voxelized sources can also be incorporated, enabling the use of digital phantoms or patient datasets for more realistic, clinical-like acquisition scenarios. Third, **phantom** geometries and materials are designed to provide a medium for positron annihilation and mimic patient-like conditions or experimental setups by accounting for attenuation and scatter. When combined with voxelized sources, voxelized phantoms offer the ability to track particles across voxels and assign different material properties based on grayscale values in images. The **physics** modeling phase involves selecting appropriate physical interaction models. Typically, the standard electromagnetic physics model is employed to account for the main processes such as Compton scattering, photoelectric absorption, and positron-electron annihilation. Additionally, the **digitizer** implements the detector responses and data processing, including modeling of energy and time resolution, dead time effects, and coincident event processing. Finally, data **output** preferences are configured to support efficient post-processing and analysis. GATE supports multiple output formats optimized for different scanners, including binary files, list mode, sinograms, and the widely used ROOT format [82]. ROOT output is particularly advantageous for handling large datasets, providing a visual interface for inspecting simulation results, troubleshooting outputs, preparing datasets for further analysis, or image reconstruction. Moreover, GATE's visualization interface enables users to preview and verify the created geometries and avoid

volume overlap before running computationally intensive simulations, thus saving time and resources. Figure 3.5 shows a visualization of a cylindrical PET system design in which a sensitivity phantom is placed.

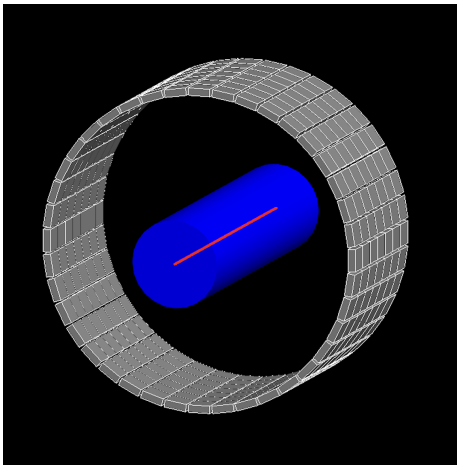

Figure 3.5: GATE visualization of a cylindrical PET system with a uniform arrangement of monolithic detectors. A linear radioactive source (in red) is embedded in a water-filled cylinder (in blue) to account for attenuation.

3.4.2 Performance evaluation standards for PET: NEMA and modifications

Accurate performance evaluation of PET systems is critical for characterizing their capabilities, benchmarking against other systems, predicting clinical performance, and guiding protocol optimization. The National Electrical Manufacturers Association (NEMA) first established standardized guidelines for PET performance evaluation in the early 1990s [83]. These standards, with only minor updates since their inception, were primarily designed for scanners with standard AFOV (typically 15-30 cm) and conventional ring geometries. As such, they do not fully account for the unique challenges and characteristics of modern PET systems, including long AFOV scanners, non-conventional designs such as sparse or flat-panel geometries or dedicated brain and organ systems. The NEMA protocols define metrics for key performance aspects such as sensitivity, count-rate capability, scatter fraction, spatial resolution, and image quality. In this section, we briefly review these standard metrics

and discuss the necessary adaptations for emerging PET designs. Several of these proposed modifications, including some presented by the PennPET Explorer group at the PSMR 2022 conference [84], aim to extend the applicability of performance assessments to long AFOV systems and unconventional geometries. While some of these suggestions have been implemented in the present work, others remain to be explored in future studies. Although NEMA performance tests were originally intended for experimental evaluation of physical systems, they have also been widely adopted in Monte Carlo simulations. In this context, they serve to validate MC models of existing scanners, predict the performance of novel system designs, or optimize parameters of existing designs for research and development purposes. The main performance metrics established by NEMA are outlined below, together with proposed modifications.

Sensitivity

According to NEMA standards, PET scanner sensitivity is measured using a 70-cm long line source of ^{18}F surrounded by five concentric aluminum sleeves, which act as a medium for the annihilation of the positrons (Figure 3.6). Sensitivity is determined through five successive measurements, where one aluminum sleeve is removed at each step. The attenuation-free sensitivity is then obtained by extrapolating these measurements to zero attenuation. To minimize dead-time losses and random coincidences, the line source should have a relatively low activity. Measurements are performed with the line source placed both at the center of the transverse FOV and at a radial offset of 10 cm, and the reported sensitivity is the average of these two values. Additionally, this setup allows plotting the sensitivity profile along the scanner's AFOV to assess variations in sensitivity across its length.

However, using a 70-cm line source raises concerns about its suitability for evaluating scanners with an AFOV larger than 70 cm, as it does not fully span the system's length and cannot accurately reflect the total number of events that are measured in a clinical setting where activity distribution often extends beyond 70 cm (e.g., across the torso). To address this limitation, it is recommended to match the length of the line source to the AFOV of the scanner or tailor it to the specific task, thereby enabling measurement of the full axial sensitivity profile. Furthermore, for non-cylindrical geometries such as flat-panel systems, the positioning of the line source should be adapted. In addition to placing it at the transverse center of the FOV, measurements should also be taken with

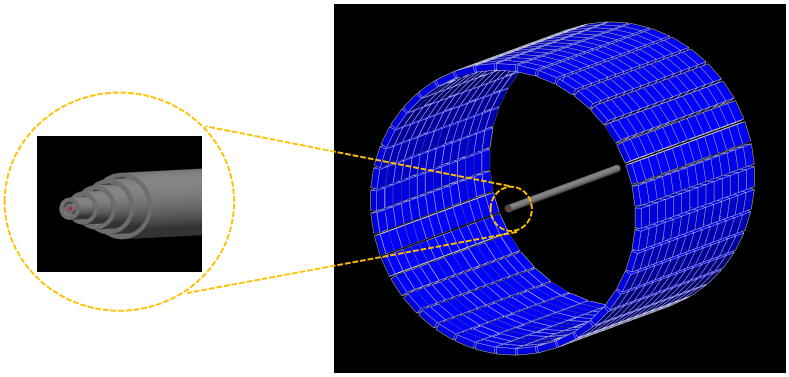

Figure 3.6: GATE visualization of the NEMA sensitivity phantom showing the line source in red surrounded by five concentric aluminum sleeves.

the source shifted by 10 cm parallel to the panels, then towards the panels. The reported sensitivity should then be the average of these three measurements, accounting for variations in angular coverage and detector arrangement.

Spatial resolution

In NEMA, spatial resolution is evaluated using point-like radioactive sources (e.g. ^{18}F or ^{22}Na) of sufficiently low activity to avoid dead time effects and random coincidences. These sources are placed at specific positions within the scanner's FOV: at the center of the transverse plane and at an axial position corresponding to 3/8ths of the AFOV, with radial offsets of 1, 10, and 20 cm from the center. The recommended reconstruction method is filtered-back-projection (FBP) without any post-processing to ensure that the resolution measurement accurately reflects the system's performance. For each source position, the PSF is analyzed by drawing line profiles along the radial, tangential, and axial directions. The FWHM of these profiles is determined by linear interpolation between adjacent voxels. The resulting FWHM values are reported as measures of the system's spatial resolution in all three orthogonal directions at the corresponding locations. This evaluation provides insight into spatial resolution variations across the FOV, which is particularly relevant for systems with extended AFOV and unconventional geometries. To

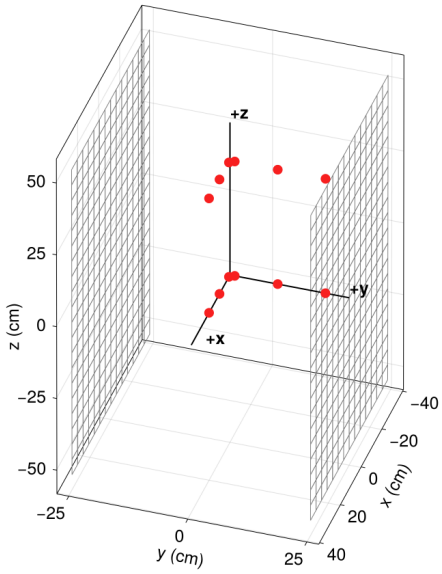

Figure 3.7: Schematic illustration of a flat-panel PET design with NEMA point sources placed along the two orthogonal directions in the transverse planes at Z=0 and Z=3/8ths of the AFOV.

achieve a more comprehensive assessment, additional point sources can be placed at intermediate radial offsets (e.g., 5 cm and 15 cm) and at axial positions between the center and 3/8ths of the AFOV. For systems with non-cylindrical geometries, it has also been suggested to assess spatial resolution along the two orthogonal directions in the transverse plane (X and Y), along the scanner's axial direction, as well as the diagonal axis, to provide a more complete mapping of the system's resolution [76] (see Figure 3.7). Furthermore, we believe that the use of statistical iterative reconstruction algorithms, as they are now the standard in clinical practice, is necessary, especially for systems with incomplete data, such as flat-panel geometries or sparse designs with large gaps, where analytical methods are not supported. However, it is important to note that iterative methods can overestimate spatial resolution when evaluating point sources in a cold background due to non-negativity constraints in the reconstruction. To mitigate this effect, several groups recommend using a warm background with sufficiently low contrast between the reconstructed point peak intensity and the background intensity [85].

Image quality (IQ)

While individual performance metrics, such as spatial resolution and sensitivity describe specific aspects of PET scanner functionality, the NEMA image quality (IQ) phantom offers a more comprehensive evaluation. It examines how these factors interact to influence the overall quality of clinical images, considering system- and reconstruction-dependent effects. The phantom is designed to resemble a human torso and contains six fillable spheres of different diameters (ranging from 10 mm to 37 mm), which simulate lesions of various sizes, along with a central low-density insert to mimic lung attenuation, see Figure 3.8a. The background is uniformly filled with an activity concentration of 5.3 kBq/ml, while the spheres are filled with higher activity to achieve a target sphere-to-background ratio of either 4:1 or 8:1. After data acquisition and image reconstruction, two main quantitative metrics are considered according to NEMA: **Contrast recovery coefficient (CRC)**, a metric that quantifies the system's ability to recover the true activity concentration contrast between the hot spheres and the background. It is defined for each sphere j as:

$$\mathrm{CRC}_j = \frac{C_{H,j}/C_{B,j} - 1}{A_H/A_B - 1} \tag{3.1}$$

where $C_{H,j}$ is the average counts in the region of interest (ROI) of sphere j, $C_{B,j}$ is the average count in the background ROIs, and A_H and A_B are the known true activity concentrations in the hot spheres and background, respectively. To ensure statistical robustness, sixty background ROIs of each size are drawn across five transverse slices: the central slice and two on each slice at ± 1 cm and ± 2 cm, see Figure 3.8b. The **background variability (BV)** reflects the noise level in the background and is computed as:

$$\mathrm{N_j} = \frac{\mathrm{SD_{B,j}}}{C_B} \tag{3.2}$$

where $SD_{B,j}$ is the standard deviation of the counts in the sixty background ROIs corresponding in size to sphere j.
While several factors contribute to background noise in PET images, random and scatter coincidences are among the most significant sources. The BV metric quantifies how these events contribute to noise in regions expected to be uniform. In this work, however, we reconstruct only true coincidence events, excluding random and scatter events. As a result the BV metric is not relevant. Instead, we use a measure that represents the

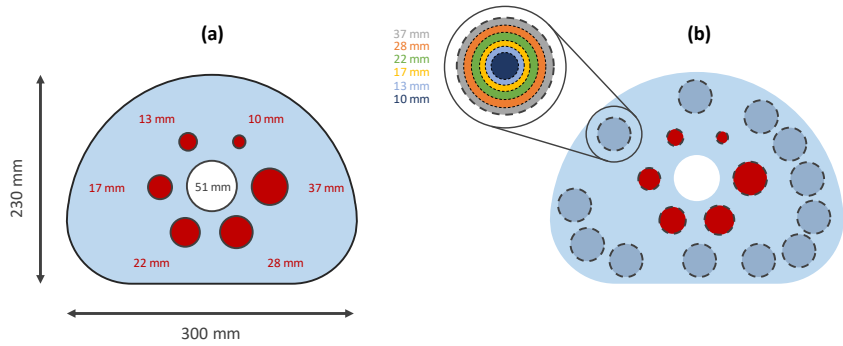

Figure 3.8: Schematic of the central transverse slice of the NEMA IQ phantom showing (a) the dimensions of the phantom, hot spheres and lung insert and (b) the placement and sizes of the background ROIs.

'detectability' of a sphere by incorporating both contrast and background noise, namely the contrast-to-noise ratio (CNR), defined for sphere j as:

$$\mathrm{CNR}_j = \frac{C_{H,j} - C_{B,j}}{SD_{B,j}} \tag{3.3}$$

It is important to note that this phantom is centered within the AFOV and does not assess the image quality across the full FOV in long AFOV systems. To address this limitation, the same phantom can be moved axially toward the edge of the scanner to evaluate how variations in axial spatial resolution and sensitivity affect image quality in peripheral regions. Additionally, the smallest sphere in the standard phantom is 10 mm in diameter, which may be insufficient for evaluating systems with high spatial resolution. To better probe the limits of resolution performance and partial volume effects, smaller spheres down to 2 mm in diameter are incorporated into what we refer to as the modified IQ phantom, see Figure 3.9. In systems, with limited spatial resolution, small structures appear blurred and underestimated in intensity due to the partial volume effect, where voxel intensities are averaged over regions containing both hot and cold areas.

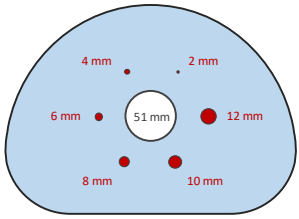

Figure 3.9: Schematic of the central transverse slice of the modified IQ phantom showing the reduced dimensions of the hot spheres.

Axial noise profile

Another phantom commonly used in simulation studies, particularly for extended AFOV and sparse PET scanner designs, is a long uniform cylindrical phantom designed to assess the axial uniformity of noise. This is especially relevant in systems with non-uniform axial sensitivity profiles or missing axial data due to detector gaps [71], [86]. The phantom typically consists of a uniform cylinder filled with a constant activity concentration, often similar to the background concentration used in the NEMA IQ phantom (e.g., 5.3 kBq/ml). It has a diameter of approximately 20 cm, while its length must be sufficient to span the entire AFOV of the system under evaluation. After image reconstruction, circular ROIs with a diameter of 10 or 15 cm are drawn at the center of the cylinder in each transverse slice. The noise level in each slice j is quantified using the normalized standard deviation, calculated as:

$$\mathrm{N_j} = \frac{\mathrm{SD_j}}{C_j} \tag{3.4}$$

where SD_j and C_j are the standard deviation and mean of voxel intensities within the ROI on slice j, respectively. Plotting N_j as a function of axial position results in an axial noise profile of the PET system. This profile offers insight into the axial uniformity of response, which is particularly important for long AFOV and sparse designs.

XCAT phantoms

The anthropomorphic eXtended Cardiac-Torso (XCAT) phantoms are computational models of the human anatomy designed for use in various medical imaging modalities [87]. They feature anatomically accurate

representations of major organs, with accurate shapes, sizes, and tissue densities. Each organ can be assigned a user-defined activity distribution and attenuation properties, allowing realistic simulation of both functional and structural imaging.
XCAT phantoms are available for both male and female anatomies across a wide range of ages, and body mass indices (BMIs). They can incorporate physiological motion, including cardiac and respiratory dynamics, which makes them particularly useful for evaluating the impact of motion on image quality. Figure 3.10 shows the activity and attenuation maps of a male XCAT phantom with a BMI of 19 used as input to the simulation. In PET imaging, XCAT phantoms are commonly used to assess clinical image quality, simulate diseases such as tumors, and explore specific imaging tasks like lesion detectability or motion correction strategies. Their flexibility makes them an essential tool for evaluating system performance, benchmarking reconstruction algorithms, and optimizing acquisition protocols.

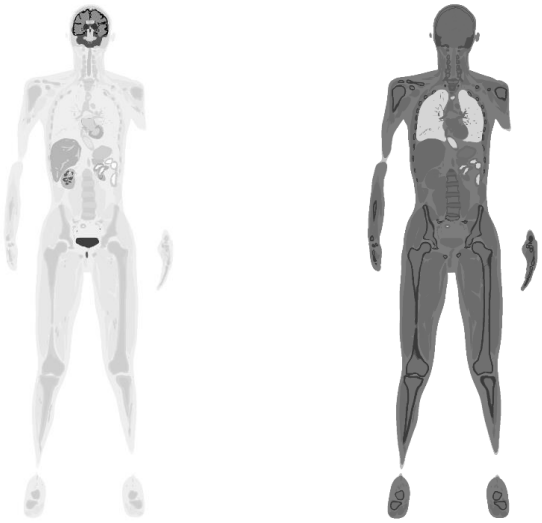

Figure 3.10: Coronal slice of the activity map of a male XCAT phantom with a BMI of 19, showing the variation in activity concentration across organs (left) and the corresponding attenuation map illustrating differences in organ attenuation (right) [87].

Throughout this thesis, we simulate the extended-AFOV PET designs in GATE and evaluate them using the performance metrics described

above. To address certain performance limitations, image-based deep learning techniques are employed. Therefore, we provide an overview of deep learning in PET imaging in the next section, setting the stage for its use in Chapter 7.

3.5 Deep learning in PET

Deep learning is a subset of machine learning that uses multiple layers of neural networks, enabling them to learn and perform tasks from data without explicit programming [88]. Although its foundations date back to the 1940s, it wasn't until a little over a decade ago that it started to gain prominence and momentum, thanks to the advances in computational power, the availability of large-scale datasets, and breakthroughs in algorithm design. Its applications now span a broad range of fields, including computer vision, natural language processing, speech and audio analysis, and autonomous systems. In medical imaging, especially radiology, deep learning has proven to be highly useful across various imaging techniques. It has been employed for lesion detection [89], [90], disease classification [91], [92], image segmentation [93], and registration [94]. Additionally, it has been used for image denoising [95], [96], [97], [98] and for reducing image artifacts caused by incomplete or limited measurement data [99].
In this work, we apply deep learning to address two major limitations affecting PET image quality: noise resulting from low-count statistics and elongation artifacts caused by the limited angular coverage inherent to flat-panel geometries. While several studies have proposed DL-based methods to tackle each limitation individually, few have considered addressing both simultaneously. Given the relevance of these challenges to our work, we will first provide a brief introduction to deep learning and an overview of convolutional neural networks (CNNs), followed by a discussion of U-Net, a widely adopted CNN architecture in medical imaging, and then review representative studies targeting these specific limitations.

3.5.1 Neural networks and convolutional neural networks

A fundamental component of deep learning is the artificial neural network with the convolutional neural networks (CNNs) being a specialized type suited for image-based tasks because of their ability to extract and learn features from raw data. **Neural networks** are computational models

inspired by the structure and function of the human brain, consisting of interconnected layers of neurons [100]. Artificial neurons or perceptrons, within a layer, are connected to neurons in other layers through weighted connections, forming altogether an input layer, one or more hidden layers, and an output layer [101]. Each neuron receives inputs x_{i}, scales them by corresponding weights, w_{i}, which represent the strength of each connection, and sums them together with a bias term b. The resulting value is passed through a nonlinear activation function f to produce an output y, which is then propagated to the next layer in the network (Figure 3.11):

$$y = f\left(\sum_{i=1}^{N} w_i x_i + b\right) \tag{3.5}$$

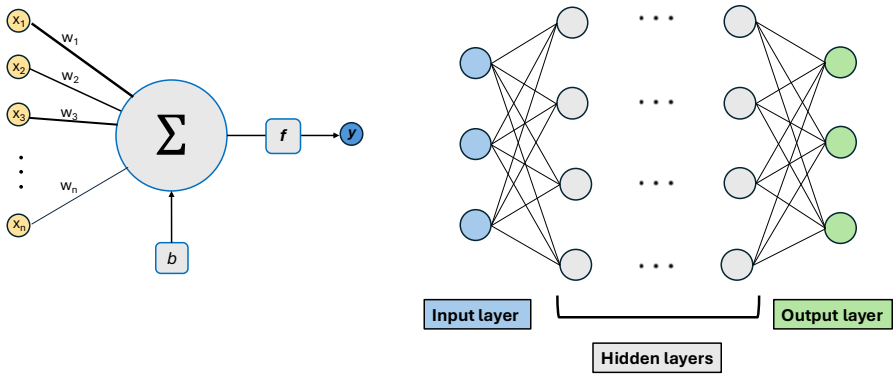

Figure 3.11: Schematic of an artificial neuron or perceptron (left) and a fully connected neural network (right).

Prior to training, the dataset is typically divided into three subsets: training (∼80%), validation (∼10%) and testing (∼10%). The **hyper-parameters**, which are user-defined, include aspects of the network architecture, training settings, and the choice of the loss function. In contrast, the weights and biases, referred to as **parameters**, are learned directly from the data during the training process. The training set is used to fit the model, where the network initially makes predictions, computes the error using the loss function, and updates the parameters through backpropagation over multiple data passes, known as epochs. The validation set is not used for parameter updates but instead monitors

the model's performance after each epoch. It helps determine whether the model generalizes beyond the training data and can indicate overfitting when validation loss increases while training loss decreases. In such cases, strategies like early stopping can be applied. Finally, once training is complete, the test set, which is unseen during training, assesses the model's overall performance.

Convolutional neural networks (CNN) are a specialized type of neural networks, particularly effective for image processing tasks [102]. They use convolutional layers that apply filters or kernels (containing the trainable weights) that slide across the input data in a process called convolution. Depending on the dimensionality of the filters and data they operate on, CNNs are typically categorized in 2D and 3D CNNs. 2D CNNs apply two-dimensional filters to process each slice independently offering computational efficiency whereas 3D CNNs use volumetric filters that operate on 3D data capturing spatial information across slices but at the cost of higher memory and data requirements. Each filter captures local patterns such as edges, textures, and shapes by computing a weighted sum (dot product) of the filter values and the input pixels at each spatial location. The result is a feature map that highlights the presence of specific features in different regions of the input image. This operation allows CNNs to efficiently learn spatial features while significantly reducing the number of parameters compared to fully connected layers. Non-linear activation functions are applied after convolution to help the network learn complex, non-linear relationships. Batch normalization layers are often added to standardize the inputs to each layer, ensuring they have zero mean and unit variance, which stabilizes and accelerates the training process. CNN architectures commonly include pooling layers between convolutional layers. Pooling operations, such as max pooling and average pooling, downsample feature maps by summarizing local neighborhoods. This reduces the spatial resolution of the feature maps, decreases computational requirements, and helps control overfitting. Additionally, many modern CNNs integrate architectural enhancements such as residual connections and dropout layers to boost training stability and overall performance.

3.5.2 U-Net architecture

U-Net is a CNN architecture originally designed for biomedical image segmentation tasks and features a nearly symmetric U-shaped structure, consisting of a contracting path, the encoder, and an expansive path, the

decoder [103] as illustrated in Figure 3.12. This architecture is also called an encoder-decoder network. The encoder includes convolutional and pooling layers that extract features from the input and reduce their spatial dimensions. The decoder gradually restores the spatial resolution of the feature maps to improve localization using transposed convolutions. A key feature of U-Net is the skip connections, which link the corresponding layers in the encoder and decoder paths to transfer high-resolution features, compensating for information loss during downsampling. U-Net has been implemented in both 2D and 3D. 2D U-Net operates on 2D image slices, making particularly suitable when computational resources are limited. In contrast 3D U-Net extends every convolution, pooling and upsampling operation into three dimensions, allowing the network to process volumetric data and capture spatial context across slices at the cost of significantly increased memory and training requirements.

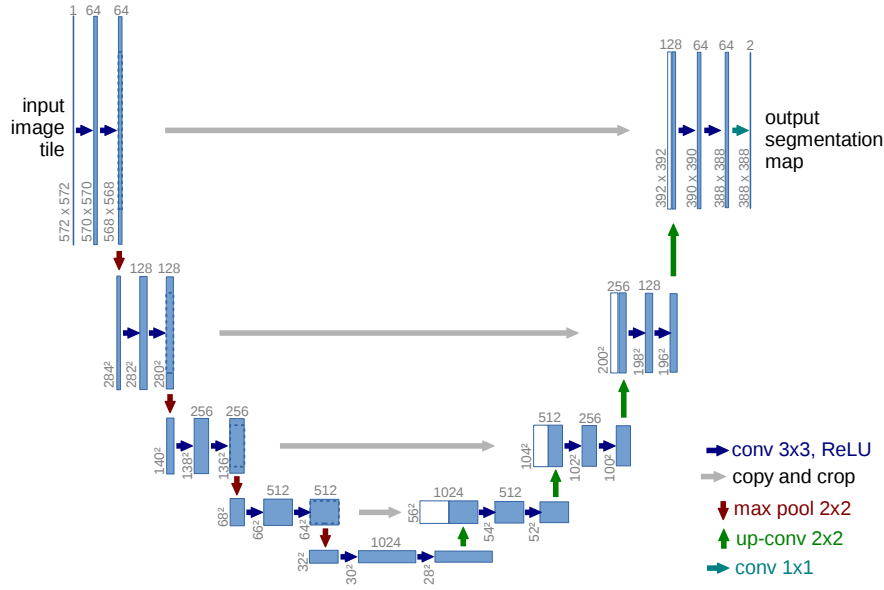

Figure 3.12: U-Net architecture: The blue boxes correspond to multi-channel feature maps with the number of channels denoted on top of each box. White boxes represent copied feature maps and the arrows denote the different operations. Adapted from [103].

3.5.3 A review on deep learning for PET image restoration

DL-based PET denoising

PET images often suffer from high noise levels, especially when acquired with low-dose protocols or short acquisition times. To address this, DL methods have emerged as effective tools for PET image denoising, providing improvements over traditional post-processing techniques like Gaussian or non-local means filters. This section offers a brief overview of recent DL-based denoising methods relevant to the work presented in Chapter 7. One early study investigated the use of a deep neural network for denoising PET images reconstructed from downsampled data [104]. They leveraged perceptual loss functions and tailored training strategies to cope with the limited availability of labeled images. Their results demonstrated that pre-training on simulated data followed by fine-tuning on real datasets enabled the network to generate images of superior quality compared to conventional Gaussian or on-local means filtering. Building on this, another study proposed a DL model capable of estimating full-dose PET images from 1/10th dose images while preserving edges, structures and texture [105]. They incorporated a composite loss function combining structural similarity features with a weighted mean squared error (MSE) and an adversarial discriminator network during training. Testing on low-dose image slices revealed significant improvements in image quality that are comparable to ground truth full-dose images. Both studies, however, acknowledged the critical need for larger and more diverse training datasets to further enhance model robustness and generalizability. Subsequent work explored variations in network architecture to further advance denoising performance. For example, a study compared convolutional autoencoders (CAEs), U-Nets, and generative adversarial networks (GANs) using a human dataset of 10 patients with solid lung nodules (most <10 mm) and 10% low-dose data obtained by listmode down-sampling [106]. Among the architectures, a carefully optimized 3D U-Net achieved the best balance between noise suppression and bias minimization for lung nodule quantification. The U-Net notably outperformed Gaussian filtering, anatomical-guided non-local means (NLM), and maximum a posteriori reconstruction techniques. In another clinical evaluation, a U-Net based on a 3D CNN was trained on chest PET scans from lung cancer patients at various noise levels [107]. Physical assessments consistently ranked CNN-denoised images higher than the original low-count PET images in terms of overall quality

and lesion detectability, particularly for data acquired at very low counts. However, the study noted that at higher count levels, comparable to routine clinical acquisitions, the added benefit of CNN denoising was limited. This finding underscores the importance of understanding the clinical context and limitations of DL methods when applied in practice. Finally, extending beyond a single-tracer applications, recent work demonstrated the feasibility of cross-tracer and cross-protocol PET denoising using transfer learning strategies [108]. Networks trained on one tracer or protocol were successfully adapted to different tracers or acquisition protocols through fine-tuning, highlighting the potential of DL approaches for versatile and robust PET image enhancement across varied clinical scenarios. It is notable that DL-based PET image denoising tools are already being implemented in clinical imaging centers. These tools help reduce radiation dose and scan time, and improve SNR and lesion detection. Several studies have reported on their development and shown their clinical benefits [109], [110], [111]

DL-based artifact reduction for limited-angle tomography

Limited-angle tomography with large gaps, as in flat-panel geometries, presents a significant challenge for image reconstruction. In conventional ring-based systems, the detectors fully surround the patient providing 360° transverse angular coverage and 180° projection angular coverage, ensuring complete sampling of LORs. However, flat-panel systems offer a reduced angular range, resulting in missing projections, and consequently, image artifacts. To address these limitations, recent studies have explored DL-based approaches to mitigate elongation artifacts in sinogram space [112] and image space [113]. While much of this research has focused on CT, PET studies have largely concentrated on addressing sparse detector designs with smaller gaps [114], [115]. Given the direct relevance to our work, we highlight a recent study on the WT-PET geometry by our group, which developed a DL-based algorithm for correcting limited-angle artifacts in image space [116]. This approach integrated a 2D U-Net in the reconstruction workflow as a regularization term and also applied separately as a post-processing step to reconstructed images, enabling a comparison between these two strategies. For training targets, a rotating WT-PET configuration covering the full angular range was employed. The dataset consisted of XCAT phantoms with varying genders, heights, and BMIs simulated using GATE. Both methods substantially reduced limited-angle artifacts; however, integrating the DL model into the

reconstruction process better preserved image sharpness, but at the cost of increased noise. In contrast, the post-processing approach resulted in a loss of contrast for the smallest lesions incorporated in the test XCAT, see Figure 3.13 adapted from the same work. The study also emphasized that the main limitation affecting both methods was not the methodology itself but more likely the lack of diversity in the training data, including uniform activity distributions across tissues, similar activity concentration ratios between different organs and identical positioning of XCAT phantoms within the scanner. This conclusion motivated the work presented in Chapter 7, where we used a larger and more diverse dataset of real patient scans acquired on a cylindrical PET scanner and simulated in a variant of the WT-PET geometry to train a DL algorithm aimed at simultaneously correcting limited-angle artifacts and denoising the reconstructed images.

In this chapter, we reviewed recent advancements in PET detector technology and design and introduced tools to simulate and evaluate the performance of different PET designs based on NEMA standards with proposed modifications. In the following chapters, we apply these tools to study various PET designs that take recent technological and design advancements into account while aiming to address persistent limitations. These include the high cost associated with extending the detector's axial coverage, the limited spatial resolution of pixelated detectors, and the lack of DOI capabilities. To address these challenges, the designs we propose in this thesis are all based on monolithic detectors, which improve spatial resolution and enable DOI measurement. In parallel, we aim to enhance system sensitivity while managing costs by exploring a moderate extension of the AFOV, sparse configurations with detector gaps, and a shift from the conventional ring-based geometry with patient bed to vertical flat panels with fast and easy patient access to increase throughput. In addition to investigating the trade-offs inherent in these design choices, we also explore how deep learning methods can be used to overcome limitations such as noise and image artifacts, thereby building upon the approaches discussed in the current chapter.

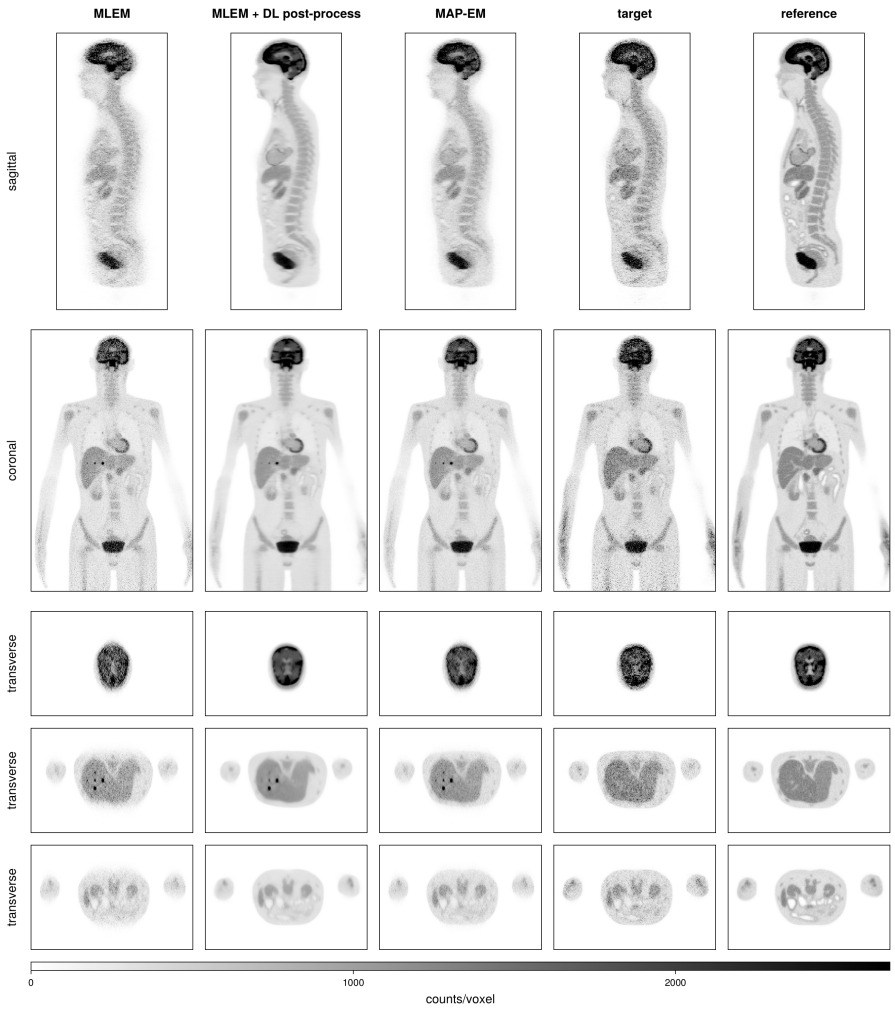

Figure 3.13: Limited angle artifact correction for the XCAT phantom, comparing implementation as a post-processing step or within the iterative reconstruction algorithm. The tenth iteration is visualized for all reconstructions. The simulation for the target and reference image did not contain any lesions, but otherwise used the same activity distribution for the phantom [116].

Chapter 4

Ring-based medium axial field-of-view PET with monolithic detectors

4.1 Introduction

Enhancing PET system sensitivity has been a primary motivation behind the development of various research and commercial medium- and long-AFOV scanners [59], [60], [61]. While these systems share the common goal of improving performance, each emphasizes different aspects. The uEXPLORER, with its 2-m-long AFOV, achieves among the highest sensitivities reported and enables full-body dynamic imaging. The PennPET Explorer, with an AFOV of 142 cm, covers most of the human body while focusing on achieving an excellent timing resolution of 240 ps. The Siemens Biograph Vision Quadra, introduced later, with an axial length of 106 cm reaches sensitivity comparable to that of the uEXPLORER, while offering a more compact system footprint, a TOF resolution of 225-230 ps and simultaneous coverage of the human torso and brain. Nevertheless, the longer AFOV of these systems results in substantially higher costs, which can limit their wider use in nuclear medicine departments. Additionally, as discussed in section 3.3.1, the sensitivity improvements from increasing the AFOV are heavily influenced by the size and axial length of the imaged object, making the optimal scanner length highly dependent on the intended imaging application. A further implication of longer AFOVs is the higher prevalence of random and scatter events. In a theoretical study on the benefits of long-AFOV PET

for region of interest quantification, Zhang et al. simulated scanners with AFOVs from 22 cm to 220 cm and demonstrated that both random and scatter fractions increase with AFOV; and at an AFOV of 111 cm, the majority of LORs were dominated by random events [117]. Furthermore, all these systems employ pixelated LSO, LYSO or BGO crystals, which constrain intrinsic spatial resolution to the pixel size and generally lack depth-of-interaction (DOI) capabilities. This limitation presents an opportunity for alternative system designs that focus on high spatial resolution and DOI performance.

In light of these facts, we propose a modular, cost-efficient PET scanner design based on monolithic LYSO scintillators. This design aims to improve spatial resolution and provide DOI information while increasing geometric sensitivity and maintaining a moderate system cost. A modular approach further allows scalable extension of the AFOV, offering flexibility to adapt the system to different clinical or research needs. The modularity supports whole-body imaging either through extended coverage or through limited bed motion, reducing the need for overly long scanners. In addition, a sparse configuration is considered to achieve a longer AFOV without additional detector modules, to balance sensitivity and cost. The sparse design can also be adapted for specific populations where a reduction in bore diameter for pediatric applications enhances geometric sensitivity. This improved sensitivity can be leveraged to lower injected dose, critical for vulnerable populations such as children, or to shorten scan times to minimize the impact of motion.

In this chapter, we present the details of the proposed medium-AFOV PET designs and evaluate their performance using Monte Carlo simulations, following the main standard NEMA metrics. We also explore the extended sparse configuration aimed at increasing the AFOV cost-effectively. For this design, we assess how sensitivity improves with axial length, and how it varies with different bore diameters. This analysis offers insights into the sensitivity trade-offs and potential benefits associated with an axial extension and bore reduction achieved by introducing detector gaps, particularly in the context of full-body coverage or pediatric imaging applications.

4.2 Materials and methods

4.2.1 Simulated scanner designs

Three PET scanner configurations were simulated, see Figure 4.1. **Design A** features a single-module setup with an AFOV of 36.2 cm, while **design B** is a dual-module setup extending the AFOV to 72.6 cm. Both configurations include 40 detector modules per ring, resulting in a bore diameter of 70 cm, slightly smaller than that of conventional pixelated-based PET systems. This reduced bore size does not compromise spatial resolution thanks to the DOI capabilities provided by the use of monolithic detectors, and even slightly reduces the spatial resolution loss due to non-collinearity. Each detector module comprises a monolithic LYSO scintillation crystal measuring 50 x 50 x 16 mm^3. Design A features seven detector rings, shown in Figure 4.1a, with a 2-mm axial gap between adjacent rings, resulting in a total scanner length of 36.2 cm. Design B doubles the number of rings to 14, as illustrated in Figure 4.1b, thereby doubling the AFOV. To further increase axial coverage, **design C** features 50% detector gaps arranged in a checkered pattern, which effectively doubles the axial length of design B to 145.4 cm without adding detectors (see Figure 4.1c). In this sparse configuration, each ring contains 20 detectors with alternating modules removed from around the ring. An advantage of these transverse gaps is the possibility to reduce the scanner bore diameter down to 35 cm, thereby increasing angular coverage and improving sensitivity, a design tailored for pediatric imaging applications.
The scanner performance was modeled with a coincidence timing resolution (CTR) of 200 ps, a coincidence time window (CTW) of 3 ns, and an energy resolution of 11.5% using an energy window of 440 - 650 keV. All simulations were performed using GATE version 9.1.

4.2.2 NEMA phantom studies

Sensitivity

For all three designs, the sensitivity was evaluated using a 70-cm-long line source emitting 511 keV back-to-back gamma photons at an activity of 5 MBq, a sufficiently low activity recommended by NEMA to minimize dead time losses and random coincidence rate. The source was placed at two positions: at the center of the scanner and 10 cm radially offset. No attenuating material surrounded the source. Data were acquired

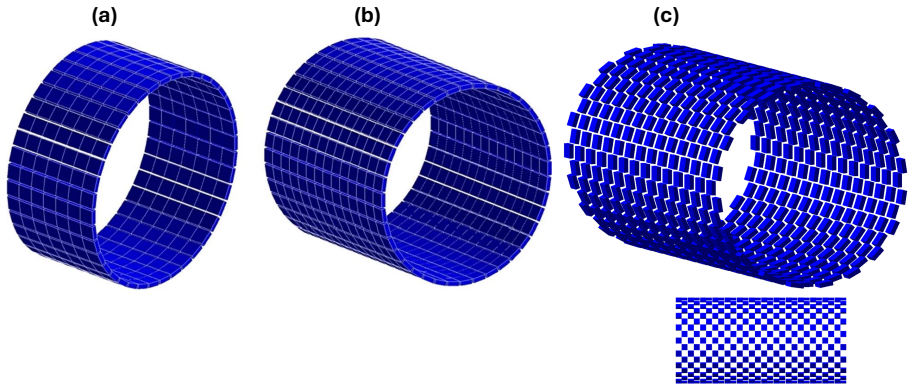

Figure 4.1: GATE visualization of (a) design A of 36.2 cm AFOV, (b) design B of 72.6 cm AFOV and (c) sparse design C extending to 145.5 cm, with a miniature side view shown below to illustrate the checkerboard pattern of the detectors.

over 30 seconds. The output ROOT files were post-processed to classify true, scattered, and random events based on Monte Carlo event tagging. Sensitivity was calculated with the following formula:

$$\text{Sensitivity} = \frac{\text{True counts detected}}{\text{Activity} \times \text{Acquision time}} \tag{4.1}$$

Similarly, the sensitivity of a Monte Carlo model of the Biograph Vision 600 scanner was evaluated to ensure that the comparison with our designs was based on simulated data rather than measured values. The simulation model and parameters were derived from published performance studies and the scanner's specification sheet [118], [119].

Spatial resolution

The system's spatial resolution was evaluated using an ^{18}F positron-emitting point-like source with a total activity of 3.7 MBq. A 0.5-mm-diameter water sphere containing the radioactivity is placed inside a cylindrical glass capillary (inner diameter: 0.52 mm, outer diameter: 1.8 mm, height: 0.9 mm). Measurements were taken at three radial positions from the center of the FOV: 1, 10, and 20 cm. For each radial location, two axial positions were examined: the center of the AFOV and a position located 3/8ths of the AFOV length, away from the center. At least one million coincidence events were collected per source position.

The raw simulation data were processed to include the detector's intrinsic resolution by applying endpoint blurring to each LOR, with values of 1.14 mm 2D resolution and 2.67 mm DOI based on previously characterized detector performance [55]. Image reconstruction was performed using the **Quantitative Emission Tomography Iterative Reconstruction (QETIR)** software developed by the MEDISIP group at Ghent University, which has been used in prior simulation studies for the total-body J-PET scanner [120], [121], [122]. A QETIR-based implementation is also used in the pre-clinical β-CUBE from MOLECUBES [51]. QETIR, developed in C++, implements the maximum likelihood expectation maximization (MLEM) algorithm with normalization and attenuation corrections. For reconstructing the simulation data, MLEM was applied for 10 iterations without subsets. Within QETIR, a sensitivity map was also generated, and the reconstructed images were produced with an isotropic voxel size of 0.5 mm. For each source location, the axial, radial and tangential spatial resolutions were quantified by calculating the FWHM of the point spread function (PSF) in the respective directions.

Image quality

To evaluate image quality, the NEMA IQ phantom, designed to resemble a human torso was simulated. The phantom contains six spheres with diameters of 10, 13, 17, 22, 28, and 37 mm, representing lesions of various sizes, and a central low-density insert to mimic lung attenuation. Simulations were run for 400 seconds using two sphere-to-background (STB) activity concentration ratios of 4:1 and 8:1, with a background activity concentration of 5.3 kBq/ml. For a 4:1 STB ratio, the total activity in the phantom is around 60 MBq. The true coincidences were reconstructed into images with 2 mm isotropic voxels using the time-of-flight-MLEM (TOF-MLEM) algorithm implemented in QETIR for 20 iterations and without subsets, assuming a coincidence time resolution of 200 ps. Attenuation correction was applied using a density map generated from the phantom geometry via a custom C++ script. Contrast recovery coefficients (CRCs) were computed according to the NEMA NU-2018 guidelines.

4.3 Results

4.3.1 Sensitivity

Design A shows a NEMA sensitivity of 29.2 kcps/MBq at the center of the FOV and 27 kcps/MBq at a 10 cm radial offset. Design B, with a longer AFOV, achieves much higher sensitivity values of 106.8 kcps/MBq at the center and 98.3 kcps/MBq at 10 cm off-center. The average of the two values for each design is listed as the system sensitivity in Table 4.1. Figure 4.2 displays the axial sensitivity profiles for both designs using the same 70-cm-long NEMA line source at the center of the FOV. Compared to design A, design B shows an approximate 1.6x peak sensitivity increase at the scanner's center. A detailed comparison of the simulated NEMA sensitivity values and relevant geometric parameters for designs A and B, along with reference values from the Biograph Vision 600 system, are presented in Table 4.1.

Table 4.1: Simulated NEMA sensitivity and geometric characteristics comparison between designs A and B and the Biograph Vision 600 from Siemens.

	Design A	Design B	Biograph Vision 600
NEMA sensitivity (kcps/MBq)	28.1	102.6	16.4
AFOV (cm)	36.2	72.6	26.1
Diameter (cm)	70	70	78
Crystal thickness (mm)	16 (LYSO)	16 (LYSO)	20 (LSO)
Detector surface ($\times 10^6 mm^2$)	0.70	1.40	0.62
Scintillator volume ($\times 10^6 mm^3$)	11.20	22.40	12.45

Figure 4.3 shows the cumulative sensitivity as a function of the scanner's axial length, allowing a comparison between designs B and C. While design C exhibits lower sensitivity in the central 70 cm due to axial gaps, it provides wider axial coverage, which is useful for studies needing full-body imaging. Additionally, the checkerboard pattern of the gaps enables a reduction in scanner bore diameter, improving sensitivity and is particularly advantageous for pediatric imaging. Figure 4.4 demonstrates the effect of decreasing the bore diameter on system sensitivity: halving the diameter results in a 50% increase in sensitivity across the entire axial length of the scanner.

For the remaining phantom studies, we focus on designs A and B for further evaluation. Design A offers the advantage of enhanced sensitivity

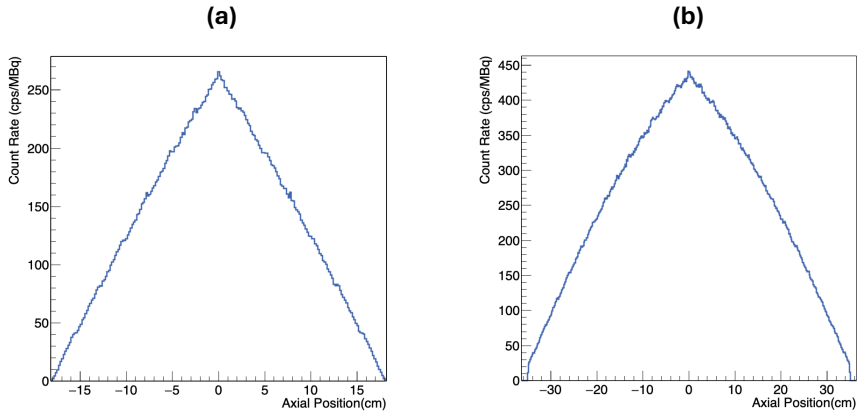

Figure 4.2: Axial sensitivity profiles at 0 cm radial offset for (a) design A and (b) design B, using a bin width of 1.65 mm.

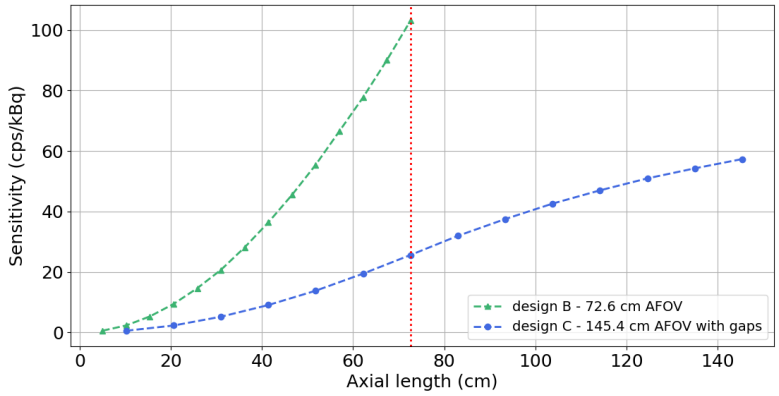

Figure 4.3: Sensitivity versus axial length for designs B and C, measured using a centered NEMA line source. The red dashed line marks the AFOV corresponding to design B to compare with design C.

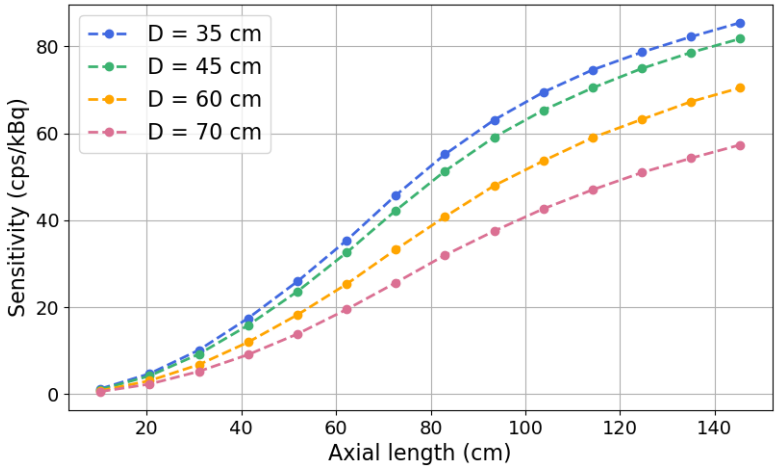

Figure 4.4: NEMA sensitivity as a function axial length for design C, 145.5 cm AFOV with 50% gaps at varying bore diameters.

with only a moderate extension of the AFOV compared to conventional standard AFOV systems. A potential upgrade involves combining two modules of design A to achieve the longer AFOV of design B, which significantly boosts sensitivity and enables torso imaging without bed translation.

4.3.2 Spatial resolution

Tables 4.2 and 4.3 show the spatial resolution results for both scanner designs, including detector blurring as well as contributions from positron range and non-collinearity as simulated in GATE. The radial, tangential, and axial FWHM values for the point sources at various radial and axial positions remain below 2 mm, with minimal variations across both the transverse and axial FOVs for each design. It is noteworthy that iterative reconstruction methods yield superior spatial resolution compared to analytical algorithms such as filtered-back-projection (FBP). For both designs, the radial FWHM does not deteriorate as the point source is moved radially outward, which is expected due to the DOI capability of the monolithic detectors that effectively mitigates radial parallax error. In terms of axial resolution, the highest FWHM values are observed at the center of the FOV, specifically at position (1,0,0) cm for both

systems.

Table 4.2: Spatial resolution FWHM (mm) for design A

	Radius (cm)	Radial (mm)	Tangential (mm)	Axial (mm)
AFOV center	1	1.44	1.36	1.45
	10	1.46	1.41	1.25
	20	1.48	1.38	1.23
3/8 AFOV	1	1.34	1.32	1.23
	10	1.41	1.38	1.24
	20	1.41	1.26	1.14

Table 4.3: Spatial resolution FWHM (mm) for design B

	Radius (cm)	Radial (mm)	Tangential (mm)	Axial (mm)
AFOV center	1	1.45	1.48	1.36
	10	1.46	1.44	1.32
	20	1.50	1.34	1.24
3/8 AFOV	1	1.37	1.37	1.31
	10	1.39	1.35	1.20
	20	1.44	1.31	1.17

4.3.3 Image quality

The tenth iteration of the reconstructed NEMA IQ images, along with the CRC curves as a function of iteration number for designs A and B are shown in Figure 4.5. The sphere-to-background activity concentration ratio was 4:1. Both reconstructions demonstrate good image quality, with all spheres clearly visible, including the smallest one (10 mm diameter), which exhibits a discernible contrast. The CRC values converge around iteration 10, ranging from 50-60% for the smallest sphere to about 90% for the largest. For design B, the IQ image exhibits more noise, and the smallest sphere shows reduced contrast compared to design A. Since the contrast difference is limited to the smallest sphere and the overall image of design B appears noisier, this effect can be attributed to the coarser sampling of the sensitivity image during reconstruction due to software limitations. A noisy or undersampled sensitivity image propagates into the reconstruction, leading to increased image noise and affecting small structures where resolution limits are probed.

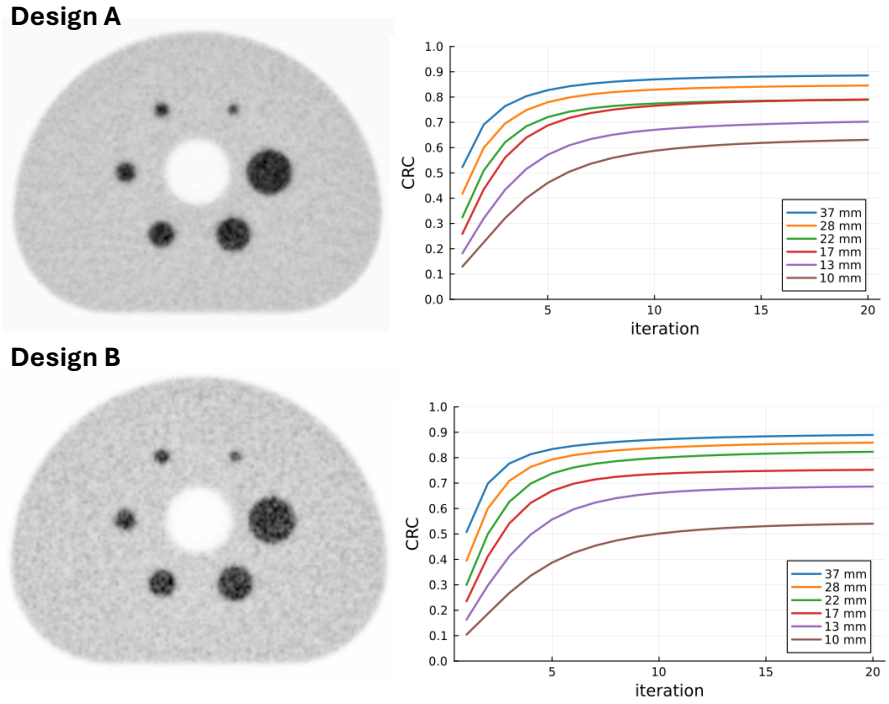

Figure 4.5: Tenth iteration of the reconstructed IQ image (left) and contrast recovery coefficient (CRC) values (right). The sphere-to-background ratio was 4:1, and the data acquisition time was 400 s.

4.4 Discussion

Design A with an AFOV of 36.2 cm, achieves 71% higher sensitivity than the simulated Biograph Vision 600, as shown in Table 4.1. This improvement mainly results from a 40% increase in AFOV and a reduction in bore diameter, both enhancing geometric efficiency and coincidence detection probability. Although the Biograph Vision 600 uses thicker scintillation crystals, which theoretically improves photon stopping power, most 511 keV photons are absorbed near the entrance surface due to exponential attenuation. As a result, the benefit of extra thickness is limited. Additionally, thicker crystals often lead to decreased timing resolution, increased parallax error, and higher system costs. A previous study by Surti et al. [123] showed that increasing AFOV with shorter crystals can achieve greater sensitivity improvements than using thicker

scintillators, supporting our design strategy. This moderate AFOV extension provides a noticeable improvement in sensitivity compared to conventional PET/CT systems, making it particularly useful for applications like organ-specific imaging, without the high costs of large AFOV systems. Furthermore, the results show nearly a fourfold increase in sensitivity when comparing design A to B, which features a doubled AFOV of 72.6 cm. This scaling follows the expected near-quadratic dependence of sensitivity on AFOV length due to the increasing number of possible axial LORs. Design B therefore offers a compelling solution for multi-organ imaging, enabling simultaneous coverage of multiple organs within the torso or both the brain and upper torso without the need for bed motion. This not only enhances clinical efficiency but also improves imaging performance. For cases where an even larger AFOV is needed, introducing detector gaps can extend coverage without additional cost. However, design C was only assessed in terms of sensitivity. While this is a critical performance metric, further phantom studies are needed to evaluate image quality and to characterize potential non-uniformities introduced by the gaps. The main advantage of the sparsity of design C lies in its gap arrangement, which allows for a reduced bore diameter. This configuration boosts sensitivity and is particularly well-suited for pediatric applications. It is also shown in Table 4.1 that design A has slightly less scintillator volume and 13% more detector surface than the Biograph Vision 600. This is due to its longer AFOV and smaller bore diameter. While the Biograph Vision 600 requires more detector surface in the transaxial FOV to cover the perimeter of its 78 cm bore, its larger scintillator volume results from the thicker crystals, which provide only marginal, if any, sensitivity gain.

An additional advantage of designs A and B is their use of monolithic detectors, which offer superior intrinsic resolution and DOI capabilities. These capabilities help mitigate radial parallax error, leading to a more uniform radial system resolution when point sources are moved off-center, as reflected in the results. The FWHM values show a consistent sub-2 mm spatial resolution across both the axial and transverse FOV, enabling detection of small lesions and abnormalities and making quantification accuracy independent of the source position within the patient. Compared to the existing standard and large AFOV systems with high sensitivity, both designs achieve approximately a 50% improvement in spatial resolution and off-center points are not affected by radial parallax error thanks to the DOI information. For the axial resolution, the slightly higher

FWHM observed at the center of the FOV may be attributed to highly oblique LORs, which cannot be fully corrected by DOI information given its limited resolution (2.67 mm). However, if axial parallax were the main contributor, design B would be expected to exhibit poorer axial resolution than design A at the center, owing to its longer AFOV and therefore more oblique LORs. Nevertheless, this trend was not observed. The measured difference between the two designs was only about 0.1 mm, which lies within the expected margin of error. Thus, these results do not provide sufficient evidence to conclude a significant impact of axial parallax on the axial resolution of our designs. A previous simulation study followed by measurements reported only a slight degradation in axial FWHM when extending the AFOV from 64 to 142 cm even without DOI information [12], [60], [81]. In reflecting on these results, several factors should be considered for future studies. First, according to NEMA guidelines, one-dimensional response functions should be formed along profiles through the image volume, with the width of the response function in the two orthogonal directions extending to about twice the expected FWHM. However, in this study, the width was limited to a single pixel, which makes the measurement more susceptible to noise. This choice may have caused fluctuations and contributed to the variation seen in axial resolution. Additionally, iterative reconstruction was used, which generally provides better results than filtered-back-projection (FBP) because of the non-negativity constraint. To reduce this effect, embedding the point-like sources in a warm background could be considered. Furthermore, iterative algorithms depend on implementation, meaning that choices such as modeling of physics, noise handling, and convergence criteria can lead to slight differences in results, so caution is needed when comparing values from different reconstruction software. Lastly, since the measured FWHM values were below 1.5 mm, a voxel size smaller than 0.5 mm is recommended, however, this was not possible due to limitations of the reconstruction software.

In terms of image quality, the CRC values are highly dependent on the chosen reconstruction parameters. For example, a study on the uEXPLORER demonstrated that both voxel size and point spread function (PSF) modeling significantly affected CRC values, particularly for the smallest sphere (10 mm) which increased from 49.8% without PSF to 69.2% with PSF and a reduced voxel [59]. In our work, the CRC values shown in Figure 4.5 were obtained using a 2 mm voxel size without PSF modeling. Further optimization of reconstruction settings

would likely improve these values. Even so, designs A and B achieved CRC values ranging from 50-60 % up to 90 %, which is comparable to current clinical systems, including the recent long AFOV scanners. The assumed time-of-flight (TOF) resolution of 200 ps, consistent with expected performance for such a system, contributed to enhanced effective sensitivity and improved SNR and overall image quality. Although it might be a bit optimistic, we do not anticipate a substantial degradation in image quality if the TOF resolution is slightly worse (e.g., 300 ps), although this warrants further investigation.

4.5 Conclusion

In this work, we demonstrated the benefit of a moderate AFOV extension by adding detectors, which improved sensitivity, and of a larger extension achieved through the introduction of detector gaps without requiring additional detectors. We also examined the use of monolithic detectors and their positive impact on achieving uniform spatial resolution across the FOV. Nevertheless, reconstruction software and parameter choices must be carefully considered, as they directly affect spatial resolution and overall image quality. These aspects will be addressed in the following chapter, where we build on the choice of monolithic detectors and the availability of DOI and introduce a novel system geometry with a different detector arrangement, aiming to further reduce costs while addressing key clinical needs such as higher throughput.

Chapter 5

Flat-panel PET geometries with monolithic detectors

5.1 Introduction

In the pursuit of more cost-effective and widely accessible PET designs that can match the sensitivity of existing medium- and long-AFOV systems, there has been growing interest in novel geometries and detector configurations driven in part by advances in time-of-flight (TOF) technology. Conventional PET systems use a ring-shaped detector configuration, which requires adding many detectors to extend the AFOV while maintaining full angular coverage in the transverse plane. Since detector modules are the main cost driver, the total system expense increases linearly with the AFOV. Although long-AFOV systems provide high sensitivity, enabling shorter scan times and/or lower injected doses, the limited gains in throughput and tracer savings are not enough to justify the higher acquisition and maintenance costs. Additionally, a large part of examination time is spent on patient positioning, which limits throughput even when scans are faster. Therefore most clinical centers and nuclear medicine deparments still rely on conventional standard-AFOV PET scanners. Various strategies have been explored to reduce system costs, including designs with detector gaps [69], [71], [86], [124] and the use of less expensive scintillator materials such as plastic scintillators [125]. Building on these efforts, our research group has moved away from the conventional cylindrical geometry and proposed a novel extended flat-panel PET design based on DOI-capable, high-resolution monolithic detectors [3]. This setup features two vertical panels, each measuring

106 cm in height and 71 cm in width, separated by a 50-cm gap.These dimensions were based on a study that first considered anthropometric and ergonomic factors and then analyzed the body sizes of 40 PET/CT patients randomly selected from the database at the University Hospital of Liège [3]. Compared to existing long-AFOV cylindrical designs, this flat-panel configuration provides similar sensitivity while offering improved resolution and DOI capability, along with higher throughput and a smaller footprint at a reasonable cost.

Monolithic detectors provide better intrinsic resolution than pixelated detectors, which are limited by pixel size. Their DOI capabilities reduce the parallax effect and enables the positioning of the panels closer to the patient. This enhances the axial angular coverage compared to a cylindrical system with a similar AFOV. Throughput is further improved by eliminating bed positioning, as patients stand between the two panels. Based on sensitivity differences, Vandenberghe et al. [3] estimated a threefold increase in throughput over standard-AFOV systems and 1.2- to 1.4-fold increase compared with long-AFOV designs like the Biograph Vision Quadra operating at full acceptance angle. Additionally, the vertical orientation of the panels and absence of patient bed reduce the system's footprint, which is advantageous in nuclear medicine departments where space is often limited. Cost efficiency is another advantage of this geometry. Compared with the geometry of design B from Chapter 4, the flat-panel design uses 1.7 times fewer detectors for roughly the same axial length. Furthermore, monolithic scintillators are less costly to produce than pixelated crystals (in fine pixels of less than 2 mm) because they do not require crystal cutting.

One drawback of the flat-panel geometry is the incomplete angular coverage in the transverse direction, which causes elongation artifacts in the reconstructed images. However, studies have indicated that with sufficiently good time-of-flight (TOF) resolution, full angular coverage is not always necessary [45]. While other groups have explored flat-panel concepts for open geometries of adjustable AFOVs [72], [86], [126], our group simulated an early version of our proposed flat-panel design called the Walk-Through PET (WT-PET) using BGO scintillators [76]. BGO was initially selected because it is 2-3 times less expensive than LYSO, helping to reduce system costs. Still, the superior TOF resolution of LYSO makes it a more suitable choice for reducing elongation artifacts in the flat-panel design.

In this chapter, we present simulation studies of two flat-panel configurations based on the WT-PET geometry. The first design retains the same AFOV as the WT-PET while the second is a more cost-efficient configuration featuring axial gaps and a reduced AFOV. In this sparse configuration, detector costs associated with the switch to LYSO are reduced by introducing gaps and limiting the detector arrangement to eight rows. Given the non-cylindrical geometry and relatively long AFOV of the proposed designs, certain modifications and additions to the standard NEMA-recommended tests (as described in chapter 3) were implemented to enable a more comprehensive system evaluation.

5.2 Materials and Methods

5.2.1 System design specifications and simulation parameters

The long flat-panels (L-FP), based on the original WT-PET design, consists of two flat panels placed 50 cm apart. Each panel contains 20 rows of fully populated monolithic LYSO detectors measuring 50 x 50 x 16 mm^3, with a 3-mm gap, resulting in an AFOV of 106 cm. Horizontally, a width of 71 cm is achieved by arranging 12 detector blocks with a 10-mm gap between each. The sparse WT-PET configuration, referred to as the SpM-FP, features eight axial rows of detectors with 28-mm gaps between rows, achieving an AFOV of 60 cm. Each gap includes the initial 3-mm spacing plus an additional 25 mm, which is half the size of a detector. This approximately half-detector gap extends the AFOV with limited sensitivity loss and maintaining image quality, as supported by previous research [71]. In addition to these performance considerations, the row-sparse layout is also an engineering choice: introducing sparsity along the axial direction is simpler than for instance implementing 2D checkerboard patterns as in Chapter 4, which would require irregular detector placement and more complex mechanical assembly. With an AFOV of 60 cm, only limited panel movement is necessary to image the brain and torso, similar to the L-FP setup. Schematics of the WT-PET design and both configurations are shown in Figure 5.1. The axial acceptance angle of the L-FP is 65° and reduced to 50° for the SpM-FP. A coincidence timing resolution of 300 ps FWHM was chosen, corresponding to the expected performance of the system, based on a published work by Carra et al. [58]. The average spatial resolution of the LYSO monolithic detectors used for detector blurring is 1.14 mm FWHM parallel to the

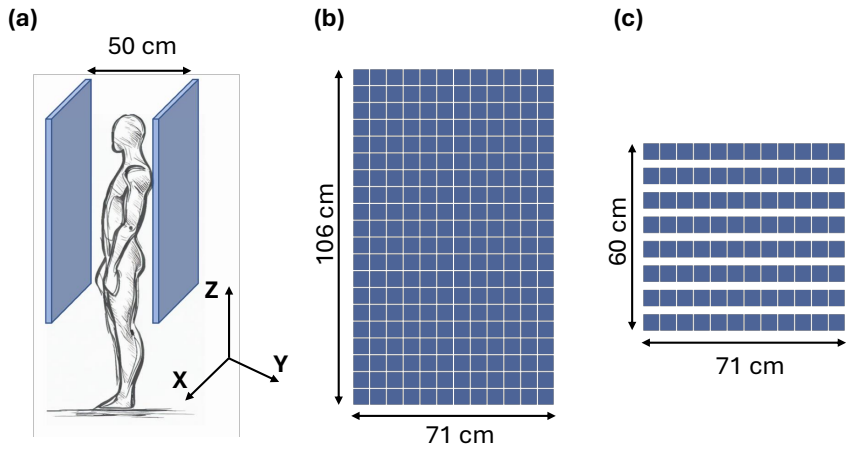

Figure 5.1: (a) Schematic view of the WT-PET concept, (b) L-FP design, (c) SpM-FP design with 28-mm axial gaps and a reduced AFOV.

detector face and 2.67 mm FWHM along the depth as reported in [55] for measurements on the same detector.

Table 5.1 summarizes the differences in system specifications and simulation parameters. The coincidence time window (CTW) chosen for the SpM-FP and L-FP designs was 4 ns and 5 ns, respectively (calculated from the length of the most oblique LOR present in the system). The energy resolution was set to 11.5% for LYSO (455-645 keV window). The sources are simulated as ^{18}F positrons, including the positron range and the physics of the non-collinearity. The exact gamma photon interaction time and position of the coincident events are recorded in the detector. The hits are grouped and saved as single events, and the coincidence sorting is done in GATE. No cut was applied to the axial acceptance angle.

To reconstruct the images from the simulated data, **PETRecon** was used, an iterative list-mode image reconstruction package developed at MEDISIP and optimized for the WT-PET geometry. It is written in Julia, a high-level programming language designed for optimal GPU performance [127]. The true coincidences (511 keV photons originating from the same annihilation event and not scattered in the phantom) were reconstructed using the Maximum Likelihood Expectation Maximization (MLEM) algorithm without subsets. The system's timing, detector spatial resolution, and DOI were modeled before reconstruction. The

Table 5.1: L-FP and SpM-FP design specifications and simulation parameters.

	SpM-FP	**L-FP**
AFOV (cm)	60	106
Axial gap size (mm)	28	3
Detector array size	8x12	20x12
Number of monolithic detectors	192	480
Detector surface ($\times 10^6 mm^2$)	0.48	1.20
Detector volume ($\times 10^6 mm^3$)	7.68	19.20
Axial acceptance angle	50°	65°
Coincidence time window (ns)	4	5
Coincidence time resolution (ps)	300	300

GATE simulation records the exact timestamps and interaction positions of the two coincident events. Before reconstruction, the measured data were blurred by applying Gaussian kernels with FWHM values of 300 ps for time, 1.14 mm and 2.67 mm for spatial coordinates, corresponding to the 2D intrinsic resolution and DOI, respectively. These values reflect the average intrinsic performance of the monolithic detector. Although this approach simplifies the real behavior of such detectors, whose resolution typically worsens near the edges and varies with interaction depth, it offers a reasonable approximation. The accuracy of this homogeneous model is assessed in the spatial resolution study, which includes a spatially varying resolution model based on data from [55].

5.2.2 Phantom studies for performance evaluation

Sensitivity

The sensitivity of the SpM-FP and L-FP configurations was simulated using the NEMA standard 70-cm long line source placed at the center of the scanner and at 10-cm radial offset along two directions: parallel to the panels (X-axis) and towards the panels (Y-axis). To evaluate the axial sensitivity profile across a 106-cm AFOV for head and torso scanning, a 106-cm-long line source was placed at the center. In the SpM-FP, the detector panels were moved vertically relative to the source to cover a scanning FOV of 106 cm, which was then extended by 15 cm at both the top and bottom, resulting in a total scanning FOV of 136 cm, as illustrated in Figure 5.2. With the 15-cm extension on both ends,

the head will be positioned at the center of the AFOV at the end of the scan, improving statistics for the brain region on one side and the pelvic area on the other. For comparison, the same source was also simulated in the L-FP. For both line sources, a 1 MBq ^{18}F positron source was used in water, surrounded by one to five concentric aluminum attenuating sleeves (2.5 mm thick). The results were extrapolated to determine the attenuation-free system sensitivity. To simulate attenuation in a human body with a relatively low Body Mass Index (BMI), we encase the 106-cm line source with a 20-cm diameter water cylinder.

Spatial resolution

Twelve ^{18}F positron point-like sources with a diameter of 0.5 mm were simulated to evaluate the system's spatial resolution following the adapted NEMA protocol. Six sources were positioned at the central transverse slice with offsets of 1, 10, and 20 cm along the X- and Y-axes, and another set of six sources was placed at the transverse slice located at 3/8ths of the AFOV. According to the NEMA standards, the voxel size of the reconstructed point source should not exceed one-third of the expected FWHM in all directions. Given the anticipated spatial resolution range of 1-2 mm, the images were reconstructed using an isotropic voxel size of 0.25 mm. Because dual flat-panel systems measure incomplete data, due to the side gaps, filtered back-projection results in image artifacts [128]. For a more realistic assessment of image resolution, the MLEM algorithm was used instead, without any smoothing or resolution modeling in the reconstruction. To prevent artificial resolution enhancement caused by iterative reconstruction [129], all point sources were embedded in a warm background. The activity concentration ratio of point source-to-background was set to 160:1. Additionally, the source counts were subsampled prior to reconstruction to achieve a reconstructed point source-to-background contrast ratio in the image between 0.1 and 0.2 following the recommendations of a comprehensive study on spatial resolution assessment with iterative image reconstruction [85]. For each source position, a minimum of 100,000 true coincidence events were used for image reconstruction. The background reconstruction was subtracted from the combined source and background reconstruction to generate the source-only image, see Figure 5.3. Line profiles in all three directions of each source's point spread function (PSF) were drawn, with the width of the response function in the two orthogonal directions extending to about twice the corresponding expected FWHM and linear interpolation

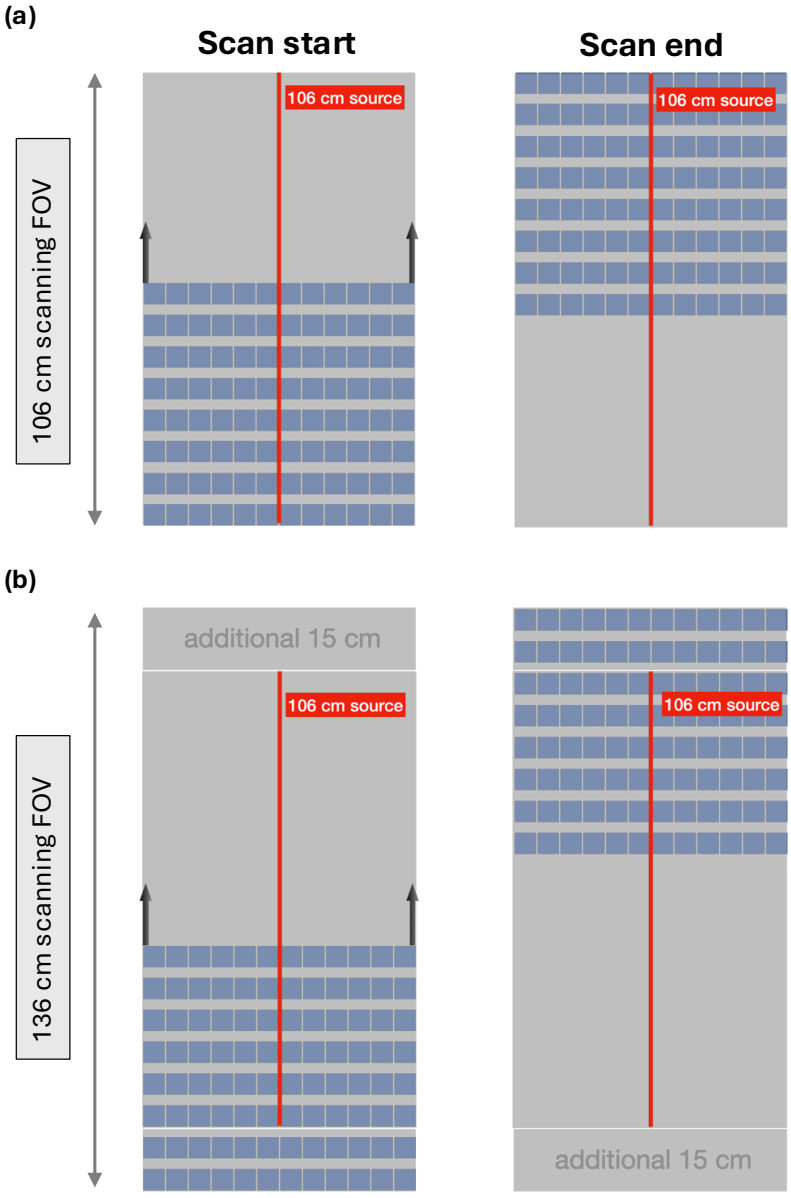

Figure 5.2: (a) Schematic illustration showing the 106-cm line source simulated in the SpM-FP with upward panel motion to cover a scanning FOV of (a) 106 cm and (b) 136 cm (106 cm with an additional 15 cm at the top and bottom).

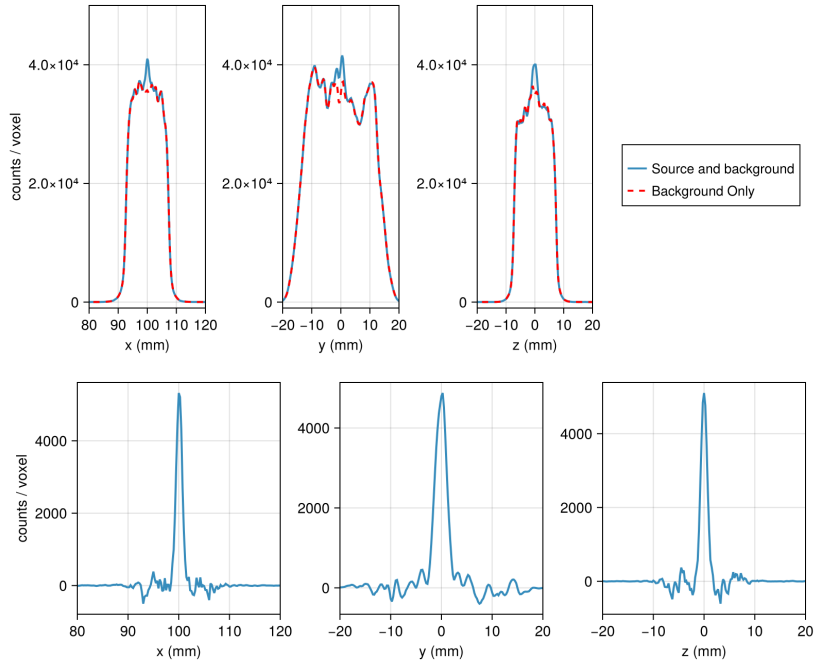

Figure 5.3: Line profiles of the point spread function of the point source at (10,0,0) cm for (a) source and background in blue and background only in red for a ratio of 160:1 with subsampling, and (b) source only after background subtraction.

was performed to evaluate the FWHM. The reported values correspond to the 50th iteration, at which convergence was observed.

Spatially varying detector resolution

The reported spatial resolution results incorporate a uniform model of the detector's spatial resolution/DOI based on a previous study of the same detector [55] which measured an average intrinsic 2D resolution of 1.14 mm across the entire detector and a DOI resolution of 2.67 mm over all six layers. In that study, the authors presented a 2D spatial resolution map showing a uniform resolution in the central 40 x 40 mm^2 region, with degradation near the edges, extending up to 5 mm from each edge, see Figure 5.4. To evaluate how this non-uniform detector resolution affects system resolution, a spatially varying detector response function was implemented for an off-center point source. This function

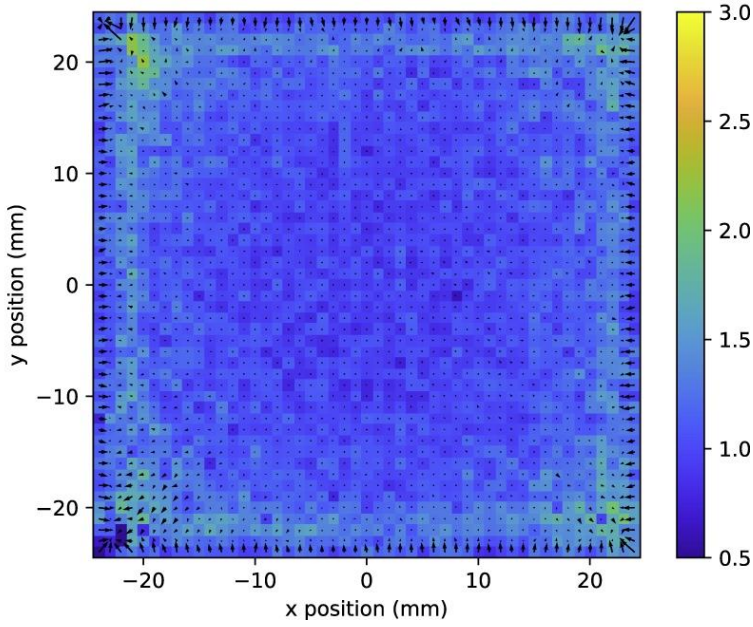

Figure 5.4: Spatial resolution as FWHM (mm) per calibration position for detector with 0.6 mm diameter calibration beam. The bias vectors are indicated as arrows for neural network positioning. Adapted from [55].

maintained a constant resolution of 1.02 mm in the central 40 x 40 mm^2, gradually increasing to 1.35 mm at the edges, averaging to the reported 1.14 mm for the entire detector. The model was also adjusted to account for DOI resolution degradation in the two layers closest to the SiPM array. A constant DOI of 2.4 mm was assigned to layers 1 through 4, while layers 5 and 6 used a DOI of 3.7 mm, resulting in an average DOI resolution of 2.67 mm across the full detector volume. These values were weighted based on the percentage of detected events in each layer, calculated according to the Beer-Lambert attenuation law, with an attenuation coefficient of 0.082 mm^{-1} for LYSO, see Table 5.2. The system resolution, measured as FWHM, was evaluated using this spatially varying intrinsic resolution model and compared to the uniform resolution case for a point source simulated in the L-FP system at (10, 0, 0) cm.

Table 5.2: Depth distribution of events across layers 1-6 of the monolithic detector (depth = 16 mm) calculated according to Beer-Lambert attenuation law with an attenuation coefficient of 0.082 mm^{-1} for LYSO.

Layer	1	1	3	4	5	6
Percentage	26.88	21.60	17.36	13.95	11.21	9

5.2.3 Axial noise variability

To evaluate the axial noise variability along the AFOV of the sparse design due to the presence of gaps, a 3-min acquisition of a 20-cm diameter and 120-cm long water cylinder with a uniform ^{18}F activity concentration of 3.7 kBq/ml was simulated. The images were reconstructed with only true coincidences and an isotropic voxel size of 2 mm. Attenuation correction and PSF modeling were implemented in the reconstruction. In the L-FP, only the LORs within the central 60-cm region of the AFOV were considered to enable comparison with the SpM-FP. A 16-cm diameter circular region of interest (ROI) was drawn on each slice, and the noise measure in each slice j was defined as:

$$\mathrm{N_j} = \frac{\mathrm{SD_j}}{C_j} \tag{5.1}$$

where SD_j and C_j are the standard deviation and average of the counts in each ROI, respectively.

5.2.4 Image quality

The NEMA IQ phantom was used to evaluate the image quality of the SpM-FP and L-FP designs. It consists of six hot spheres of various diameters (10, 13, 17, 22, 28, and 37 mm) placed in a body phantom with a warm background and a cold lung insert. The STB activity concentration ratio was 4:1, with a background activity of 5.3 kBq/ml, and a 3-minute acquisition of the phantom was simulated. The true coincidences were reconstructed with attenuation correction and PSF modeling and an isotropic voxel dimension of 2 mm. To evaluate the contrast recovery in the presence of noise in the image, the same ROIs proposed by NEMA were used to compute the contrast-to-noise ratio (CNR) defined as:

$$\mathrm{CNR}_j = \frac{C_{H,j} - C_{B,j}}{SD_{B,j}} \tag{5.2}$$

where $C_{H,j}$ is the average counts in the ROI of sphere j, and $C_{B,j}$ and $SD_{B,j}$ are the average and standard deviation of the counts in the background ROIs, respectively.

IQ body phantom with smaller spheres
A modified IQ phantom with small hot sphere sizes was simulated to probe the limits of the SpM-FP design in distinguishing small features (less than 12 mm in diameter). The overall geometry of the body phantom was kept the same, but the diameters of the hot spheres were reduced to 2, 4, 6, 8, 10 and 12 mm and simulated with a STB activity concentration ratio of 4:1 and 8:1 for a total acquisition time of 3 minutes. The images were reconstructed with an isotropic voxel size of 1 mm, and the CNR was calculated for each sphere for an acquisition time ranging from 30 seconds to 3 minutes.

5.2.5 XCAT anthropomorphic phantom

In this study, a male XCAT phantom (BMI = 18.64) with an activity concentration of 3 MBq/kg was simulated in both configurations, incorporating activity decay to represent imaging one hour after injection. The acquisition was simulated for 30 seconds on the L-FP and 120 seconds on the SpM-FP without further modeling of activity decay, given the relatively short simulation time. Attenuation correction and PSF modeling were implemented in the reconstruction with an isotropic voxel size of 2 mm. Two 3-cm diameter 3D ROIs were placed in the liver and lung, and the normalized standard deviation was calculated for each. These values were plotted as a function of acquisition time for the SpM-FP and compared to the values for a 30-second acquisition with the L-FP.

5.3 Results

5.3.1 Sensitivity

Table 5.3 lists the sensitivity values for the SpM-FP and L-FP configurations for the 70-cm long line source in air and the 106-cm source in air and water. The SpM-FP achieves a NEMA sensitivity of 30 kcps/MBq at the center of the transverse FOV and an average value of 22 kcps/MBq at a 10-cm offset. The average total NEMA sensitivity of the system is then 26 kcps/MBq. This is 4.6 times less than the NEMA sensitivity of the L-FP design, given the reduced AFOV and the presence of gaps.

Table 5.3: Total sensitivity values in kcps/MBq of the SpM-FP and L-FP configurations for the 70-cm line source at the center and at 10-cm radial offset (along X and Y), and the 106-cm line source at the center in air and in a 20-cm water-filled cylinder for attenuation

Source length and position	**Sensitivity (kcps/MBq)**	
	SpM-FP (fixed panels)	**L-FP**
70 cm (centered)	30	140
70 cm (10-cm along X)	21.6	100
70 cm (10-cm along Y)	22.4	101
106 cm (centered)	20	109
106 cm (centered and attenuated)	2.7	13

Figure 5.5a shows the axial sensitivity profiles of both designs for the 70-cm line source. A translation of the panels of half a detector module will smooth out the SpM-FP profile whereby the new detector positions will align with the center of the gaps from the previous position, effectively covering them entirely and compensating for the missing LORs with new ones. The SpM-FP is compared to the L-FP for a 106-cm line source in air and with water attenuation. The latter represents a realistic situation, such as torso scanning with patient attenuation. The sensitivity difference between both designs is less with water attenuation than only air, which can be attributed to the higher attenuation of the oblique LORs in the center of the L-FP design. Figure 5.5b shows the sensitivity profiles of the L-FP and the SpM-FP with panel motion. The panels of the SpM-FP design move vertically relative to the patient to image the head and torso (AFOV of $\sim$ 106 cm). We examine two scanning FOVs: 106 cm and one extended to 136 cm (106 cm plus 15 cm at each end). The profile of the SpM-FP with the 136-cm scanning FOV shows increased sensitivity at the 106 cm AFOV edges, improving count statistics in the brain and pelvic regions.

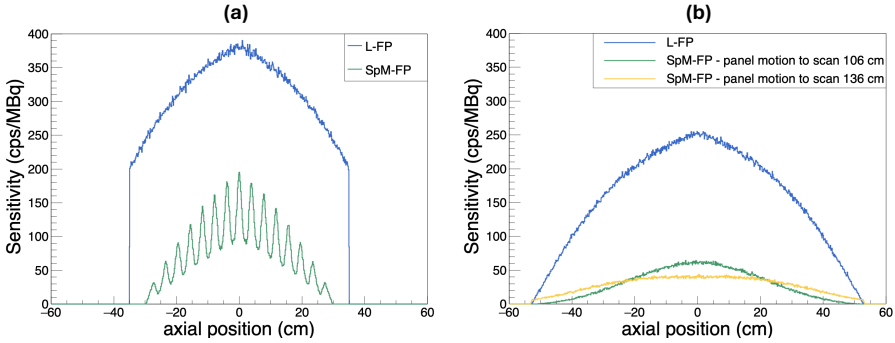

Figure 5.5: Axial sensitivity profiles for (a) the L-FP and SpM-FP with a 70-cm line source, (b) the L-FP and moving SpM-FP to cover two scanning FOVs (106 and 136 cm) with a 106-cm line source.

5.3.2 Spatial resolution

The FWHM in all three directions for both designs with the NEMA point sources are presented in Table 5.4 and graphed in Figure 5.6. The values in the X and Z directions (FWHM-x and FWHM-z) are mostly below 2 mm, varying slightly with radial and axial offset. In the central plane and at three-eighths of the AFOV, the FWHM along Y (FWHM-y) increases when the point source is moved parallel or towards the panels. The SpM-FP design shows resolution values comparable to those of the L-FP in all three directions without significant degradation.

Table 5.5 presents the L-FP system's FWHM for a point source positioned at (10, 0, 0) cm, comparing uniform and spatially varying detector response functions. The data show that the degradation of the 2D and DOI resolutions near the detector edges minimally impacts overall performance. The FWHM values are very similar to those obtained with a uniform response, with a slight improvement in resolution. This is attributed to the better resolution in the central region, which compensates for the lower resolution at the edges, ensuring that the average values at 1.14 mm (2D) and 2.67 mm (DOI) are preserved. Given these findings, the uniform resolution model was adopted for the remainder of this study.

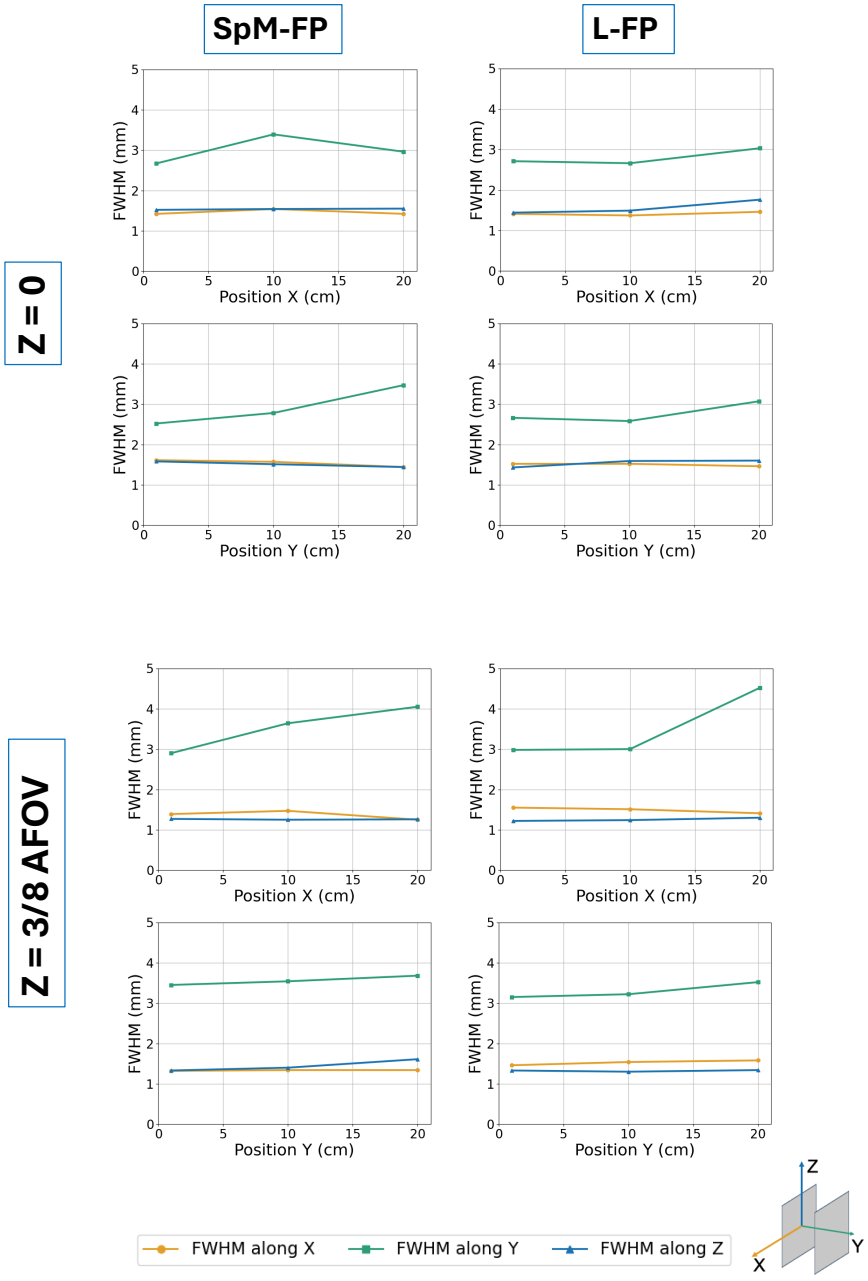

Figure 5.6: FWHM of the NEMA point sources in all three orthogonal directions at different locations moving sideways (X) and towards the panels (Y) at the central axial plane and 3/8ths of the AFOV from the center. The values are shown for iteration 50 at which convergence is observed.

Table 5.4: Spatial resolution FWHM (mm) in all three orthogonal directions for the SpM-FP and L-FP at different X and Y offsets at Z=0 and Z=3/8ths AFOV (22.35 cm and 39.64 cm for the SpM-FP and L-FP, respectively.)
X is the direction parallel to the panels, Y is towards the panels, and Z is the direction of the AFOV.

Source position	**SpM-FP**			**L-FP**		
	X	Y	Z	X	Y	Z
X offset at Z = 0						
1 cm	1.42	2.67	1.52	1.41	2.71	1.44
10 cm	1.54	3.39	1.54	1.37	2.66	1.49
20 cm	1.42	2.96	1.55	1.46	3.03	1.76
Y offset at Z = 0						
1 cm	1.61	2.52	1.58	1.52	2.66	1.43
10 cm	1.57	2.78	1.51	1.52	2.58	1.59
20 cm	1.44	3.47	1.44	1.46	3.07	1.60
X offset at Z = 3/8 AFOV						
1 cm	1.39	2.90	1.27	1.55	2.98	1.22
10 cm	1.47	3.64	1.25	1.51	3.00	1.24
20 cm	1.25	4.05	1.26	1.41	4.52	1.30
Y offset at Z = 3/8 AFOV						
1 cm	1.32	3.45	1.33	1.46	3.15	1.33
10 cm	1.34	3.54	1.40	1.54	3.22	1.30
20 cm	1.34	3.68	1.61	1.58	3.52	1.34

Table 5.5: FWHM values (mm) in all three orthogonal directions for a point source at (10, 0, 0) cm simulated in the L-FP design using two detector response models: one with a uniform 2D resolution of 1.14 mm and DOI resolution of 2.67 mm and another with a spatially varying 2D resolution ranging from 1.02 to 1.35 mm and DOI resolution between 2.4 and 3.7 mm.

Detector response function	**FWHM-x**	**FWHM-y**	**FWHM-z**
Uniform	1.37	2.66	1.49
Spatially varying	1.34	2.48	1.43

5.3.3 Axial noise variability

Figure 5.7a shows the central coronal slice of the reconstructed image of each design. The slice of the L-FP appears to be more uniform, while that of the SpM-FP exhibits a non-uniform and higher noise that follows the pattern of the gaps. The normalized standard deviation (SD) was calculated for each slice along the AFOV and plotted as a function of the axial distance from the center, as shown in Figure 5.7b. The SpM-FP's axial noise variability is lowest in the central 40-cm region of the AFOV. It increases closer to the edges, where the peaks get bigger with increasing distance from the center.

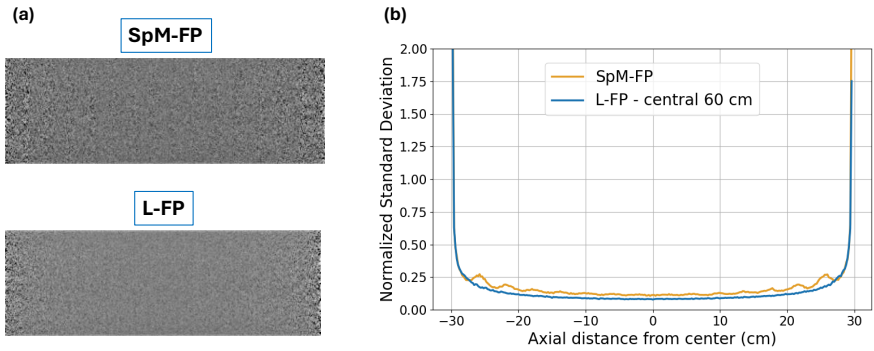

Figure 5.7: (a) Central coronal slices through the reconstructed images (5th iteration) of a 3-minute simulation of a 20-cm diameter long cylinder on the SpM-FP (top) and L-FP (bottom) designs with an AFOV of 60 cm. (b) Axial noise profile of a long, 20-cm diameter water cylinder simulated in the SpM-FP and the central 60-cm AFOV of the L-FP.

5.3.4 Image quality

Figure 5.8 shows the central transverse slices of the reconstructed IQ images (10th iteration - STB activity concentration ratio 4:1) for the L-FP and the SpM-FP with and without panel motion using different acquisition times. Elongation resulting from the limited range of projection angles is visible in the upper and lower regions of the transverse slices. With a TOF value of 300 ps and an acquisition time as low as 30 seconds, all the spheres are still visible for both designs. Since the IQ phantom has an axial extent of around 21 cm only, the SpM-FP with moving panels to cover a scanning FOV of 106 cm obviously has less

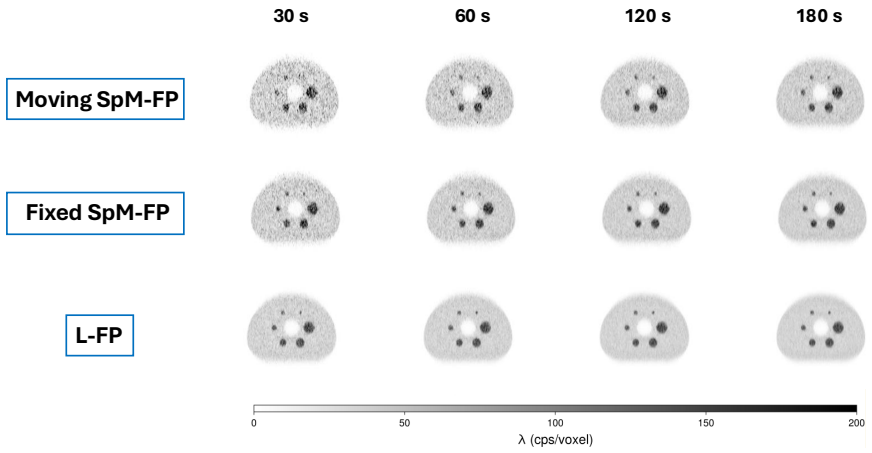

Figure 5.8: Transverse slices of the reconstructed IQ images (10th iteration) for the SpM-FP with moving panels, SpM-FP with fixed panels and the L-FP at 30, 60, 120 and 180-s acquisitions, with a STB activity concentration ratio of 4:1 and a voxel size of 2 mm.

count statistics than the design with fixed panels. This can be addressed by scanning for longer when panel motion is needed. The image of the IQ phantom simulated in the L-FP design shows a very good image already at 30 seconds.

To evaluate the contrast in the presence of noise for the SpM-FP design with respect to the L-FP, the CNR is calculated for the images reconstructed from data simulated without panel motion. Figure 5.9 compares the CNR values across iterations for all spheres at various acquisition times in the SpM-FP with those from a 30-second acquisition of the L-FP. The peak CNR is attained at the second iteration for all spheres and is higher than 5 for even the smallest sphere using a 30-s acquisition, which means that according to the Rose criterion [130], all spheres are observable. The CNR of the SpM-FP increases with increasing acquisition times, achieving at 120 seconds values similar to those of the L-FP at 30 seconds for the large spheres and higher values for the smaller spheres. Figure 5.10 shows the reconstructed images of the modified IQ phantom with smaller spheres for the STB activity ratios of 4:1 and 8:1 at different acquisition times. Qualitatively, the smallest observable sphere has a diameter of 4 mm for a ratio of 8:1 and 6 mm for a ratio of 4:1 at longer acquisition times. To evaluate the

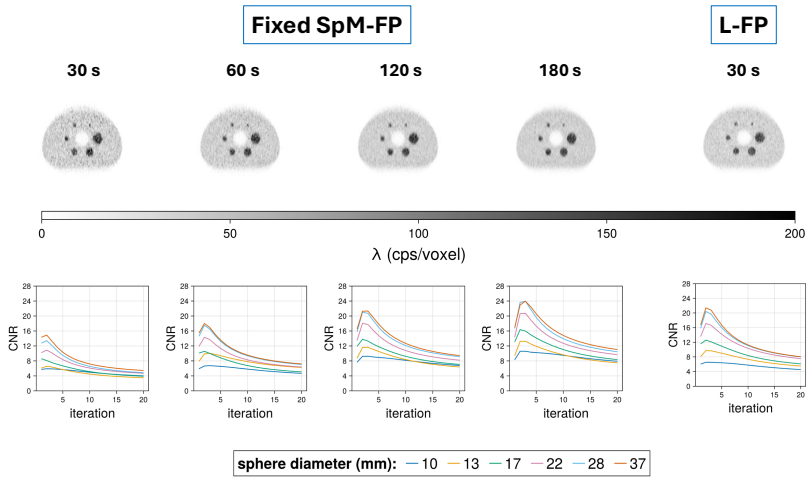

Figure 5.9: Transverse slices of the reconstructed IQ images (3rd iteration) and the CNR values as a function of the iteration number for various sphere diameters (4:1 activity concentration ratio) for the SpM-FP with fixed panels at different acquisition times compared to the L-FP at 30 s (with PSF modeling).

observability quantitatively, the maximum value of the CNR is plotted as a function of acquisition time for the different sphere sizes, as shown in Figure 5.11. The black dashed line at a CNR value of 5 marks the threshold of observability based on the Rose criterion.

5.3.5 XCAT anthropomorphic phantoms

Figure 5.12 shows the central coronal, sagittal and transverse slices of the reconstructed XCAT images for the SpM-FP at varying acquisition times compared to the L-FP image at 30 seconds. The SpM-FP design includes panel motion to cover a scanning FOV of 136 cm to increase the count statistics in the leg and brain regions. Even at 30 seconds, with almost five times lower sensitivity than the L-FP, the reconstructed image of the SpM-FP demonstrates good quality with reasonable organ contrast and acceptable noise level. As the acquisition time increases, image noise decreases, resulting in improved image quality that resembles the L-FP image at 30 seconds. In the sagittal and transverse views, elongation artifacts can be observed due to the limited angular range of the data.

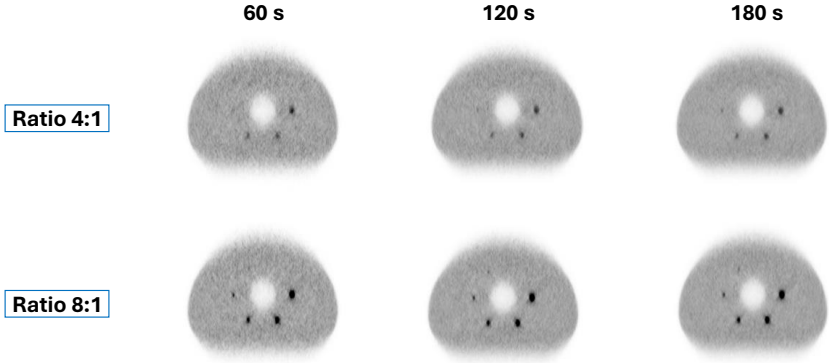

Figure 5.10: Transverse slices of the reconstructed IQ phantom with smaller spheres (3rd iteration) for the SpM-FP (fixed panels) at 60, 120 and 180-s acquisitions, with activity concentration ratios of 4:1 and 8:1 and a voxel size of 1 mm.

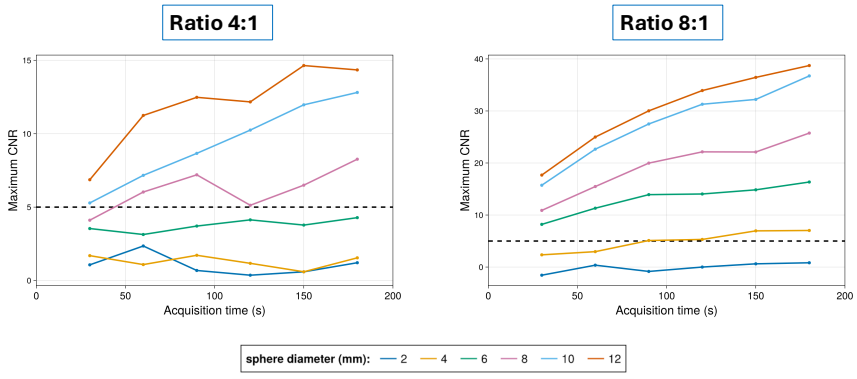

Figure 5.11: Maximum CNR values over iterations as a function of acquisition time for the SpM-FP at activity ratios 4:1 and 8:1, with the black dashed line representing the observability threshold according to the Rose criterion.

The extent of the artifacts and impact on the image quality is however limited and comparable between both configurations.

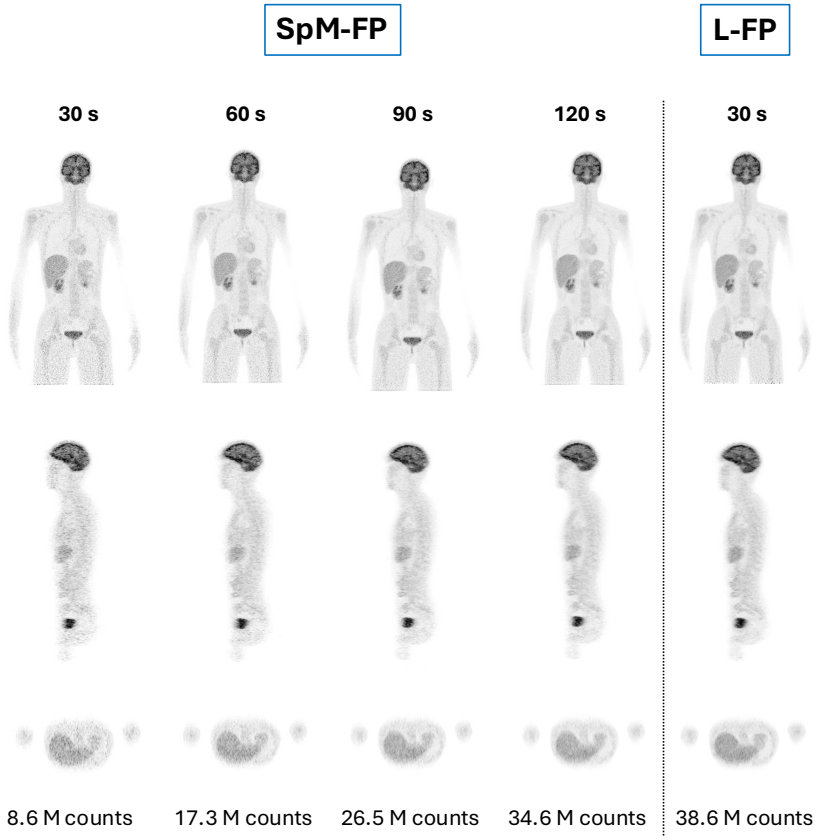

Figure 5.12: Central coronal, sagittal and transverse slices of the reconstructed XCAT phantom for the SpM-FP at acquisition times of 30, 60, 90 and 120 s and for the L-FP at 30 s. The number of detected counts used in the reconstruction is displayed for each case.

Figure 5.13 displays the 3D ROIs positioned in the liver and lung of the XCAT image. The SD within each ROI decreases as the acquisition time increases, approaching at 120 s the SD value of the ROI in the L-FP image at 30 s. The SD in the lung ROI is consistently higher than in the liver due to differences in tissue density and tracer uptake.

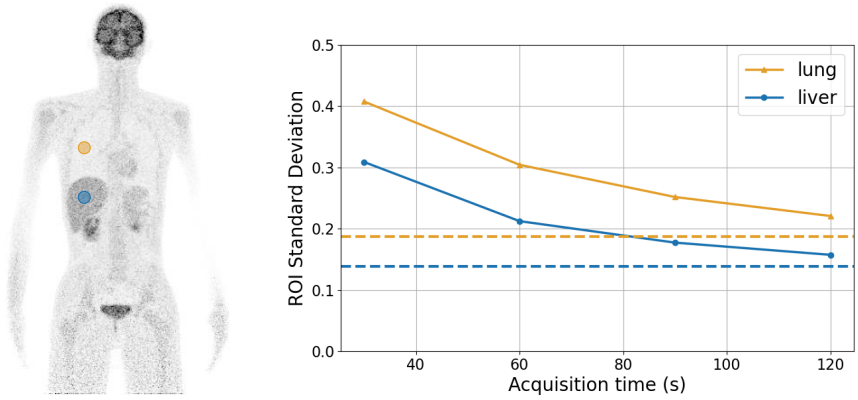

Figure 5.13: Central coronal slice of the XCAT phantom for the SpM-FP with ROIs indicated (left) and a graph of the standard deviation within the ROIs as a function of acquisition time (right). Dashed lines represent the SD values for the L-FP at 30 s.

5.4 Discussion

For both designs, the NEMA sensitivity for a 70-cm line source drops significantly at a 10-cm offset due to the limited angle coverage in the flat-panel geometry, represented schematically in Figure 5.14. With a 106-cm line source, the L-FP is 5.5 times more sensitive than the SpM-FP configuration without panel motion, owing to its longer axial extent and compact design. This sensitivity difference decreases to a ratio of 4.8 when the source is surrounded by a water phantom, primarily due to the attenuation of LORs at large oblique angles [23]. Table 5.6 shows that the SpM-FP, with 22% less detector surface and 38% less scintillator volume than the Biograph Vision 600 (26 cm AFOV), achieves 59% higher sensitivity than that of the simulated Vision 600. Moreover, the SpM-FP's AFOV is 2-3 times greater than that of current SAFOV systems, including the Vision 600. The extended coverage enables the simultaneous imaging of the full torso or the brain and upper torso in a single scan. With limited panel movement, it also allows scanning of both the brain and full torso in a relatively short time, offering a distinct advantage over the Vision 600. From a cost perspective, based on a previous study conducted by our group detailing the PET component cost of the WT-PET and standard AFOV PET systems [3], the L-FP design is only 1.9 times more expensive than the Vision 600 (excluding the CT

Table 5.6: Comparison of the NEMA sensitivity and geometrical characteristics between the SpM-FP configuration and the Biograph Vision 600 (recent standard AFOV scanner).

	SpM-FP	**Biograph Vision 600**
Average NEMA sensitivity (kcps/MBq)	26	16.4
Axial length (cm)	59.6	25.6
Crystal thickness (mm)	16 (LYSO)	20 (LSO)
Detector surface ($\times 10^6 mm^2$)	0.48	0.62
Scintillator volume ($\times 10^6 mm^3$)	7.68 s	12.45

component). Meanwhile, the SpM-FP, with 2.5 times fewer detectors, is 2.5 times less expensive than the L-FP. This means that the SpM-FP cost would be approximately 30% lower than the PET component of the Vision 600.

Given that they have the same axial extent, Table 5.7 compares the geometrical characteristics of the L-FP and the Biograph Vision Quadra. With less than half detector surface and volume, the L-FP achieves 68% of the sensitivity of the Quadra at half the cost according to Vandenberghe et al. [3]. That said, sensitivity and cost alone do not fully capture PET system performance; a comprehensive evaluation must also account for additional metrics to draw accurate conclusions. It should also be noted that the current flat-panel configuration with a gap of 50 cm may not be suitable for bed-ridden patients. However, the design is intended as a complementary system within nuclear medicine departments rather than a full replacement. In this role, it could improve workflow flexibility, especially since bed-ridden cases represent only a small fraction of the PET imaging cohort.

Table 5.7: Comparison of the NEMA sensitivity and geometrical characteristics between the L-FP configuration and the Biograph Vision Quadra (recent long AFOV scanner).

	L-FP	**Biograph Vision Quadra**
Average NEMA sensitivity (kcps/MBq)	120	176
Axial length (cm)	106	106
Crystal thickness (mm)	16 (LYSO)	20 (LSO)
Detector surface ($\times 10^6 mm^2$)	1.2	2.48
Scintillator volume ($\times 10^6 mm^3$)	19.2	49.8

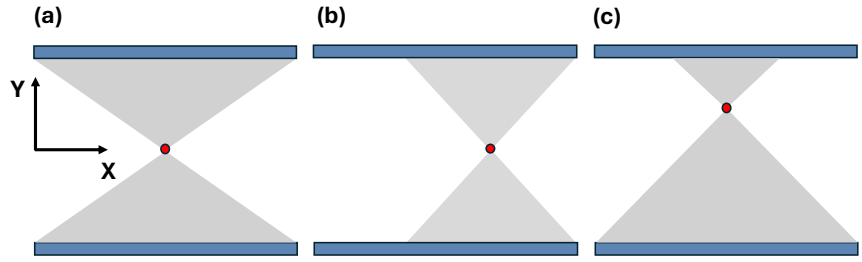

Figure 5.14: Schematic view of the available projection ranges in the L-FP and SpM-FP for a transverse view of the sensitivity line source (a) in the center, (b) moved 10 cm parallel to the panels (in the X direction), (c) moved 10 cm towards one of the panels (in the Y direction). The same also applies to a point source.

The spatial resolution of PET systems primarily depends on the intrinsic resolution of the detectors, as well as fundamental limitations such as positron range and non-collinearity. Therefore, improving the system resolution relies on enhancing the intrinsic detector resolution [131]. Monolithic detectors were chosen for their superior intrinsic resolution and DOI capabilities. The aim is to bring the detector resolution down to the fundamental physical limit. Based on prior measurements [55], the 50 x 50 x 16 mm^3 LYSO detectors used in this study have an intrinsic resolution of 1.14 mm, contributing to the system's resolution in X and Z directions, parallel to the panels (sideways and vertically, respectively). Additionally, the detectors have a DOI resolution of 2.67 mm, which, together with elongation artifacts caused by limited angular coverage, degrades the system resolution along the Y direction (perpendicular to the panels). This explains why both configurations consistently show higher FWHM-y values than FWHM-x and FWHM-z across the entire FOV. The results shown in Table 5.4 and Figure 5.6 demonstrate a relatively uniform spatial resolution of less than 2 mm in the two directions parallel to the panels across the FOV. This is owing to the DOI information provided by the monolithic detector and their superior intrinsic resolution. Such system-level spatial resolution has not been achieved experimentally, nor has it been reported by any simulated and validated model of the current leading standard-AFOV or long-AFOV scanners [66], [132]. At Z=0, the FWHM-y is generally less than 3 mm in the center and increases when the point source is moved parallel or

towards the panels due to the reduced range of angles in the transverse planes, as shown in Figure 5.14 (for a point source). As the source is moved toward the edge of the AFOV (at 3/8ths of the AFOV), the range of available projection angles is reduced by factors of 3 and 2.3 for the SpM-FP and L-FP, respectively. See Figure 5.15. Consequently, fewer oblique LORs contribute information along the Y-direction and for both designs, the measured FWHM-y near the edge of the AFOV is consistently greater than at the center. In contrast, while the FWHM-x and FWHM-z values may vary slightly, they do not exhibit significant degradation, as they are determined by the LORs that are perpendicular to the detector panels and are unaffected by an axial displacement of the source. Overall, the SpM-FP design does not exhibit significant degradation in FWHM values due to detector gaps or reduced AFOV when compared to the L-FP design.

Additionally, we performed an analytical calculation of the expected system spatial resolution by accounting for the combined contributions of positron range, non-collinearity, and intrinsic detector resolution using the following equation:

$$R_{\text{sys}} \approx \sqrt{R_{\text{det}}^2 + R_{\text{range}}^2 + R_{\text{acol}}^2} \tag{5.3}$$

where $R_{\text{det}} \approx \frac{R_{\text{int}}}{\sqrt{2}}$ when the point source is positioned at the center of the transverse FOV, i.e., halfway between detectors and $R_{\text{det}} \approx R_{\text{int}}$ when it is located closer to one of the panels, i.e. near the detector's face. Since our system is not ring-based, for the non-collinearity contribution, the equation $R_{\text{acol}} = 0.0022D$ where D is the system diameter is calculated for two cases:

- **case A**: $D = 50$ *cm*, which represents the direct gap between the two panels.
- **case B**: $D = 87$ *cm*, representing an extreme case to account for the most oblique LORs in the transverse plane.

The system resolution values are shown for both cases in Table 5.8 for a point source in the center of the transverse FOV and Table 5.9 for a point source near the detector's surface. For both tables, the positron range contribution is taken as $R_{\text{range}} = 0.5$ mm.
The calculated values highlighted in gray in the above tables generally align with the measured values reported in Table 5.4.

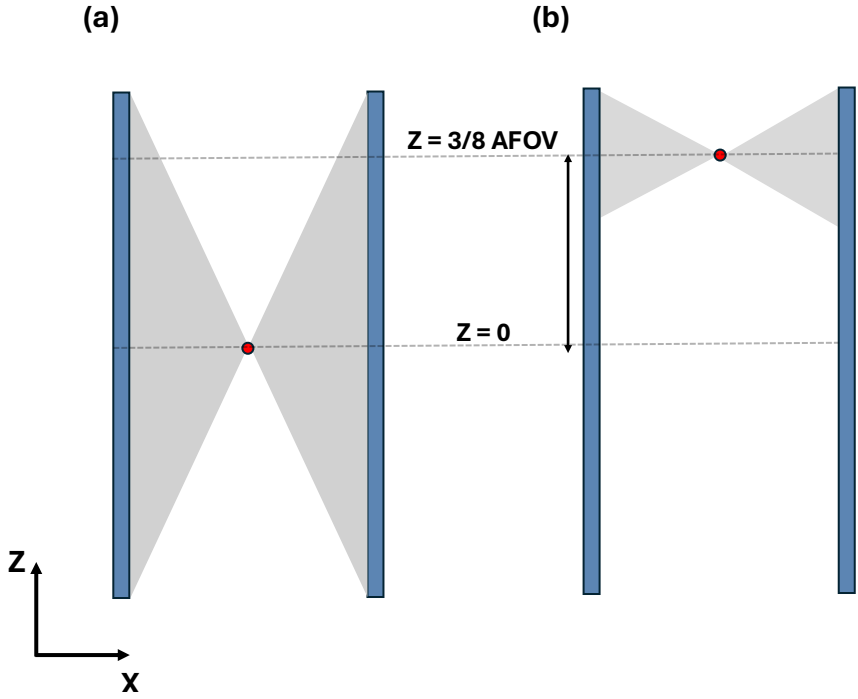

Figure 5.15: Schematic view of the available axial projection ranges in the L-FP for (a) a point source in the center of the AFOV and (b) a point source at 3/8ths of the AFOV.

Table 5.8: System resolution for cases A and B for a point source in the center of the transverse FOV, i.e. halfway between detectors. All values are in mm.

	$R_{\mathbf{int}}$	$R_{\mathbf{det}}$	$R_{\mathbf{acol}}(\mathbf{A})$	$R_{\mathbf{acol}}(\mathbf{B})$	$R_{\mathbf{sys}}(\mathbf{A})$	$R_{\mathbf{sys}}(\mathbf{B})$
2D (X & Z)	1.14	0.81	1.10	1.91	1.45	2.29
DOI direction (Y)	2.67	1.89	1.10	1.91	2.24	3.33

Table 5.9: System resolution for cases A and B for a point source near the detector's surface. All values are in mm.

	$R_{\mathbf{int}}$	$R_{\mathbf{det}}$	$R_{\mathbf{acol}}(\mathbf{A})$	$R_{\mathbf{acol}}(\mathbf{B})$	$R_{\mathbf{sys}}(\mathbf{A})$	$R_{\mathbf{sys}}(\mathbf{B})$
2D (X & Z)	1.14	1.14	1.10	1.91	1.66	2.56
DOI direction (Y)	2.67	2.67	1.10	1.91	2.93	4.27

The presence of axial gaps in the SpM-FP design leads to variations in the axial sensitivity and noise profiles as shown in Figures 5.5a and 5.7b, respectively. However, these variations are not prominently visible in the reconstructed image of the cylinder, particularly when compared to the image obtained with the L-FP configuration. The normalized standard deviation shows minimal variation within the central 40 cm of the AFOV. This is attributed to the moderate size of the axial gaps (28 mm), which are approximately half the width of a detector module (50 mm). Simulations by the PennPET group at the University of Pennsylvania on various scanner configurations with different gap sizes concluded that gaps should not exceed half the width of a detector ring to prevent significant performance variability [71]. Our findings align with this conclusion.

The IQ and XCAT results indicate that a 30-second scan in the SpM-FP configuration with moving panels is insufficient to generate a high-quality image. The reduced AFOV, axial gaps, and panel motion require longer scan times to increase count statistics and reduce image noise. A 120-second scan in the SpM-FP achieves CNR values in the IQ phantom and SD values in the XCAT liver and lung comparable to those of the L-FP in 30 seconds, consistent with the 4.8-fold higher sensitivity compared to the SpM-FP.
On another note, in both designs, the reconstructed transverse slices of the IQ phantom exhibit elongation artifacts in the direction of the panels caused by the missing projection angles. These artifacts appear as shape distortions in the larger spheres and as smearing at the phantom's upper and lower edges, where boundaries are poorly delineated and activity spills into non-active regions. Similarly, the transverse and sagittal slices of the XCAT also show blurring along edges perpendicular to the panels. Table 5.10 summarizes the projection angle ranges in both designs for the transverse and axial planes derived from the corresponding acceptance angles. For comparison, values are also shown for the Biograph Vision 600 and Quadra. In the transverse plane, the flat-panel designs cover only 61% of the projection range available to a cylindrical configuration. However, in the axial direction, the SpM-FP provides a wider projection range than the Vision 600, and the L-FP a wider range than the Quadra. This provides additional information that partly mitigates the impact of missing transverse projection angles, though the artifacts remain. Consequently, the residual artifacts reduce PET image quality, and correction strategies will be required before the proposed flat-panel

designs can be considered clinically viable.

Table 5.10: Available projection ranges at the center of the FOV of the SpM-FP and the L-FP in comparison to the Biograph Vision 600 and Quadra.

	SpM-FP	**Vision 600**	**L-FP**	**Quadra**
Transverse	110°	180°	110°	180°
Axial	100°	36°	130°	105°

5.5 Conclusion

The study presented in this chapter demonstrates that the L-FP LYSO-based configuration combines cost-effectiveness and higher throughput with superior spatial resolution and good overall image quality in just 30-second acquisition. With 2.5 times less detectors and an axial extent exceeding half that of the L-FP, the SpM-FP emerges as an attractive and more cost-efficient clinical alternative. The sensitivity, image quality and XCAT results indicate that a 2-3-minute scan with SpM-FP produces images comparable in quality to a 30-second scan on the L-FP. The axial noise profile shows low variability, suggesting that the presence of gaps has little impact on the image quality beyond the expected drop in sensitivity which can be compensated for by slightly longer scan times. Moreover, the superior spatial resolution shows great promise, particularly for detecting sub-centimeter lesions. To fully assess these benefits, further studies will compare the superior resolution SpM-FP against the Biograph Vision 600, which provides better TOF resolution and complete angular coverage in the transverse plane. This comparison will be presented in Chapter 6. Looking ahead, strategies to address limited-angle artifacts using deep learning methods will be explored in Chapter 7.

Chapter 6

PET performance trade-offs

6.1 Introduction

Despite advances in PET image quantification with long-AFOV systems that improve diagnostic accuracy, treatment planning and therapy monitoring, diagnosis and follow-up in most clinics continue to rely on visual examination of images. A common challenge remains the reliable detection of small lesions [133], [134], and precise tumor outlining [135], [136], both of which are limited by current spatial resolution and its effect on lesion contrast. This challenge is particularly critical for early-stage lesions, where small size and low tracer uptake push the scanner's detection limits. In such cases, detectability depends on system sensitivity, resolution and the choice of reconstruction algorithms and parameters, which collectively determine the effective signal-to-noise ratio (SNR) of the final image.

As explained in section 2.3.2, the signal-to-noise ratio (SNR) of a PET image depends on the number of detected counts, roughly scaling with the square root of the counts. Therefore, doubling the SNR requires increasing the number of detected events by about a factor of four. Consistent with this principle, Yan et al. demonstrated that increasing the number of counts in clinical PET/MR scans results in higher liver SNR^2 and lesion CNR, along with decreased bias and noise [137]. Extending the AFOV is a way to boost detected counts, but it requires more detectors and increases system costs. Increasing the administered activity is another option, but it raises patient risk and causes more random coincidences, adding noise to the background. Extending the scan time is also undesirable given the clinical focus on reducing

acquisition time. Additionally, as discussed in Chapter 2, time-of-flight (TOF) information can significantly improve SNR. Specifically, the gain from non-TOF to TOF is proportional to $\sqrt{\frac{D}{\Delta x}}$, where D is the object size, and Δx is the spatial uncertainty determined by how accurately the difference in arrival times of the two photons is measured. Better TOF resolution directly enhances SNR. However, this benefit is limited by current detector technology and the achievable timing resolution in the system.

From a different perspective, early studies have demonstrated that spatial resolution can address the challenge of low SNR caused by low statistics. Muehllehner [138] demonstrated that improved spatial resolution can compensate for lower count statistics. Specifically, increasing system resolution by 2 mm resulted in image quality similar to what is achieved with roughly four times more counts at lower resolution. This indicates that higher resolution can reduce the injected dose and, consequently, patient exposure while also decreasing noise from random coincidences, since fewer counts are needed overall. A recent work by Nuyts et al. showed that improvements in spatial resolution lead to an increase in "effective" sensitivity, an overall measure that accounts for detector solid angle coverage, stopping power, TOF resolution, scatter fraction and system spatial resolution [139]. Additionally, Kaufman et al. pointed out that spatial resolution is an inherent property of the imaging system, independent of image statistics [140]. Importantly, they also showed that spatial resolution directly impacts image contrast and the ability to distinguish small features, thereby enhancing the benefits of increased sensitivity and statistical data. These findings are particularly relevant to our work, as the cylindrical and flat-panel PET systems previously proposed are based on monolithic detectors, which inherently provide superior intrinsic resolution and depth-of-interaction capabilities.

In this chapter, we therefore test the limits of detection of the most cost-effective among the previously proposed designs, the sparse medium flat panels (SpM-FP) and examine how the improved spatial resolution can enhance image SNR and lesion contrast for a given number of detected counts. Specifically, we assess whether higher resolution can compensate for reduced statistics while preserving diagnostic quality. This analysis offers insights into the trade-offs between resolution, sensitivity, and acquisition conditions in developing next-generation PET systems.

6.2 Materials and methods

In the NEMA IQ phantom, the smallest sphere has a diameter of 10 mm, which is too large to test the detection limits of the SpM-FP design. Therefore, for this study, we use the IQ body phantom with smaller spheres described in Chapter 5, and we refer to it here as the high-resolution torso phantom, see Figure 6.1. It is simulated in the static SpM-FP with sphere-to-background (STB) activity concentration ratios of 4:1 and 8:1 for an acquisition of six minutes. The images were reconstructed using only true coincident events with a TOF of 300 ps and an isotropic voxel size of 0.5 mm, given how small the imaged spheres are. This is also supported by a previous study that showed the advantage of using smaller voxel sizes to improve tumor detection performance for PET [141]. The contrast recovery coefficients (CRCs) and contrast-to-noise ratios (CNRs) were then calculated for the different scenarios.

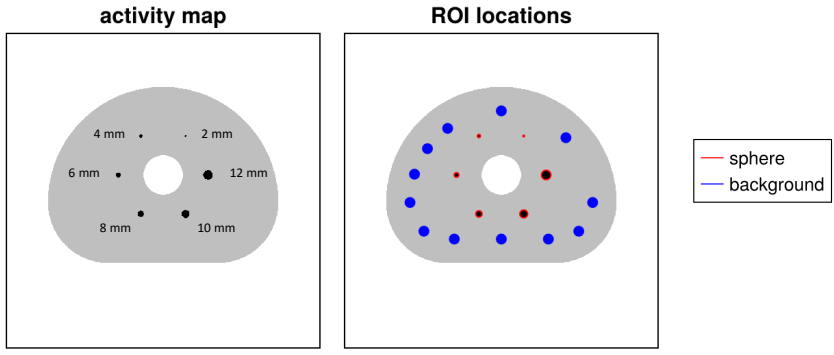

Figure 6.1: Schematic of the central transverse slice of the high-resolution torso phantom showing the reduced dimensions of the hot spheres in red and the background regions of interest in blue.

Detection limits of the SpM-FP

Initially, the detection limits of the SpM-FP were evaluated by varying the acquisition time to determine which of the three smallest spheres (2, 4, and 6 mm) could be reliably detected. Reconstructions were performed at 2-minute intervals, up to 6 minutes, since changes were minor when using an increment of 1 minute. In this study, the actual intrinsic and DOI resolutions of the monolithic LYSO detectors were used. For PSF

modeling, the system's spatial resolution values at the scanner's center were applied, since the phantom was positioned in the center.

Detector resolution versus counts
In this study, the impact of detector spatial resolution was evaluated by varying the detector blurring parameters to determine the smallest sphere that can be reliably detected for a given number of counts and to assess how this detection limit changes with improved resolution. The endpoints of the lines of responses (LORs) were blurred using a kernel size corresponding to the intrinsic detector and DOI resolutions as described in the previous chapters. Three additional cases were considered, where the actual detector and DOI resolution values were scaled by factors of 2, 3, and 4. To enable accurate point spread function (PSF) modeling, the effective spatial resolution of the SpM-FP in the center of the FOV was first evaluated for each detector resolution scenario. These values were then used as the corresponding PSF kernels during image reconstruction.

Comparison with the simulated Vision600
To compare the resolution limits of the SpM-FP with those of the Siemens Biograph Vision 600, we simulated the high-resolution body phantom using the validated MC model of the Vision 600. The model had previously been benchmarked against the scanner's sensitivity, showing good agreement with both the simulated values reported in Chapters 4 and 5, and the measurements by van Sluis et al. [118]. The STB activity concentration ratios were set to 4:1, with acquisition time of 6 minutes. To account for the intrinsic resolution limitations of the Vision 600 pixelated detectors which lack DOI capability, the interaction points within each detector pixel recorded in GATE were shifted to the central plane of the pixel and uniformly randomized within that plane. The reported TOF resolution of 214 ps was incorporated to reflect the system's timing performance. In addition, PSF modeling was applied using a kernel size of (4.4, 4.0, 4.5) mm, corresponding to the reported spatial resolution of the Vision 600 at the scanner's center, where the high-resolution torso phantom was positioned.

6.3 Results

6.3.1 Detection limits of the SpM-FP

Figure 6.2 shows the reconstructed images and the contrast metrics of the high-resolution torso phantom (10th iteration) at an STB activity

ratio of 4:1 for various acquisition times. The CRC values stay consistent across different acquisition times while the CNR values increase for most spheres due to reduced image noise at higher statistics. The 2-mm and 4-mm spheres do not meet the Rose criterion, with CNR values remaining well below 5 even after six minutes of acquisition. In contrast, the 6-mm sphere reaches a CNR of 5 with increasing statistics after approximately 15 iterations, demonstrating that the SpM-FP can reliably detect lesions as small as 6 mm in diameter with a relatively low uptake given sufficient acquisition time. Looking at the 10th iteration at 360 seconds, the 6-mm sphere is already visible despite having a CNR less than 5. This can be due to the relatively uniform background of the phantom used, however, in clinical patient data, with increased anatomical complexity and heterogeneity, the Rose criterion serves as a more strict threshold for reliable lesion detection. The same analysis was performed for an STB activity concentration ratio of 8:1 with results shown in Figure 6.3. At this higher contrast, the resolution limit improves and the SpM-FP can detect the 4-mm sphere as early as 120 s, where the CNR slightly exceeds 5 at the 10th iteration and the sphere is clearly visible in the reconstructed images. At longer acquisition times, the CNR of all spheres except the 2-mm increases further as image noise decreases. CRC values remain consistent as image noise decreases confirming that the improvement in CNR mainly results from reduced noise at higher statistics.

6.3.2 Detector resolution versus counts

Having established the detection limits of the SpM-FP for STB activity concentration ratios of 4:1 and 8:1, we now examine the effect of degrading detector resolution and consequently system spatial resolution on image quality with a focus on CNR values of the smallest spheres. The analysis is performed at an STB ratio of 8:1, at which the 4-mm is detectable in the SpM-FP. Table 6.1 summarizes the actual detector resolution along with values scaled by factors of 2, 3, and 4. For each case, the corresponding PSF kernel size was determined based on the system's achievable spatial resolution in all three direction.

Figure 6.4, shows the reconstructed images and the associated CRC and CNR values for these four scenarios. As detector resolution degrades, the broader PSF kernels applied during reconstruction lead to smoother and less sharp images. While this smoothing reduces image noise and results in higher CNR values overall, the contrast recovery is not improved. The CRC is consistently highest at the best detector resolution, and

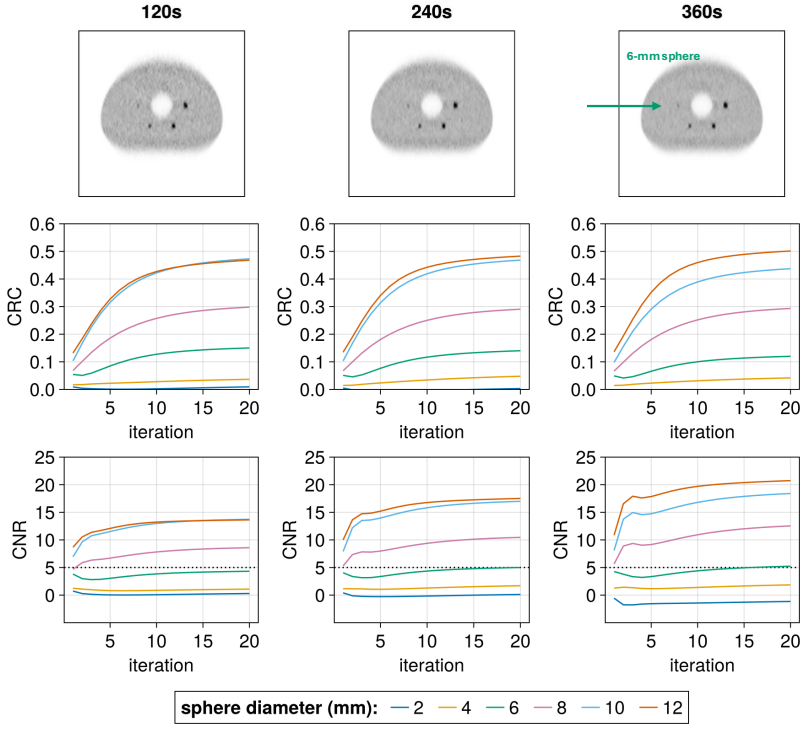

Figure 6.2: Reconstructions of the high-resolution torso phantom (10th iteration) simulated in the SpM-FP, with the corresponding CRC and CNR at **different acquisition times** for an STB activity concentration ratio of **4:1** with PSF modeling applied. The dotted black line represents the observability threshold according to the Rose criterion.

Table 6.1: Detector resolution and DOI values in mm scaled by factors of 2, 3, and 4 with the corresponding kernels used for PSF modeling.

	DRx1	**DRx2**	**DRx3**	**DRx4**
2D resolution - DOI	1.14 - 2.67	2.28 - 5.34	3.42 - 8.01	4.56 - 10.68
PSF kernel	(1.5,2.8,1.5)	(2,4,2)	(2.8,5.5,2.8)	(3.4,6.5,3.4)

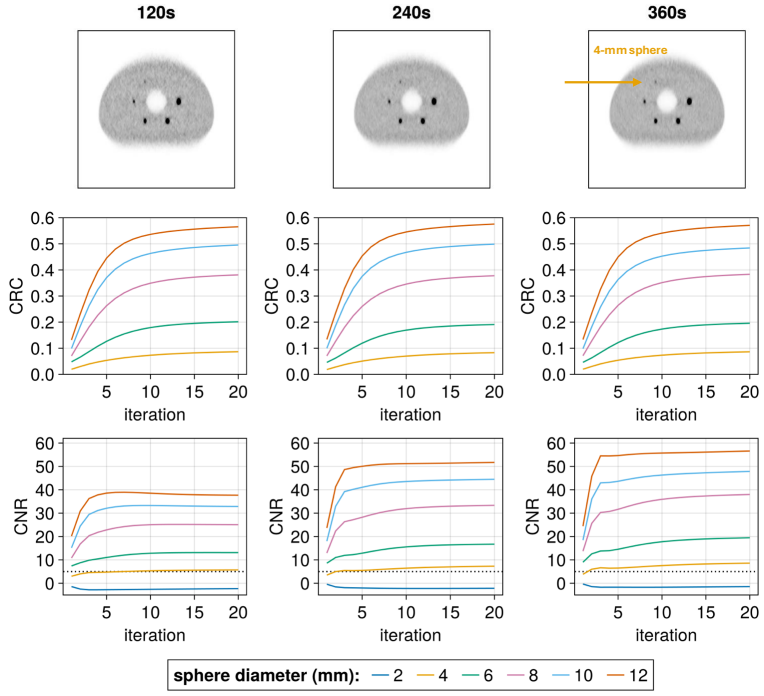

Figure 6.3: Reconstructions of the high-resolution torso phantom (10th iteration) with the corresponding CRC and CNR at **different acquisition times** for an STB activity concentration ratio of **8:1** with PSF modeling applied. The dotted black line represents the observability threshold according to the Rose criterion.

importantly, the CNR of the 4-mm sphere falls below the detectability threshold (CNR less than 5) when detector resolution is degraded by factors of 3 and 4, rendering the sphere practically undetectable. To put this into perspective and evaluate the trade-off between detector resolution and the number of counts or simply acquisition time, Figure 6.5 compares three cases:

- 180-second acquisition with a detector resolution degraded by a factor of four (DRx4),
- 360-second acquisition with the same degraded resolution (DRx4) to increase the number of counts, and

- 180-second acquisition with the actual detector resolution (DRx1).

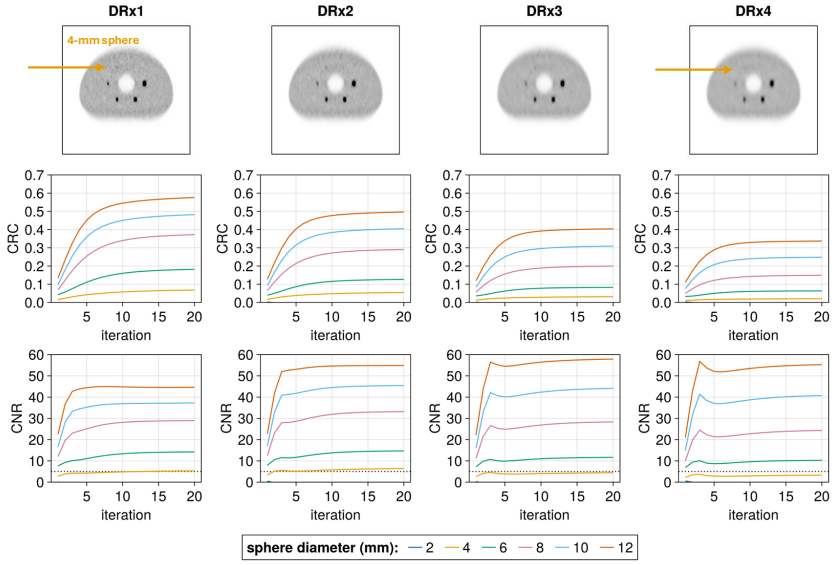

Figure 6.4: Reconstructions of the high-resolution torso phantom (10th iteration) with the corresponding CRC and CNR at **varying detector resolutions** with an acquisition time of 180 s and an STB activity concentration ratio of **8:1** with PSF modeling applied (bigger PSF kernels are used for higher detector resolution values).

The DRx4 reconstructions (left and middle) appear smoother and increasingly blurred due to the broader PSF kernels, whereas the DRx1 reconstruction (right) is sharper and achieves higher CRC values despite showing slightly more noise. As expected, doubling the statistics at DRx4 increases the CNR of the 4-mm sphere above 5, enabling detection. However, with DRx1, the same sphere is already visible at 180 seconds, reaching a CNR of roughly 5 by the 10th iteration. This result highlights that improving detector resolution provides a more effective way for detecting small lesions than increasing acquisition time. Enhanced resolution not only improves detectability but also strengthens contrast recovery, a benefit that cannot be achieved by only increasing statistics.

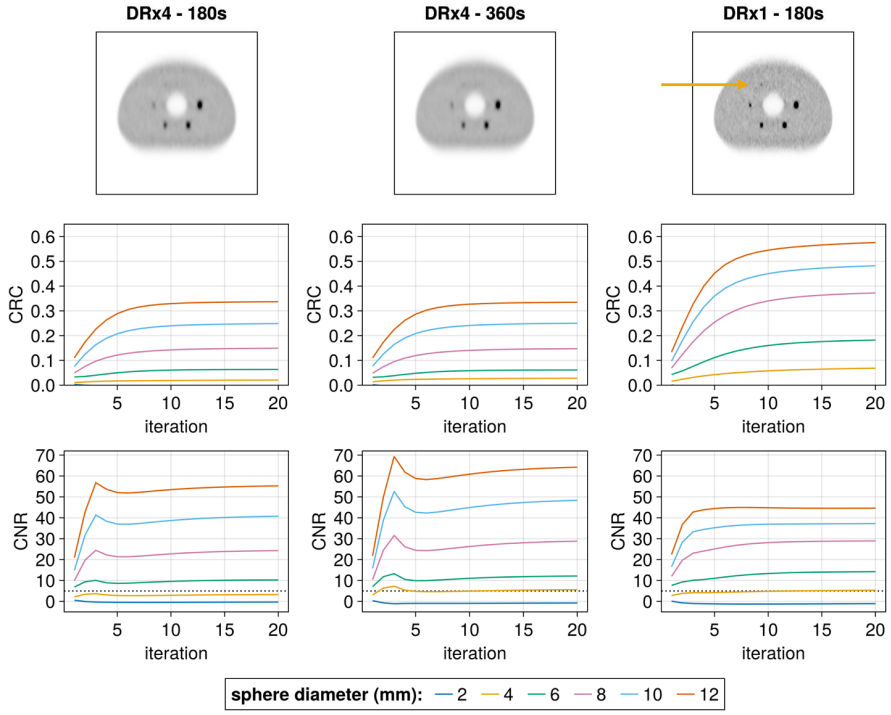

Figure 6.5: Reconstructions of the high-resolution torso phantom (10th iteration)simulated in the SpM-FP, with the corresponding CRC and CNR at **180 and 360 seconds for DRx4** and at **180 seconds for DRx1** for an STB activity concentration ratio of **8:1** with PSF modeling applied (bigger PSF kernels are used for the cases of DRx2 and DRx4).

6.3.3 Comparison with the simulated Vision 600

Figure 6.6 compares the reconstructed images of the SpM-FP and Vision 600 for a 360-s acquisition with an STB ratio of 4:1. The Vision 600 image appears smoother, with well-defined edges, whereas the SpM-FP reconstruction is affected by elongation artifacts, particularly at the top and bottom edges of the IQ phantom and around the larger spheres. Despite this, the SpM-FP achieves higher CRC values than the Vision 600, reflecting its superior spatial resolution. In contrast, the CNR values are lower for the SpM-FP due to increased background noise. For the 6-mm sphere, the SpM-FP reaches a CNR of about 5 after the 10th iteration, whereas the Vision 600 achieves nearly twice this value,

despite the sphere being only faintly discernible in both reconstructions as indicated by the green arrow.

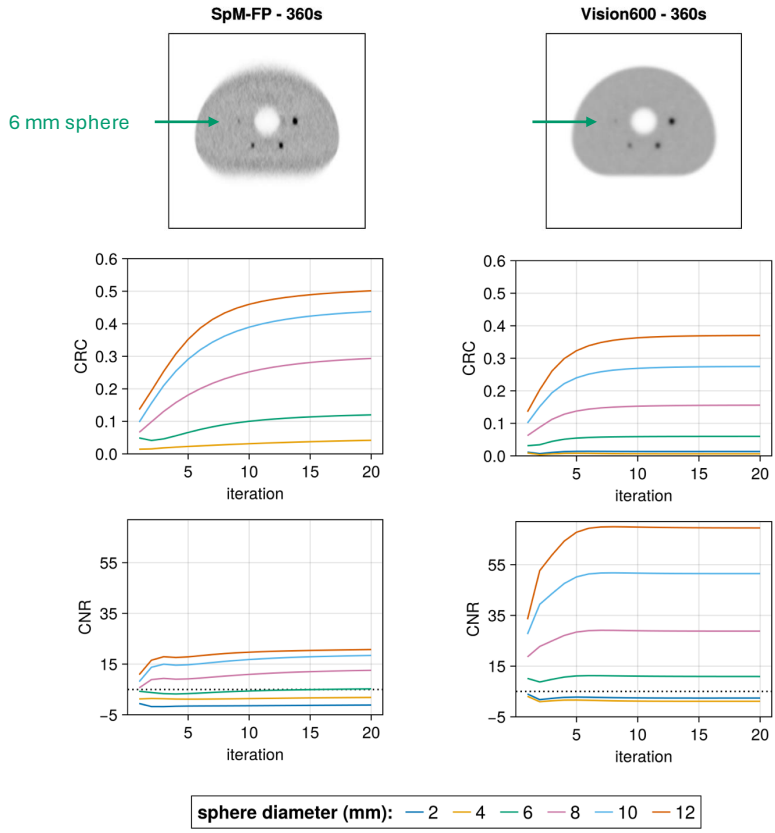

Figure 6.6: Reconstructions of the high-resolution torso phantom (10th iteration) simulated in the SpM-FP and Vision600, with the corresponding CRC and CNR at **360 seconds** for an STB activity concentration ratio of **4:1** with PSF modeling applied.

6.4 Discussion

As outlined in Chapter 2, the limited spatial resolution of PET systems leads to partial volume effects, which reduce the apparent activity concentration in small lesions. Because PET systems have a limited resolution

characterized by the point spread function of imaged point-like sources, small objects appear blurred, and lesions with low uptake can be missed when the system resolution exceeds roughly one-third of the lesion size. Detecting early-stage, low-uptake lesions therefore requires systems with superior spatial resolution, one of the main strengths of the SpM-FP design, as demonstrated in Chapter 5. To probe the limits of detectability, we reconstructed images with small voxel sizes of 0.5 mm and evaluated the detection of the three smallest spheres in the high-resolution torso phantom. The PSF model was anisotropic due to elongation along the direction orthogonal to the detector panels, reflecting the limited-angle geometry. However, because the phantom was centered in the field of view, where the system resolution is relatively uniform, the same PSF kernel was applied throughout the reconstruction for each scenario.

The results demonstrate that the SpM-FP can detect a 6-mm sphere at low uptake (4:1 contrast) with a 4-minute scan, and a 4-mm sphere at higher uptake (8:1 contrast) in less than 2 minutes. These results are consistent with the system's measured resolution of less than 2 mm parallel to the panels (X, Z) and around 3 mm in the orthogonal direction (Y). While such high resolution enhances detectability, the small PSF kernels also limit noise suppression, reducing CNR values across most spheres, especially the larger ones, highlighting the trade-off between resolution recovery and noise. The detector resolution study confirmed this behavior. When resolution was intentionally degraded, the resulting larger PSF kernels suppressed noise and increased CNR, at the expense of details. In contrast, the actual SpM-FP resolution preserved fine structures but yielded noisier images. This aligns with Muehllehner's observation [138] that improved system resolution reduces the number of counts required to achieve a given image quality. Although applying Gaussian filtering could have mitigated this difference, mostly for the larger spheres, our primary aim was to assess the detectability of the smallest spheres.

Comparisons with the Monte Carlo model of the Siemens Biograph Vision 600 must be interpreted cautiously. Differences in PSF modeling and especially in time-of-flight resolution influence detectability metrics. In his work, Kadrmas et al. showed how time-of-flight helps detect focal warm lesions in a noisy background [142]. The Vision 600, simulated with its reported 214 ps TOF resolution, benefited from reduced noise propagation and improved effective sensitivity. The SpM-FP, modeled with a more conservative TOF resolution of 300 ps, produced noisier

reconstructions. This helps explain why Vision 600 images appeared smoother and why its CNR values for the 6-mm sphere were nearly double those of the SpM-FP, despite neither system clearly resolving the lesion.

Experimental data from Siemens support these findings where the Biograph Vision 600 was able to detect a 5-mm sphere at a 6:1 contrast ratio as shown in Figure 6.7, largely due to its use of small crystal sizes that enhance resolution [119]. Other phantom studies confirm that lesion detectability strongly depends on acquisition time, lesion-to-background contrast, and reconstruction choices. For example, Oen et al. reported that with PSF modeling and Gaussian filtering, the 5-mm sphere could be detected on the Siemens mCT at 8:1 contrast within 150 seconds. Similarly, a multi-vendor study concluded that while all systems could resolve 4-mm spheres at very high uptake (15:1) with long acquisitions, detection of 5-6 mm spheres at routine scan times (2-4 minutes per bed position) required very high uptake values. In comparison, the SpM-FP achieved detection of a 6-mm sphere at a clinically realistic 4:1 contrast in roughly 4 minutes.

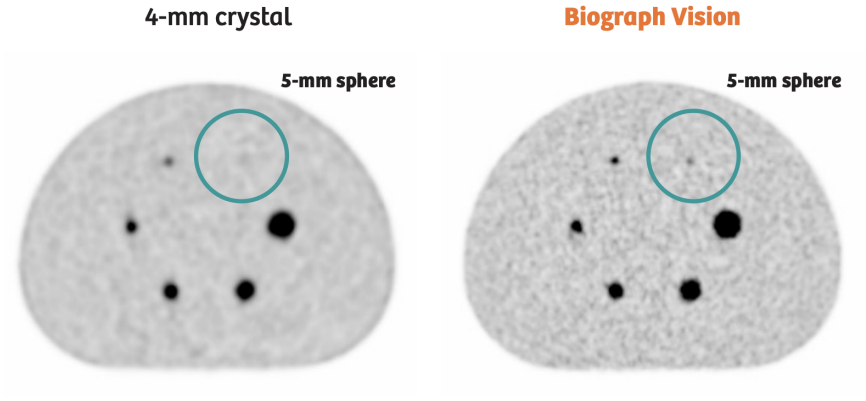

Figure 6.7: Reconstructions of the high resolution torso phantom with sphere sizes equal to 5.0, 7.9, 9.9, 12.4, 15.4 and 19.8 mm. Data acquired with 4-mm crystals and the Biograph Vision 600 for a 6:1 contrast-to-background ratio. Figure adapted from [119].

Together, these results underscore the importance of spatial resolution for lesion detection, which complements but does not replace TOF improvements. Although the SpM-FP's TOF resolution does not yet

reach the latest standards, its superior intrinsic resolution allows detection of very small lesions that might otherwise be missed. At the same time, TOF is particularly critical for the SpM-FP geometry: the flat-panel configuration suffers from elongation artifacts, especially at the top and bottom of the phantom. These artifacts can also bias CNR estimates, as background ROIs overlap with regions affected by elongation.

6.5 Conclusion

This chapter demonstrates the potential of the SpM-FP to deliver high-resolution PET imaging and improve the detectability of small lesions, even at modest uptake values. The results confirm that spatial resolution plays a decisive role in extending lesion detectability to sub-centimeter scales. Nonetheless, two main limitations remain. First, the flat-panel geometry introduces elongation artifacts due to incomplete angular coverage. Second, the system's TOF resolution is currently inferior to that of leading clinical systems, which amplifies noise in short acquisitions. Addressing these challenges is essential for clinical translation. In the next chapter, we introduce and evaluate a deep learning-based approach aimed at mitigating noise and reducing elongation artifacts. This strategy is expected to further enhance lesion detectability and image quality, thereby advancing the clinical potential of the SpM-FP system.

Chapter 7

Deep learning-based image restoration

7.1 Introduction

In Chapter 5, we evaluated the sparse medium flat panel (SpM-FP) design and demonstrated its potential for cost-effective PET imaging, offering good sensitivity and superior spatial resolution that yield clear advantages in lesion detection as demonstrated in Chapter 6. However, two main image quality challenges were evident in the reconstructed images:

- Elongation artifacts in the transverse and sagittal directions, caused by side gaps and incomplete angular coverage. These artifacts are inherent to flat-panel geometry and represent a fundamental limitation of the design.

- Noise from low-count statistics, which reduces image quality, even with the system's relatively high resolution. Although this issue could potentially be addressed by longer acquisition times than 2-3 minutes, doing so would undermine the high-throughput benefit that the SpM-FP is designed to offer.

The first limitation stems from fundamental differences between flat-panel and cylindrical geometries. In a cylindrical PET system, a full 180-degree angular projection range is available in the transverse plane, which, despite noise, limited detector resolution, dead time, and physical constraints, provides enough information to accurately reconstruct the

tracer distribution. Although 3D projections can be partly redundant and increase scatter, they improve sensitivity and provide essential cross-plane and oblique lines of response (LORs), especially in long-AFOV systems. In flat-panel designs, the available transverse angular coverage is less than 180 degrees. While the axial projection range adds extra information, it is not enough to fully compensate for missing projection angles. As a result, certain regions remain obscured, leading to structured elongation artifacts. In the NEMA IQ and modified IQ phantoms of the flat-panel designs (Figures 5.9 and 5.10), hot spheres appeared stretched, blurring tumor boundaries and creating the impression of artificially enlarged lesions. Similarly, in the XCAT phantom, edges perpendicular to the panels were poorly defined, with spillover of activity into cold regions, which could impact clinical interpretation despite otherwise good quantitative results. On the other hand, the SpM-FP achieved good image quality in 2-3 minutes, which is 4-5 times faster than the Siemens Biograph Vision 600, despite having less than double its sensitivity and a clear advantage in spatial resolution. However, the lower count statistics still cause noticeable noise, emphasizing the need for effective image denoising methods.
Therefore, for the SpM-FP to become clinically practical, both limited-angle artifacts and image noise need to be addressed. As discussed in Chapter 3, deep learning (DL)-based methods have been used separately for denoising and artifact correction. Here, we build on this approach by considering both factors together, while acknowledging their differences:

- Noise is random, high-frequency, and spread across the entire image, which lowers the signal-to-noise ratio (SNR).

- Limited-angle artifacts are directional and structured, caused by incomplete angular sampling.

Previous studies we conducted to denoise reconstructed XCAT images from data simulated in the L-FP design (not included in this work) showed that noise could be significantly reduced, both visually and through calculation of the contrast-to-noise ratio [143]. However, training a deep learning model on highly controlled, idealized data such as XCAT phantoms can lead to unrealistic performance. To better approximate clinical reality, we therefore switched to using PET patient data acquired on the Siemens Biograph Vision Quadra as part of the *Ultra Low Dose Challenge* [5].

In this chapter, we use a 2D U-Net architecture that has proven effective for denoising micro-PET data [97]. It is now adapted to not only reduce noise but also minimize elongation artifacts in SpM-FP reconstructed images, enhancing the potential for practical deep learning-based image restoration in flat-panel PET systems.

7.2 Materials and Methods

7.2.1 Training data

The dataset used to train the deep learning model consists of ^{18}F-fluorodeoxyglucose (^{18}F-FDG) scans from 30 patients of the *Ultra Low Dose Challenge* dataset acquired on the Siemens Biograph Quadra at Bern University hospital [5]. The corresponding CT data were also provided. The patient cohort comprised both genders and was selected to cover a broad range of body-mass indices (BMI: 16-48 kg/m^2) and ages (26-85 years). Acquisition times varied between 6 and 10 minutes, with injected activities ranging from 84 to 250 MBq calculated at 2.5 MBq/kg of body weight, in accordance with EANM guidelines. All PET scans were conducted approximately 1 hour post-injection to allow for tracer uptake. The full dose PET images served as the ***reference targets*** for training the deep learning model.

Input data: simulation and reconstruction
To generate patient-specific GATE simulations, two inputs were required for each subject: (i) an activity distribution map derived from the PET images, and (ii) an attenuation map representing the tissue composition derived from the CT images. The original CT images had a matrix size of 512 x 512 x 644 with voxel dimensions of 1.52 x 1.52 x 1.65 mm^2, while the PET images had a matrix size of 440 x 440 x 644 with isotropic voxel dimensions of 1.65 mm. The Quadra scanner with an AFOV of 106 cm was operated with a maximum ring difference of 85, and a single bed position. Images were reconstructed using PSF modeling and TOF with four iterations and five subsets. Prior to simulation, the CT images were preprocessed by cropping the patient bed from the transverse slices. Image co-registration was then performed in PMOD v4.4 [144]. To retain the higher spatial resolution of the CT data, the PET images were interpolated to the CT voxel grid. Cropping and positioning adjustments were applied to ensure correspondence with the scanning FOV and the moving SpM-FP design.

In the XCAT simulations described in Chapter 5, activity and attenuation maps were directly generated by the XCAT software by specifying various parameters. Here, both maps were derived from clinical PET/CT acquisitions. The PET images, originally expressed in Standardized Uptake Value (SUV), were converted to units of Bq/voxel for use in GATE. The CT images in Hounsfield Units (HU) were converted into a tissue classification map using tabulated stoichiometric conversion data from Schneider et al. [145]. Since scanner-specific calibration data from the Siemens Biograph Vision Quadra were not available, the generic conversion tables were applied. Nevertheless, visual inspection confirmed that the resulting tissue classification and spatial distribution were anatomically consistent. The final attenuation maps were generated in GATE and served as the ground-truth tissue maps for the simulation. Figure 7.1 shows the activity and attenuation maps for one of the patients, which were used as input for the GATE simulations. The moving SpM-FP configuration described in Chapter 5 was simulated to cover a total AFOV of 136 cm, with an acquisition time of three minutes per patient.

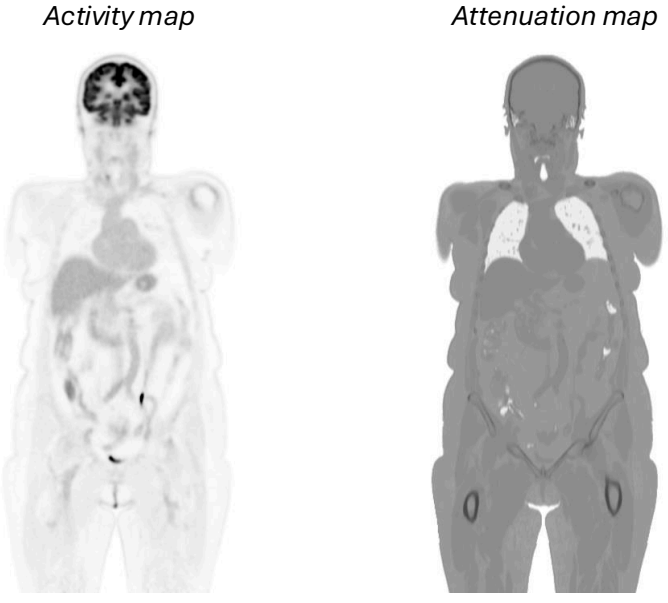

Figure 7.1: Activity and attenuation maps from one of the patient datasets used as input for the GATE simulation.

The ROOT outputs were post-processed and only true coincidences were used. For the reconstruction, a TOF resolution of 300 ps and detector blurring were modeled, along with attenuation correction. Patient-specific attenuation maps were derived from CT images by converting Hounsfield Units to linear attenuation coefficients using a bilinear transformation based on scanner-specific calibration curves [146]. Image reconstruction was performed using the MLEM algorithm with a voxel size of 1.52 x 1.52 x 1.65 mm^3, incorporating PSF modeling. Images from the fifth iteration were selected to balance between image contrast and noise.

7.2.2 Network architecture

Based on earlier successful DL-denoising work by our group [97], the model used in this study consists of a 2D convolutional neural network based on a four-layer U-Net architecture shown in Figure 7.2. It features an **encoder path** that gradually reduces spatial resolution at each level while increasing the number of feature maps, and a **decoder path** that restores the spatial resolution. Nine adjacent slices are stacked at the input to provide some 3D spatial context. Since the 2D U-Net processes each slice independently, this approach allows the model to capture information across slices; however, only the central slice is denoised during each forward pass, making the network a 2.5D U-Net.

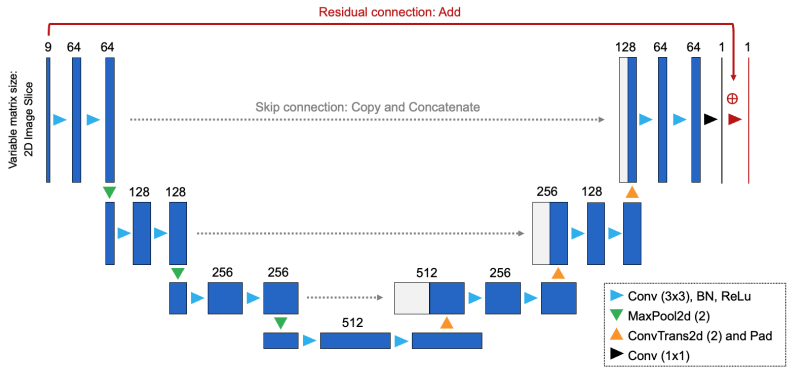

Figure 7.2: U-Net structure of the 2D convolutional neural network used in this work. The model takes 9 input slices.

Each encoder level performs two convolutional operations (kernel size of

3), followed by batch normalization (BN) and rectified linear unit (ReLU) activation. Moving to the second level, the 2D max-pooling operation downsamples the feature maps, reducing their spatial resolution by a factor of two. Then, the number of feature maps doubles from 64 to 128. This process continues until the bottleneck layer, where the feature depth reaches 512. In the decoder path, 2D transposed convolution operations are used for upsampling between levels. Skip connections concatenate the corresponding feature maps from the encoder to the decoder, allowing the model to preserve details lost during encoding. After each upsampling and concatenation, two blocks of convolutions, BN, and ReLu are applied. The final layer in the decoding path is a convolution with a kernel size of 1, used for mapping the feature maps back to the original spatial dimensions and predict the new pixel/voxel values. A residual connection between the input and output slices is also included to improve model convergence. This network ultimately outputs a DL-enhanced version of the input slice.

7.2.3 Training strategy

The dataset of 30 subjects was divided into training, validation, and testing sets in a 24:3:3 ratio, ensuring that each set included a range of BMIs and ages, both genders, and acquisition times (6 and 10 minutes). During preprocessing, a patient with a clearly visible high-uptake structure in the shoulder, confirmed by a clinician to be a residual tracer, was identified and set aside for testing, since no obvious lesions appeared in the training data. This enabled evaluation of the model's ability to handle focal high-uptake regions that resembles lesions. Multiple models were trained using different anatomical views: transverse only, sagittal only, both transverse and sagittal, and a combination of transverse, sagittal, and coronal. This approach was driven by the structure of the elongation artifacts in the SpM-FP system, which occur perpendicular to the detector panels and are visible in the transverse and sagittal planes but not in the coronal plane. As a result, including coronal slices, where elongation artifacts are not visible might reduce the model's ability to learn artifact-related features and could influence the learned weights and biases. Consequently, the results presented correspond to a model trained on transverse views only. All models were trained using paired images: the noisy, artifact-affected SpM-FP reconstructions as input and the corresponding Quadra images as ground-truth targets. Images were expressed in standardized uptake value (SUV) units, and mean

intensity normalization was applied to both input and target data to ensure consistent scaling across subjects. Data augmentation involved random horizontal and vertical flipping of the input images. Several loss functions were used, including mean absolute error (MAE), mean squared error (MSE) and a combination of MSE and VGG16 perceptual loss [147]. The perceptual loss uses the VGG16 deep convolutional neural network as a feature extractor, comparing high-level feature maps from intermediate layers instead of performing pixel-wise comparison like MAE and MSE. This method is expected to help maintain perceptual and structural image features. For the results presented in this work, we used the combined MSE and VGG16 perceptual loss. The Adam optimizer [148] was employed with a fixed learning rate of 10^{-4}. The batch size was set to 6, limited by available GPU memory. Early stopping was applied to end training once no further improvements in validation performance were observed. All trainings were conducted on a workstation equipped with an Intel(R) Core(TM) i7-9700K CPU (8 cores) and an NVIDIA GeForce RTX 2080 GPU (11 GB memory). Depending on the model and loss function, training times varied but generally under 12 hours, with an average of about 6 hours. Inference was carried out in the same orientation as training. For models trained on transverse slices, inference was done slice-by-slice in the transverse plane, and the 2D outputs were stacked to create the full 3D image volume.

7.2.4 Model evaluation

The performance of the trained model was evaluated on the testing dataset, which included three patients, with one of them having a high-uptake structure in the shoulder region. Both qualitative and quantitative analyses were conducted to assess the model's ability to reduce noise, mitigate elongation artifacts, and preserve contrast in the high-uptake structure. The details of the test patients are summarized in Table 7.1.

Qualitative evaluation

A visual inspection of the images was performed by examining the transverse, sagittal and coronal slices of the input, DL-enhanced, and target (Quadra) images. The assessment focused on evaluating noise reduction and the elimination of elongation artifacts, especially in the transverse and sagittal planes where these artifacts were most prominent. Particular attention was given to anatomical boundaries and small

Table 7.1: Demographic and acquisition details of the three test patients used in this study with injected activities, calculated at 2.5 MBq/kg according to EANM guidelines.

	BMI	Sex	Age	Injected Activity	Acquisition time
Patient 1 (P1)	27	M	59	179 MBq	6 min
Patient 2 (P2)	35	F	47	211 MBq	6 min
Patient 3 (P3)	24	F	50	132 MBq	10 min

structures that appeared elongated in the SpM-FP images, to see if the DL model could better define edges.

Quantitative evaluation
For quantitative analysis, three-dimensional volumes of interest (VOIs) were placed in homogeneous areas of the liver and leg to estimate image noise, calculated as the standard deviation of the SUV values within each VOI. In the patient with the high-uptake structure caused by residual tracer, a VOI covering most of the structure was drawn to determine the mean SUV and assess how the DL enhancement recovered focal uptake. Additionally, line profiles were drawn across the lesion-like feature and other small anatomical features that showed elongation artifacts in the input images. These profiles were compared across input, DL-enhanced, and target images to measure improvements in shape and boundary clarity. Line profiles through organ boundaries were also analyzed to evaluate transitions between regions, which often appear blurred or poorly defined in the original SpM-FP reconstructions.

7.3 Results

Various models were trained with different number of input slices (3, 9, and 17), loss functions, and anatomical views (one, two, or all three planes). Models that achieved good validation performance were further evaluated on the test patients summarized in Table 7.1. Overall, the differences in quantitative performance across models were not substantial, and the final selection was based on detailed visual assessment. Notably, models trained exclusively on transverse slices provided the best results in terms of noise reduction, correction of elongation artifacts, and reduction of spillover effects caused by the limited-angle coverage of the

flat-panel geometry. In contrast, models trained on sagittal or combined views exhibited higher noise levels and more distortions. The use of MSE loss alone also yielded acceptable results. Furthermore, increasing the number of input slices from three to nine improved both denoising and artifact-correction performance. The best performing model was trained exclusively on transverse slices using nine input slices and a combined loss function of both MSE and VGG16-based perceptual loss. The model achieved optimal performance at epoch 13, with a total training time of approximately six hours and about three hours to reach the best epoch. During inference, the model generated a DL-enhanced image for each patient in the test set in roughly 14 seconds.

Qualitative evaluation

Figure 7.3 shows the visual results for Patient 1, comparing the reconstructed SpM-FP data for a three-minute acquisition (input) with the DL-enhanced and reference images, the latter corresponding to the original Quadra reconstruction. Slices from all three anatomical views are shown, emphasizing those that include the high-uptake structure in the shoulder region. The DL-enhanced image exhibits a clear noise reduction, with improved delineation of anatomical structures, particularly in the sagittal and transverse planes. Compared to the Quadra reference, however, it remains slightly blurred, and some fine details such as spinal discs in the cervical and upper thoracic regions, abdominal organs, and brain structures are not fully recovered. Regarding limited angle artifacts, the high-uptake structure that appeared elongated in the sagittal and transverse input images is restored to a more rounded shape in the DL-enhanced image, although it does not perfectly match the reference in size. The network also improved the definition of edges perpendicular to the detector panels (top and bottom in the transverse view; left and right in the sagittal view), where activity in the input images appeared smeared or poorly separated from cold regions. In the DL-enhanced output, these edges are better defined, though not as sharply as in the Quadra reference, which shows a clear skin boundary. Figures 7.4 and 7.5 show similar results for Patients 2 and 3 who had no visible lesions but different BMIs and injected activities. Again, the DL model effectively reduced noise and improved edge definition and organ clarity, most notably in the transverse and sagittal planes. For Patient 3, a minor anatomical distortion was observed in the DL-enhanced coronal slice, where the brain appears slightly wider on the left side, suggesting

that the model may have introduced artificial tissue adjacent to the skull.

Quantitative evaluation

Regarding image noise, figure 7.6 illustrates the spherical VOIs used for analysis: 6 cm in diameter placed in the liver and leg for all three patients, and a 1-cm VOI placed over the high-uptake lesion-like structure for Patient 1. The standard deviation, representing voxel-to-voxel intensity variation within each VOI, was calculated for the input, DL-enhanced, and reference Quadra images of each patient. Figure 7.7 shows these results in a bar plot, demonstrating a consistent reduction in standard deviation for the DL-enhanced images across all patients. The noise levels were slightly lower than those of the reference images, consistent with the visual observations where the DL-enhanced images appeared smoother. Figure 7.8a shows the percentage SUV recovery in the SpM-FP and DL-enhanced images relative to the reference Quadra image. Within the 1-cm VOI of the lesion-like structure, SUV recovery improved from 62% in the input image to full recovery in the DL-enhanced image, indicating that the model effectively restored the structure contrast. Figure 7.8b presents a line profile across a transverse slice for Patient 2 illustrating how closely the DL-enhanced image follows the reference image in terms of SUV values. In contrast, the input image exhibits substantial fluctuations due to noise.

To assess the limited angle artifacts visible in the transverse and sagittal slices, Figure 7.9a presents a line profile through the lesion-like structure in the transverse plane. The broader peak observed in the input image reflects the elongation of the structure along the detector panel direction. The DL-enhanced image not only reduces this elongation but also shows improved SUV recovery, with a peak height closer to that of the reference image. In Figure 7.9b, the line profile across the liver boundary demonstrates that the DL-enhanced profile more closely follows the reference, while the input image shows elevated SUV values spilling into the adjacent region (encircled in black), consistent with the blurring and edge distortion caused by limited-angle effects. The improvements are further demonstrated in Figure 7.10 for Patient 2, where line profiles in the transverse and sagittal planes show reduced artifacts. Figure 7.11 presents similar enhancement across an elongated structure in the sagittal plane for Patient 3.

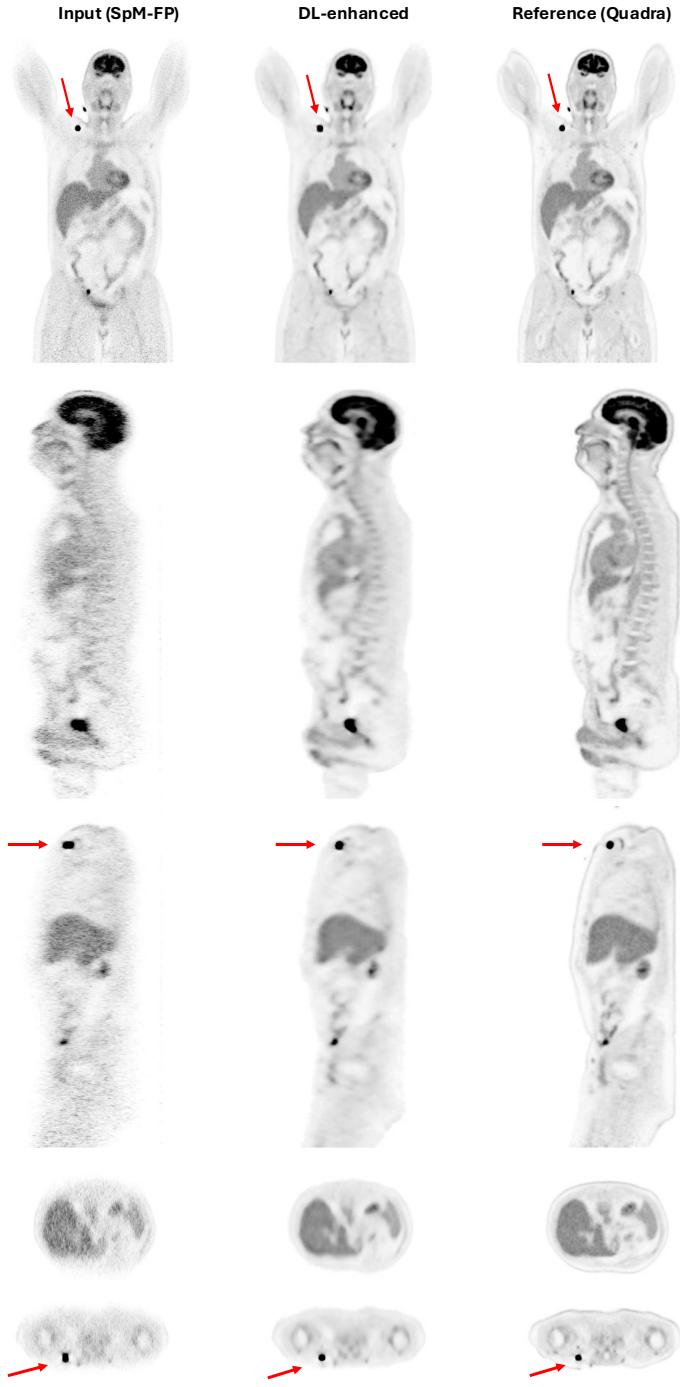

Figure 7.3: Patient 1: BMI 27 - 179 MBq. Coronal, sagittal and transverse slices of the input SpM-FP, DL-enhanced output, and the reference Quadra image. Slices including the high-uptake structure in the shoulder region are also shown.

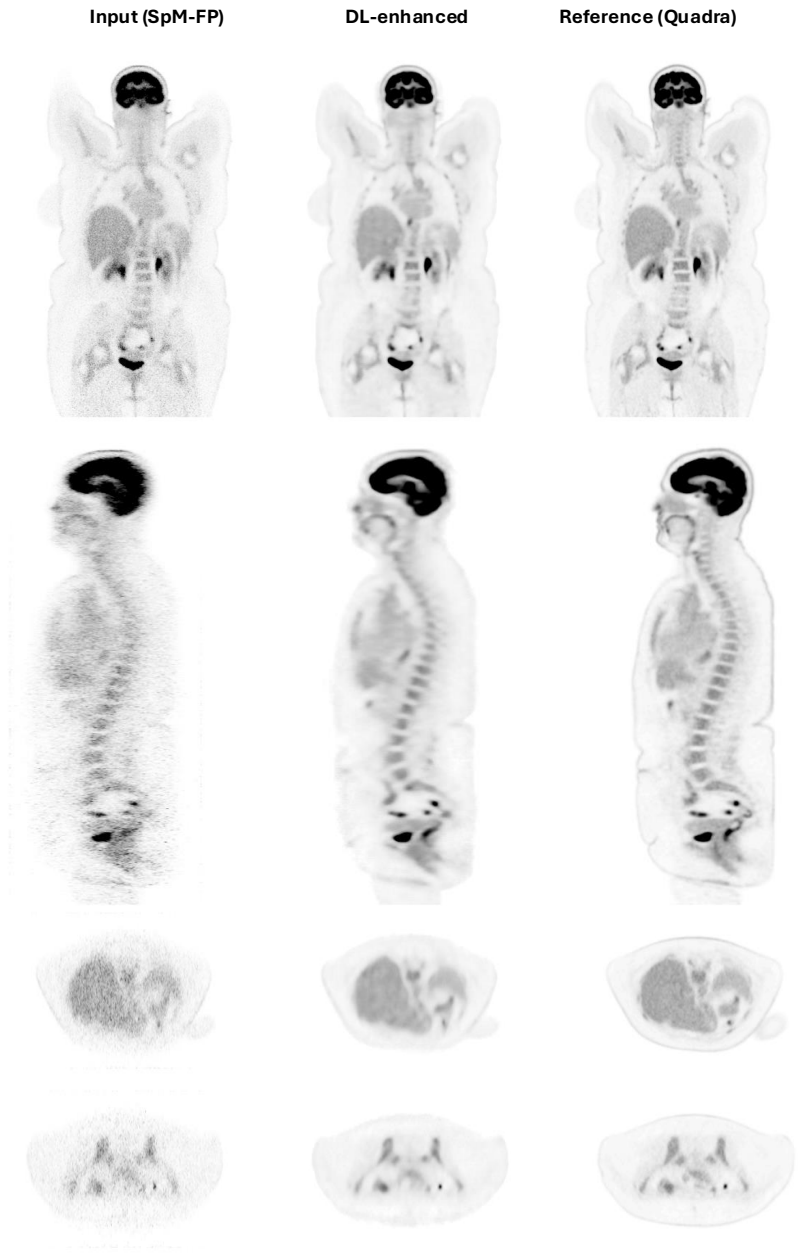

Figure 7.4: Patient 2: BMI 35 - 211 MBq. Coronal, sagittal and transverse slices of the input SpM-FP, DL-enhanced output, and the reference Quadra image.

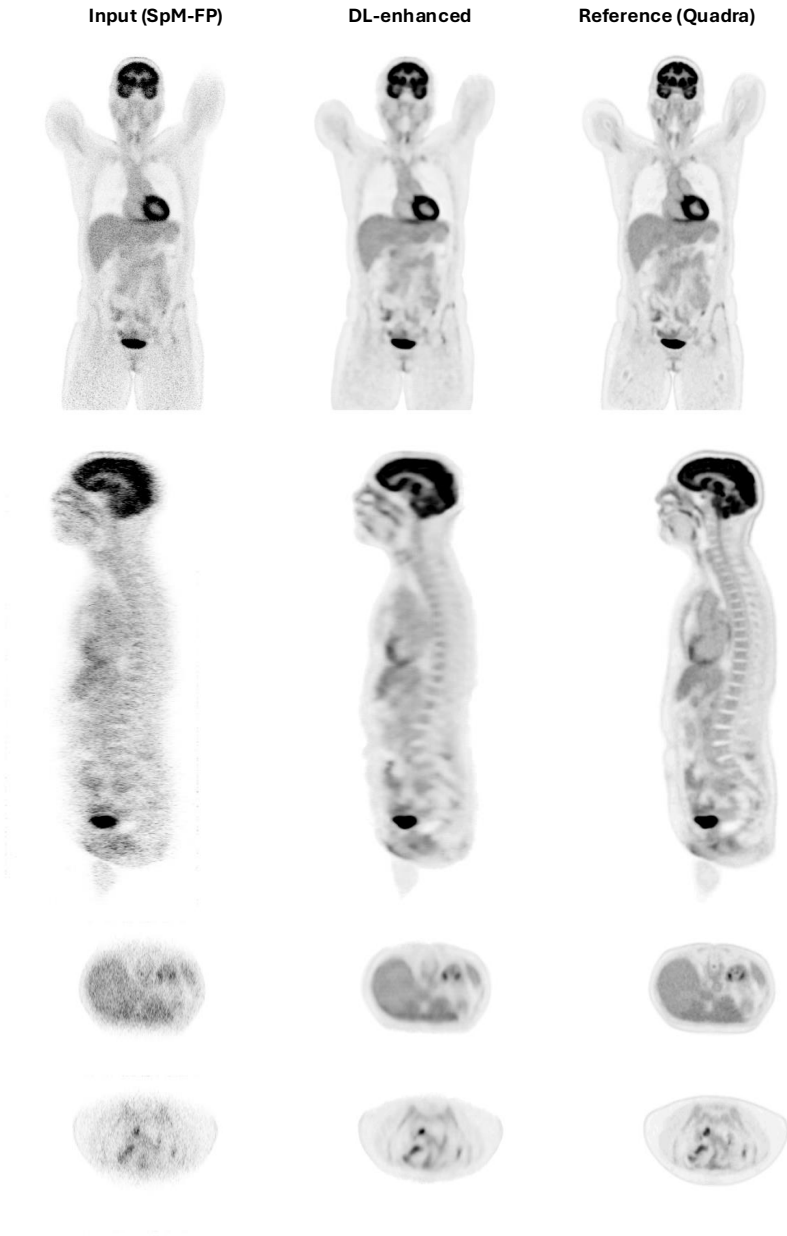

Figure 7.5: Patient 3: BMI 24 - 132 MBq. Coronal, sagittal and transverse slices of the input SpM-FP, DL-enhanced output, and the reference Quadra image.

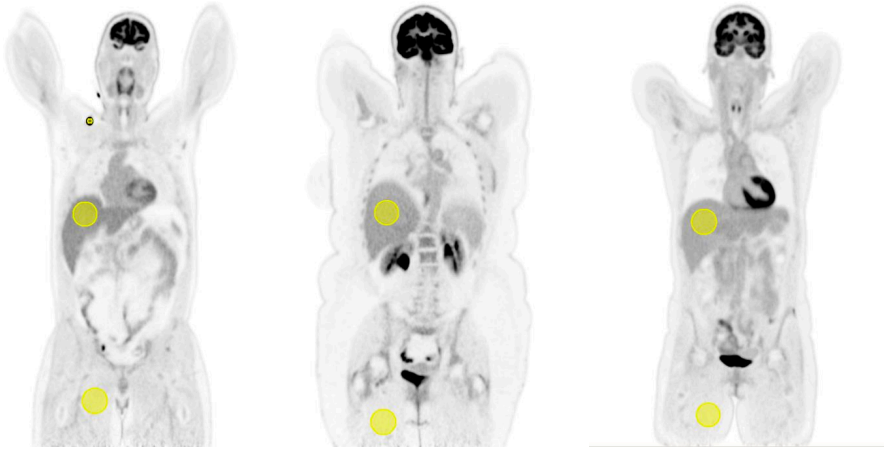

Figure 7.6: Coronal slices for all three patients showing the placement and size of the VOIs used for the quantitative analysis.

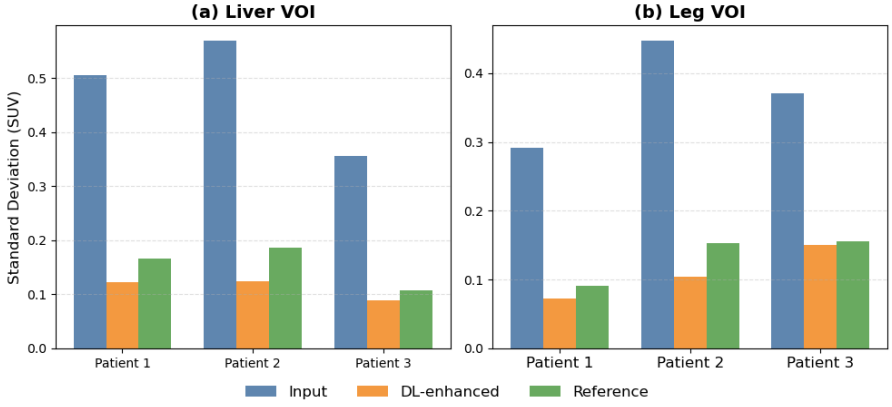

Figure 7.7: Quantitative evaluation of the noise in the input, DL-enhanced and the reference images showing the standard deviation values evaluated in the liver and leg VOIs.

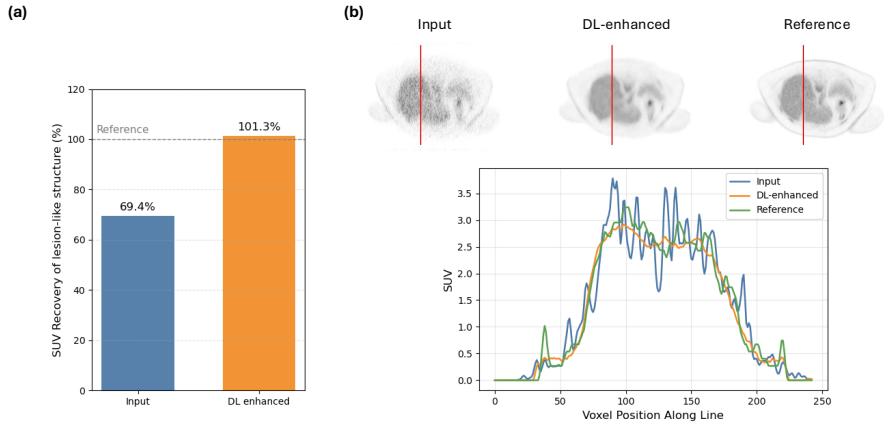

Figure 7.8: (a) Patient 1: Recovery of SUV in the high-uptake structure, caused by residual tracer, in the input and DL-enhanced images, expressed as a percentage relative to the SUV measured in the reference image, (b) Patient 2: Line profiles across the central transverse slice for all three images, showing that the DL-enhanced profile closely follows the reference profile except at the skin boundary, where uptake is not fully recovered.

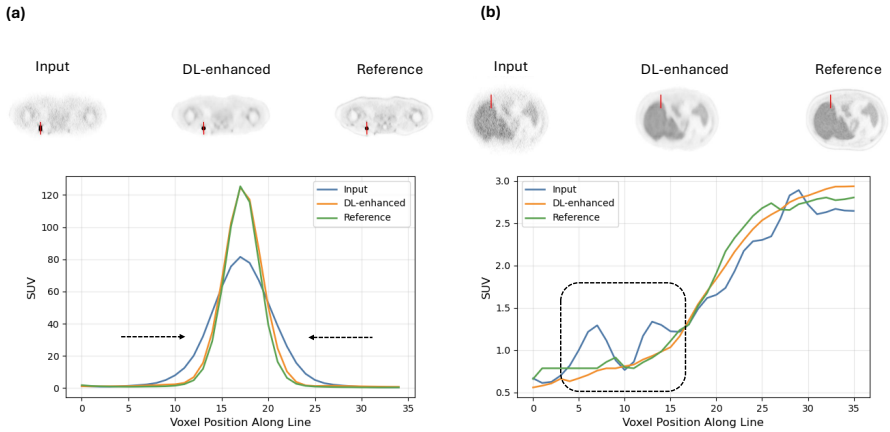

Figure 7.9: Patient 1: (a) Line profile across the high-uptake structure boundary, (b) line profile across the liver boundary, both in the transverse plane.

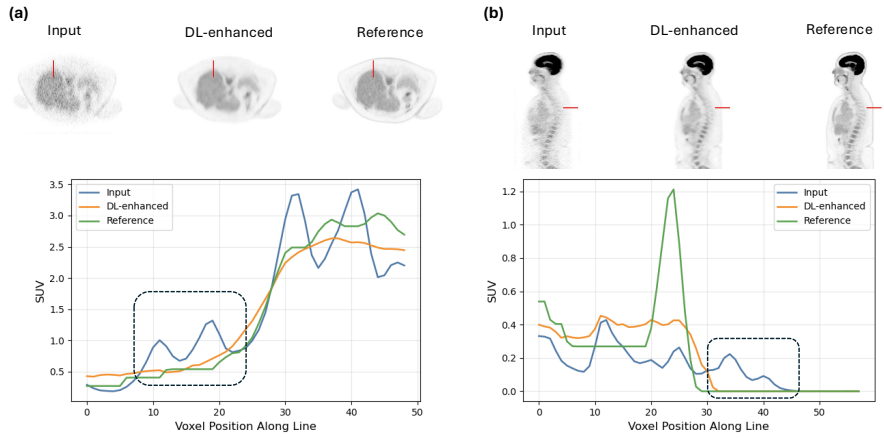

Figure 7.10: Patient 2: (a) Line profile across the liver boundary in the transverse plane, (b) line profile across the patient boundary in the sagittal plane.

7.4 Discussion

Based on the presented qualitative and quantitative results, the DL model effectively reduced image noise, although it caused some blurring and loss of sharpness compared to the reference images. Certain anatomical details, particularly in the brain and some thoracic regions, were not clearly visible. However, examining the input images of the test patients, especially in the sagittal and transverse planes, reveals that much of these fine details were already obscured by noise. Thus, relative to the input, the DL model was able to recover most structural information, even if the sharpness does not match that of the Quadra images. Regarding elongation and spillover caused by the limited-angle geometry, the network was capable of addressing these effects by redistributing activity into appropriate regions, reducing spillover, and providing better-defined edges. Lesion-like and small structures that appeared elongated in the input have regained their shape when compared to the reference images. However, the model was unable to fully restore skin uptake, likely due to limited-angle artifacts. Analyzing the data used to reconstruct the SpM-FP images, each three-minute scan across the 30 patients, yielded on average around 40 million true coincidence events, which is considerably lower than typical counts used in conventional PET reconstructions. The SpM-FP featuring 8 detector rows with 28-mm gaps along the axial

direction, moves during acquisition to cover a scanning FOV of 136 cm. Compared to the Quadra, and accounting for differences in acquisition time and system sensitivity (with the Quadra operating at MRD = 85), there was an approximately 9- to 14-fold difference in total counts. To put this into perspective, a recent systematic review of 55 studies highlighted the strong potential of deep learning models, such as generative adversarial networks and U-Nets, to produce high-quality PET images from low-dose acquisitions [149]. For instance, previous work has shown effective denoising even for dose-reduction factor as high as 50 [150]. However, those studies typically used pairs of low-dose full-dose data acquired on the same scanner, whereas our method used inputs and targets obtained from two different PET systems with inherently different characteristics. Moreover, the target (Quadra) images used as ground truth have lower spatial resolution than the images of the monolithic-based SpM-FP system. Additionally, the input images represent a convolution of both system resolutions, which, along with noise, likely contributed to the loss of sharpness that the DL model was unable to fully recover. Furthermore, the network was challenged to address both noise and limited-angle artifacts simultaneously. Despite these differences, the U-Net model effectively produced lower-noise outputs from high-noise, low-count SpM-FP images and mitigated the artifacts caused by the limited-angle geometry. Increasing the count statistics in the input images, by simulating longer acquisition times, would likely improve image quality and enhance the model's ability to learn fine anatomical structures. The dataset size was also relatively limited, particularly since only transverse slices were used for training. Expanding the dataset to include more patients and especially cases with lesions of varying uptake levels, could help the model generalize better. In such cases, however, careful image normalization strategies are essential to prevent distortions or biases around high-uptake lesions. Additionally, future work could explore 3D U-Net architectures, which have shown promise in PET denoising and artifact reduction [107]. These architectures could address both noise reduction and limited-angle correction. Although our 2.5D network incorporated multiple neighboring slices as input, its convolution remained two-dimensional. A 3D convolutional approach, though more memory intensive, could better exploit inter-slice spatial correlations and further enhance images.

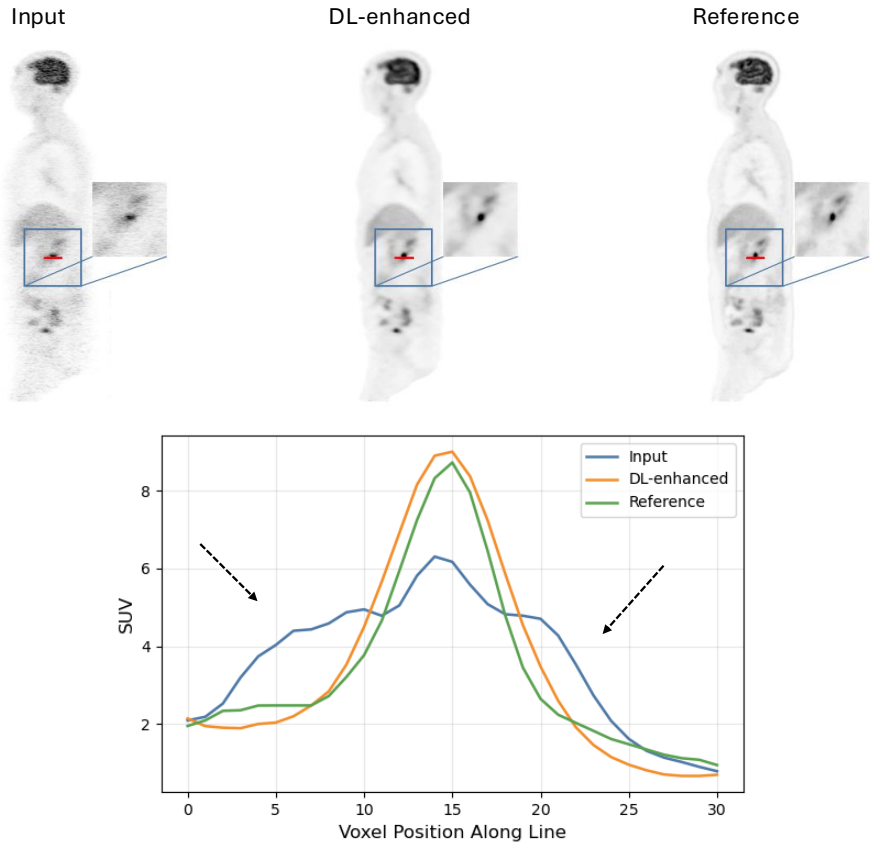

Figure 7.11: Patient 3: (a) Line profile across an elongated structure in the sagittal plane.

7.5 Conclusion

The results of this study demonstrate the strong potential of the deep learning model in effectively denoising and reducing limited-angle artifacts in images reconstructed with the SpM-FP design. Building upon this work, further optimization of the network architecture and training strategies could yield even greater improvements in image quality and artifact correction. The DL-enhanced results present the SpM-FP as a clinically viable PET system capable of producing high-spatial-resolution images with low noise and minimal artifacts. When combined with

its high throughput and cost-effective design, the SpM-FP represents a promising step toward more accessible, high-quality PET imaging. In summary, this study supports ongoing efforts to develop affordable, high-performance PET systems suitable for routine clinical practice.

Chapter 8

Conclusions and future perspectives

8.1 Summary

The purpose of this dissertation was to analyze and assess, through simulation, cost-effective and high-resolution medium-AFOV PET system designs based on monolithic scintillation detectors. Improving spatial resolution remains a central goal in PET imaging, especially with the rise of long AFOVs, and TOF-capable systems developed over the past decade. Moreover, the high cost of these systems has motivated the search for more affordable yet high-performance alternatives. This study investigated ring-based and flat-panel PET configurations with extended AFOVs. Their imaging performance was assessed and compared to current clinical systems. Based on simulation results and considerations of cost and throughput, the sparse medium-AFOV flat-panel design (SpM-FP) was identified as the most promising option. Compared to the state-of-the-art PET scanners, it showed excellent spatial resolution, higher sensitivity, cost efficiency and potential for increased throughput. A comprehensive performance evaluation was then conducted to determine the detection limits of the SpM-FP and compare them with those of existing clinical systems. Two main issues were identified: increased image noise due to short acquisition times and elongation artifacts caused by limited angular coverage resulting from side gaps in the flat-panel design. To address these issues, a deep learning model was developed and tested. The model successfully reduced both noise and elongation artifacts, producing smoother, higher-quality images. With these improvements

and the system's ability to detect lesions as small as 4 mm in diameter, the SpM-FP stands out as a promising, clinically feasible, and accessible solution that balances image quality, performance, and cost.

Chapter 2 covered the fundamental principles of PET physics and instrumentation, along with data acquisition and image reconstruction techniques. Chapter 3 reviewed recent technological advances in PET, with particular emphasis on time-of-flight (TOF) and depth-of-interaction (DOI) capabilities. TOF detectors enhance effective sensitivity and reduce noise propagation in reconstruction, allowing imaging with fewer angular projections, which is especially beneficial for geometries with limited angular coverage such as the flat-panel design proposed in this work. DOI measurement helps reduce parallax errors in both transverse and axial directions, which are more pronounced in flat-panel systems since detectors are positioned closer to the patient. The literature review also examined advances in scanner geometry and system design. This included long-AFOV systems that increase sensitivity and enable simultaneous imaging of multiple body regions, with axial lengths ranging from 32 cm to approximately 2 meters. Sparse geometries incorporating detector gaps were also discussed as cost-efficient methods to extend AFOV without additional detector modules. Furthermore, the flat-panel geometry was also analyzed, outlining its advantages and limitations to establish the rationale for its selection in this study. Finally, the simulation and performance evaluation framework used throughout this research was described in detail, including any necessary adaptations to the NEMA standards. A concise review of deep learning applications in PET imaging was also presented to give context to the development and integration of the proposed model for denoising and artifact correction.

Chapter 4 presented the results of extended-AFOV ring-based designs employing monolithic detectors. This step aimed to validate the detector technology within a conventional geometry and evaluate the system's performance with improved spatial resolution. Along with the expected improvements in sensitivity and spatial resolution, the proposed designs provided modularity as a key benefit. Starting with an initial AFOV of 36 cm, a modest extension over traditional scanners, the design can be expanded to 72 cm by combining two such modules in a dual-mode configuration, thereby boosting system sensitivity without substantially increasing cost. The two designs, labeled A and B, used monolithic LYSO crystals measuring 50 x 50 x 16 mm^3, which, based on previous measurements by our group, achieved an intrinsic spatial resolution of 1.14

mm and a DOI resolution of 2.67 mm. A third design, C, incorporated 50% detector gaps arranged in a checkered pattern, effectively doubling the axial length of design B to 145 cm without needing additional detectors. Designs A and B were simulated in GATE using digital models of the NEMA phantoms to evaluate key performance metrics: sensitivity, spatial resolution, and image quality, while design C was simulated and mainly evaluated for sensitivity. The checkered layout of design C also allowed to reduce the bore diameter, further enhancing sensitivity and making this configuration particularly suitable for pediatric applications. The results showed that design A, with its moderate AFOV extension, offers a significant sensitivity boost over traditional PET/CT systems but still requires bed movement for whole body scans. Conversely, design B, with an AFOV over 70 cm, achieved higher sensitivity and provided greater anatomical coverage in a single bed position. Both designs had a major benefit in maintaining sub-2 mm spatial resolution that was mostly uniform across the FOV, thanks to the use of monolithic detectors and their DOI capability, which effectively reduces parallax error. Image quality tests using the NEMA IQ phantom confirmed good contrast recovery, even for the smallest spheres. Nevertheless, it became clear that further optimization of the reconstruction software and parameter settings was necessary to ensure an accurate evaluation of system performance. The simulations used a coincidence timing resolution (CTR) of 200 ps, based on expected performance of the two designs. However, this value might be somewhat optimistic, as very few current state-of-the-art pixelated PET systems have achieved such timing precision. Therefore, a more conservative CTR value was adopted in subsequent studies to avoid overestimating timing performance. Image reconstruction during this phase was performed using the QETIR package; however, computational limitations impacted the image quality for designs A and B. For subsequent stages of this work, we switched to a different list-mode iterative reconstruction package developed at MEDISIP, optimized for GPU acceleration and tailored for non-standard geometries such as flat panels.

After validating the performance of monolithic detectors at the system level and demonstrating their potential for sub-2 mm resolution, this research shifted to a major design innovation: flat-panel, extended-AFOV system called the **Walk-Through PET (WT-PET)**. This concept marks a significant advancement, improving sensitivity and spatial resolution, reducing system costs, and increasing patient throughput. Unlike

traditional or long-AFOV ring-based systems that require patients to be positioned on a bed, the WT-PET allows the patient to stand between two vertical panels of monolithic detectors for a quick scan. Although this setup offers several notable benefits, it also presents specific challenges, especially related to image noise and limited-angle artifacts. In Chapter 5, we introduced and evaluated the WT-PET concept though two designs: the long flat-panel (L-FP) system with a 106 cm AFOV and the sparse medium-AFOV flat-panel (SpM-FP) design, which achieves more than half that coverage ($\sim$ 60 cm) using 2.5 times fewer detectors. The latter, providing significant cost savings and maintain high throughput, became the focus of the remaining work. Designed for limited panel movement relative to the patient, the SpM-FP enables brain-to-torso imaging while smoothing the sensitivity profile across detector gaps. Using a 300 ps timing resolution and monolithic LYSO detectors, the SpM-FP, estimated to be roughly 30% less expensive than the PET component of the Siemens Biograph Vision 600, achieved an average NEMA sensitivity of 25 kcps/MBq, approximately 1.5 times that of the Vision 600. The L-FP showed roughly 4.8 times the sensitivity of the SpM-FP. Both systems demonstrated sub-2 mm spatial resolution parallel to the panels (consistent with analytical estimates) and around 3 mm perpendicular to them. Importantly, the presence of detector gaps did not noticeably affect axial noise uniformity. Phantom studies showed that the SpM-FP produced high-quality images with good contrast and performance similar to the L-FP, but it required four times longer scan times. Phantom simulations showed that lesions as small as 4 mm were detectable, demonstrating the system's resolution limits and motivating the next chapter, which discusses performance trade-offs and the advantages of higher spatial resolution. However, limited angular coverage caused elongation artifacts perpendicular to the panels in the images, an issue addressed in Chapter 7 using deep learning.

In Chapter 6, a digital high-resolution torso phantom with sphere diameters ranging from 12 down to 2 mm was used to evaluate the detection limits of the SpM-FP under various acquisition times and sphere-to-background activity concentration ratios. The contrast recovery coefficient (CRC) and contrast-to-noise ratio (CNR) were employed as quantitative measures of sphere detectability. The results demonstrated that the SpM-FP can reliably detect 6 mm and even 4 mm spheres with practical acquisition times and standard NEMA activity concentration ratios used for the IQ phantom. An important observation was that

improved system resolution reduces the number of counts required to achieve a given image quality. Furthermore, the detectability performance of the SpM-FP was comparable to that of the Siemens Biograph Vision 600, despite the latter offering superior TOF resolution and full angular coverage. These findings suggest that combining high spatial resolution with improved TOF performance provide an optimal configuration for detecting small or early-stage lesions that are often missed in standard PET/CT systems with average resolution. Increased TOF capability is especially advantageous for systems with flat-panel geometry, as it reduces elongation artifacts and spillover effects caused by limited angular coverage. It also helps minimize noise spread during short scans. However, data on the exact timing resolution achievable with the SpM-FP system has not yet been obtained.

Chapter 7 introduced a deep learning-based method aimed at addressing the two main limitations seen in the XCAT and IQ phantom studies: image noise due to short scan times and artifacts caused by limited angular coverage. A 2D convolutional neural network (CNN) was trained using paired datasets for 30 Quadra patient scans obtained from the *Ultra Low Dose Challenge*. This data was simulated using the SpM-FP model in GATE to obtain reconstructions with notable noise and limited-angle artifacts. These were used as input images, and the network was trained to generate the corresponding Quadra images which served as less noisy and artifact-free references. The deep learning model effectively reduced both noise and limited-angle artifacts, producing images with enhanced visual quality. However, several avenues remain to further improve performance. Increasing the size and diversity of the training dataset, particularly by including more malignancies, using higher-quality inputs through longer acquisitions, and refining the network architecture could contribute to more robust performance. Implementing these enhancements could allow the DL model to serve as a complementary correction tool, enabling the SpM-FP system to deliver higher-quality images as part of a complete, optimized PET imaging solution.

8.2 Future perspectives

Based on the findings of this dissertation, several promising directions for future research can be identified.

First, in the work we presented, image reconstructions included only

true coincidence events. Random and scattered events were excluded through Monte Carlo tagging. This allowed us to evaluate the system while assuming that standard correction methods effectively remove randoms and scatters that degrade image quality. The next step should therefore involve including these events and applying the correction algorithms for scatter and randoms within the reconstruction framework developed at MEDISIP.

From another perspective, since the SpM-FP requires patients to stand upright between the detector panels for scan times of up to three minutes, longer than 30 seconds used in the WT-PET concept, external and physiological motion (such as cardiac and respiratory) becomes unavoidable. Such motion can affect the system's effective spatial resolution and compromise one of its main advantages. Our group is currently developing and testing an ergonomic prototype with healthy volunteers and patients to assess and reduce external patient motion while also exploring the integration of motion correction techniques directly into the reconstruction process. Another limitation is that the vertical panel design in its current form is not suitable for bedridden patients. However, the flexibility of using flat panels allows for adjusting the gap when needed to accommodate a bed insert. Although this group constitutes a small portion of the patient population, alternative configurations are being explored through simulations to identify optimal solutions.

In the context of deep learning, further optimization of the denoising and artifact-correction model remains a key goal. Future research could explore 3D U-Net architectures to better capture spatial information and use 3D data. Expanding the training dataset to include patients with a wider range of lesion sizes and uptake characteristics will also enhance model generalization. Another promising approach is to use the DL-enhanced image, which have reduced noise and limited-angle artifacts, as an initial estimate in MLEM reconstruction for flat-panel systems. This method could be effective for similar configurations, potentially speeding up convergence and enhancing the quality of the reconstructed images.

On a more technical note, the time-of-flight (TOF) resolution used for reconstructing the SpM-FP images in this study, is based on published estimates from comparable systems. However, it is crucial to replace these assumptions with experimentally measured values once data from the physical prototype become available. As the system is currently under construction, future reconstructions should be guided

by the TOF performance measured in the laboratory. Achieving a high TOF resolution will be particularly important for reducing image noise and mitigating limited-angle artifacts. Once the physical system is operational, validating the simulation and performance models used in this dissertation will be crucial. Such validation will confirm the accuracy of our predictions and help guide future design iterations, especially for innovative configurations based on flat-panel geometries.

Another open question for the WT-PET concept is the CT component. Conventional PET/CT systems use a circular source-detector geometries for anatomical localization and attenuation correction, which are incompatible with the flat-panel design. Our group is exploring a rectangular CT configuration that integrates well with the WT-PET geometry, using carbon nanotube (CNT)-based X-ray sources to create a rectangular source-detector array capable of acquiring 3D tomographic images [151]. However, this technology is still new and not yet clinically established. Alternatively, deep learning-based CT-less attenuation correction methods are gaining interest. These approaches aim to produce quantitatively accurate PET images without any CT acquisition. Ongoing work in our group in this area [152] could be expanded to support the WT-PET concept. However, a CT component will likely still be required within the WT-PET system to produce diagnostic-quality CT images, as the mentioned deep learning methods do not yet provide sufficient reliability.

8.3 Conclusion

Transitioning from conventional horizontal PET/CT scanners to vertical flat-panel geometries could provide important practical benefits in clinical PET imaging. The SpM-FP design offers greater flexibility, higher throughput, improved patient access and reduced costs, but it also introduces new technical challenges. To effectively address the current limitations of the SpM-FP (and flat-panel designs in general) careful system optimization is essential. Incorporating TOF reconstruction and detector-DOI capabilities is critical to ensure both measurement accuracy and high image quality. Having demonstrated a system with sub-2 mm spatial resolution throughout the FOV (thanks to DOI-capable detectors), the next key step is to experimentally measure and enhance TOF performance which allows to further reduce noise and artifacts and improve image quality. Once achieved, deep learning approaches,

as presented in this work, can be leveraged to address any remaining noise and artifacts, paving the way for a new generation of accessible, high-performance PET systems.

Looking forward, the next generation of PET systems will likely emerge from the combined evolution of detector technology, geometric design, and AI-supported approaches. Sparse geometries are gaining traction because they allow substantially longer axial coverage without a proportional increase in detector material. These configurations can deliver extended whole body coverage at reduced cost, while the associated non-uniform sensitivity profiles can be corrected in the reconstruction pipeline. On the detector side, continued improvements in TOF performance and DOI estimation will further enhance sensitivity and mitigate parallax errors, helping maintain uniform spatial resolution across the entire FOV. Monolithic scintillation detectors, thanks to their continuous 3D interaction positioning, are particularly promising in this regard. If ongoing research confirms that their timing performance approaches that of pixelated detectors, they may become central components in next-generation PET architectures, including those employing extended AFOV or unconventional geometries.

In parallel, AI-supported reconstruction methods, together with post-reconstruction techniques are expected to overcome several limitations of traditional statistical iterative algorithms. Deep neural networks offer the ability to integrate measurement statistics, physics models and prior information more flexibly, enabling improved noise-resolution trade-offs and reducing artifacts associated with sparse or limited-angle geometries. Post-reconstruction methods, such as image-domain denoising, super-resolution, or artifact-suppression networks, can further enhance image quality by correcting residual noise or distortions. For systems such as flat panels or axially sparse designs, these AI-driven approaches can partially compensate for missing angular information. While image-domain networks already provide substantial gains as we proved in this work, other approaches, such as unrolled iterative networks [153], may offer even deeper integration between physical modeling and learned priors, further advancing image quality, quantitative accuracy, and robustness.

Bibliography

[1] M. Abi-Akl, M. Dadgar, Y. Toufique, O. Bouhali, and S. Vandenberghe, "Monte Carlo simulation of the system performance of a long axial field-of-view PET based on monolithic LYSO detectors", *EJNMMI Physics*, vol. 10, no. 1, p. 37, Jun. 2023, ISSN: 2197-7364. DOI: 10.1186/s40658-023-00559-2.

[2] M. A. Akl, O. Bouhali, Y. Toufique, J. Karp, and S. Vandenberghe, "Monte Carlo sensitivity study of a long axial FOV PET scanner with patient adaptive rings", in *2019 IEEE Nuclear Science Symposium and Medical Imaging Conference (NSS/MIC)*, Manchester, United Kingdom: IEEE, Oct. 2019, pp. 1–3. DOI: 10.1109/nss/mic42101.2019.9059834.

[3] S. Vandenberghe et al., "Walk-through flat panel total-body PET: A patient-centered design for high throughput imaging at lower cost using DOI-capable high-resolution monolithic detectors", *European Journal of Nuclear Medicine and Molecular Imaging*, vol. 50, no. 12, pp. 3558–3571, Oct. 2023, ISSN: 1619-7089. DOI: 10.1007/s00259-023-06341-x.

[4] M. Abi-Akl, J. Maebe, B. Vervenne, O. Bouhali, C. Vanhove, and S. Vandenberghe, "Performance evaluation of a medium axial field-of-view sparse PET system based on flat panels of monolithic LYSO detectors: A simulation study", *EJNMMI Physics*, vol. 12, no. 1, p. 49, May 2025, ISSN: 2197-7364. DOI: 10.1186/s40658-025-00766-z.

[5] *Ultra Low Dose Grand Challenge*.

[6] J. W. Fletcher et al., "Recommendations on the Use of 18F-FDG PET in Oncology", *Journal of Nuclear Medicine*, vol. 49, no. 3, pp. 480–508, Mar. 2008, ISSN: 0161-5505, 2159-662X. DOI: 10.2967/jnumed.107.047787.

[7] D. L. Chen and P. E. Kinahan, "Multimodality molecular imaging of the lung", *Clinical and translational imaging*, vol. 2, no. 5, pp. 391–401, Oct. 2014, ISSN: 2281-5872. DOI: 10.1007/s40336-014-0084-9.

[8] L. M. Carter et al., "The Impact of Positron Range on PET Resolution, Evaluated with Phantoms and PHITS Monte Carlo Simulations for Conventional and Non-conventional Radionuclides", *Molecular imaging and biology*, vol. 22, no. 1, pp. 73–84, Feb. 2020, ISSN: 1536-1632. DOI: 10.1007/s11307-019-01337-2.

[9] Simon R. Cherry, James A. Sorenson, and Michael E. Phelps, *Physics in Nuclear Medicine*, Fourth Edition.

[10] Simon R. Cherry and Magnus Dahlbon, *PET: Physics, Instrumentation, and Scanners*.

[11] Z. C, S. Z, W. X, Z. X, and Y. Y, "The effects of inter-crystal scattering events on the performance of PET detectors", *Physics in medicine and biology*, vol. 64, no. 20, Oct. 2019, ISSN: 1361-6560. DOI: 10.1088/1361-6560/ab44f4.

[12] J. P. Schmall, J. S. Karp, M. Werner, and S. Surti, "Parallax error in long-axial field-of-view PET scanners—a simulation study", *Physics in medicine and biology*, vol. 61, no. 14, pp. 5443–5455, Jul. 2016, ISSN: 0031-9155. DOI: 10.1088/0031-9155/61/14/5443.

[13] "BGO scintillator", Epic-Crystal, Tech. Rep.

[14] "LYSO(Ce) Scintillator", Epic-Crystal, Tech. Rep.

[15] C. W. E. van Eijk, "Inorganic scintillators in medical imaging", *Physics in Medicine and Biology*, vol. 47, no. 8, R85–106, Apr. 2002, ISSN: 0031-9155. DOI: 10.1088/0031-9155/47/8/201.

[16] R. Lecomte, "Novel detector technology for clinical PET", *European Journal of Nuclear Medicine and Molecular Imaging*, vol. 36, no. 1, pp. 69–85, Mar. 2009, ISSN: 1619-7089. DOI: 10.1007/s00259-008-1054-0.

[17] M. Conti and B. Bendriem, "The new opportunities for high time resolution clinical TOF PET", *Clinical and Translational Imaging*, vol. 7, no. 2, pp. 139–147, Apr. 2019, ISSN: 2281-7565. DOI: 10.1007/s40336-019-00316-5.

[18] F. Zappa, S. Tisa, A. Tosi, and S. Cova, "Principles and features of single-photon avalanche diode arrays", *Sensors and Actuators A: Physical*, vol. 140, no. 1, pp. 103–112, Oct. 2007, ISSN: 0924-4247. DOI: 10.1016/j.sna.2007.06.021.

[19] M. Ito, J. Lee, and J. S. Lee, "Timing performance study of new fast PMTs with LYSO for time-of-flight PET", *IEEE Transactions on Nuclear Science*, vol. 60, pp. 30–37, Feb. 2013. DOI: 10.1109/TNS.2012.2215342.

[20] Y. Yang et al., "A Prototype PET Scanner with DOI-Encoding Detectors", *Journal of Nuclear Medicine*, vol. 49, no. 7, pp. 1132–1140, Jul. 2008, ISSN: 0161-5505, 2159-662X. DOI: 10.2967/jnumed.107.049791.

[21] M. Pizzichemi et al., "On light sharing TOF-PET modules with depth of interaction and 157 ps FWHM coincidence time resolution", *Physics in Medicine & Biology*, vol. 64, no. 15, p. 155 008, Aug. 2019, ISSN: 0031-9155. DOI: 10.1088/1361-6560/ab2cb0.

[22] D. L. Bailey, D. W. Townsend, P. E. Valk, and M. N. Maisey, Eds., *Positron Emission Tomography: Basic Sciences*. London: Springer, 2005, ISBN: 978-1-85233-798-8 978-1-84628-007-8. DOI: 10.1007/b136169.

[23] S. Vandenberghe, P. Moskal, and J. S. Karp, "State of the art in total body PET", *EJNMMI Physics*, vol. 7, no. 1, p. 35, May 2020, ISSN: 2197-7364. DOI: 10.1186/s40658-020-00290-2.

[24] S. R. Cherry, T. Jones, J. S. Karp, J. Qi, W. W. Moses, and R. D. Badawi, "Total-Body PET: Maximizing Sensitivity to Create New Opportunities for Clinical Research and Patient Care", *Journal of Nuclear Medicine: Official Publication, Society of Nuclear Medicine*, vol. 59, no. 1, pp. 3–12, Jan. 2018, ISSN: 1535-5667. DOI: 10.2967/jnumed.116.184028.

[25] D. R. Schaart, "Physics and technology of time-of-flight PET detectors", *Physics in Medicine and Biology*, vol. 66, no. 9, Apr. 2021, ISSN: 1361-6560. DOI: 10.1088/1361-6560/abee56.

[26] M. Conti, "Focus on time-of-flight PET: The benefits of improved time resolution", *European Journal of Nuclear Medicine and Molecular Imaging*, vol. 38, no. 6, pp. 1147–1157, Jun. 2011, ISSN: 1619-7089. DOI: 10.1007/s00259-010-1711-y.

[27] M. Conti, "Effect of randoms on signal-to-noise ratio in TOF PET", *IEEE Transactions on Nuclear Science*, vol. 53, no. 3, pp. 1188–1193, Jun. 2006, ISSN: 1558-1578. DOI: 10.1109/TNS.2006.875066.

[28] S. Surti, "Update on time-of-flight PET imaging", *Journal of Nuclear Medicine: Official Publication, Society of Nuclear Medicine*, vol. 56, no. 1, pp. 98–105, Jan. 2015, ISSN: 1535-5667. DOI: 10.2967/jnumed.114.145029.

[29] M. Soret, S. L. Bacharach, and I. Buvat, "Partial-Volume Effect in PET Tumor Imaging", *Journal of Nuclear Medicine*, vol. 48, no. 6, pp. 932–945, Jun. 2007, ISSN: 0161-5505. DOI: 10.2967/jnumed.106.035774.

[30] "Partial Volume Correction in PET imaging", in *Radiology Key*.

[31] R. Schofield et al., "Image reconstruction: Part 1 – understanding filtered back projection, noise and image acquisition", *Journal of Cardiovascular Computed Tomography*, vol. 14, no. 3, pp. 219–225, May 2020, ISSN: 1934-5925. DOI: 10.1016/j.jcct.2019.04.008.

[32] C. C. Watson, D. Newport, and M. E. Casey, "A Single Scatter Simulation Technique for Scatter Correction in 3D PET", in *Three-Dimensional Image Reconstruction in Radiology and Nuclear Medicine*, P. Grangeat and J.-L. Amans, Eds., Dordrecht: Springer Netherlands, 1996, pp. 255–268, ISBN: 978-94-015-8749-5. DOI: 10.1007/978-94-015-8749-5_18.

[33] L. M. Popescu, R. M. Lewitt, S. Matej, and J. S. Karp, "PET energy-based scatter estimation and image reconstruction with energy-dependent corrections", *Physics in Medicine and Biology*, vol. 51, no. 11, pp. 2919–2937, Jun. 2006, ISSN: 0031-9155. DOI: 10.1088/0031-9155/51/11/016.

[34] S. R. Cherry, M. Dahlbom, and E. J. Hoffman, "3D PET using a conventional multislice tomograph without septa", *Journal of Computer Assisted Tomography*, vol. 15, no. 4, pp. 655–668, 1991, ISSN: 0363-8715. DOI: 10.1097/00004728-199107000-00023.

[35] C. Johnson, Y. Yan, R. Carson, R. Martino, and M. Daube-Witherspoon, "A system for the 3D reconstruction of retracted-septa PET data using the EM algorithm", *IEEE Transactions on Nuclear Science*, vol. 42, no. 4, pp. 1223–1227, Aug. 1995, ISSN: 1558-1578. DOI: 10.1109/23.467875.

[36] T. Beyer et al., "A combined PET/CT scanner for clinical oncology", *Journal of Nuclear Medicine: Official Publication, Society of Nuclear Medicine*, vol. 41, no. 8, pp. 1369–1379, Aug. 2000, ISSN: 0161-5505.

[37] W. Moses and S. Derenzo, "Prospects for time-of-flight PET using LSO scintillator", *IEEE Transactions on Nuclear Science*, vol. 46, no. 3, pp. 474–478, Jun. 1999, ISSN: 1558-1578. DOI: 10.1109/23.775565.

[38] W. Moses, "Time of flight in PET revisited", *IEEE Transactions on Nuclear Science*, vol. 50, no. 5, pp. 1325–1330, Oct. 2003, ISSN: 1558-1578. DOI: 10.1109/TNS.2003.817319.

[39] D. R. Schaart, E. Charbon, T. Frach, and V. Schulz, "Advances in digital SiPMs and their application in biomedical imaging", *Nuclear Instruments and Methods in Physics Research Section A: Accelerators, Spectrometers, Detectors and Associated Equipment*, Advances in Detectors and Applications for Medicine, vol. 809, pp. 31–52, Feb. 2016, ISSN: 0168-9002. DOI: 10.1016/j.nima.2015.10.078.

[40] T. K. Lewellen, "Recent developments in PET detector technology", *Physics in Medicine and Biology*, vol. 53, no. 17, R287–317, Sep. 2008, ISSN: 0031-9155. DOI: 10.1088/0031-9155/53/17/R01.

[41] M. Conti, "State of the art and challenges of time-of-flight PET", *Physica medica: PM: an international journal devoted to the applications of physics to medicine and biology: official journal of the Italian Association of Biomedical Physics (AIFB)*, vol. 25, no. 1, pp. 1–11, Mar. 2009, ISSN: 1120-1797. DOI: 10.1016/j.ejmp.2008.10.001.

[42] J. S. Karp, S. Surti, M. E. Daube-Witherspoon, and G. Muehllehner, "Benefit of time-of-flight in PET: Experimental and clinical results", *Journal of Nuclear Medicine: Official Publication, Society of Nuclear Medicine*, vol. 49, no. 3, pp. 462–470, Mar. 2008, ISSN: 0161-5505. DOI: 10.2967/jnumed.107.044834.

[43] C. Lois et al., "An assessment of the impact of incorporating time-of-flight information into clinical PET/CT imaging", *Journal of Nuclear Medicine: Official Publication, Society of Nuclear Medicine*, vol. 51, no. 2, pp. 237–245, Feb. 2010, ISSN: 1535-5667. DOI: 10.2967/jnumed.109.068098.

[44] S. Vandenberghe, M. E. Daube-Witherspoon, R. M. Lewitt, and J. S. Karp, "Fast reconstruction of 3D time-of-flight PET data by axial rebinning and transverse mashing", *Physics in Medicine and Biology*, vol. 51, no. 6, pp. 1603–1621, Mar. 2006, ISSN: 0031-9155. DOI: 10.1088/0031-9155/51/6/017.

[45] S. Surti and J. S. Karp, "Design considerations for a limited angle, dedicated breast, TOF PET scanner", *Physics in Medicine and Biology*, vol. 53, no. 11, pp. 2911–2921, Jun. 2008, ISSN: 0031-9155. DOI: 10.1088/0031-9155/53/11/010.

[46] H. Liu, T. Omura, M. Watanabe, and T. Yamashita, "Development of a depth of interaction detector for γ-rays", *Nuclear Instruments and Methods in Physics Research Section A: Accelerators, Spectrometers, Detectors and Associated Equipment*, vol. 459, no. 1, pp. 182–190, Feb. 2001, ISSN: 0168-9002. DOI: 10.1016/S0168-9002(00)00939-6.

[47] L. Eriksson, C. L. Melcher, M. Zhuravleva, M. Eriksson, H. Rothfuss, and M. Conti, "Phoswich solutions for the PET DOI problem", *Nuclear Instruments and Methods in Physics Research Section A: Accelerators, Spectrometers, Detectors and Associated Equipment*, NIMA_4th International Conference on Imaging Techniques in Subatomic Physics, Astrophysics, Medicine, Biology and Industry, vol. 648, S288–S292, Aug. 2011, ISSN: 0168-9002. DOI: 10.1016/j.nima.2010.11.049.

[48] C. Levin, "Design of a high-resolution and high-sensitivity scintillation crystal array for PET with nearly complete light collection", *IEEE Transactions on Nuclear Science*, vol. 49, no. 5, pp. 2236–2243, Oct. 2002, ISSN: 1558-1578. DOI: 10.1109/TNS.2002.803870.

[49] J. Du, G. Ariño-Estrada, X. Bai, and S. R. Cherry, "Performance comparison of dual-ended readout depth-encoding PET detectors based on BGO and LYSO crystals", *Physics in Medicine and Biology*, vol. 65, no. 23, Nov. 2020, ISSN: 1361-6560. DOI: 10.1088/1361-6560/abc365.

[50] S. Blinder et al., "Influence of depth of interaction on spatial resolution and image quality for the HRRT", in *IEEE Nuclear Science Symposium Conference Record, 2005*, vol. 3, Oct. 2005, 5 pp.–1769. DOI: 10.1109/NSSMIC.2005.1596662.

[51] S. Krishnamoorthy, E. Blankemeyer, P. Mollet, S. Surti, R. Van Holen, and J. S. Karp, "Performance evaluation of the MOLECUBES β-CUBE-a high spatial resolution and high sensitivity small animal PET scanner utilizing monolithic LYSO scintillation detectors", *Physics in Medicine and Biology*, vol. 63, no. 15, p. 155 013, Jul. 2018, ISSN: 1361-6560. DOI: 10.1088/1361-6560/aacec3.

[52] G. Borghi, V. Tabacchini, and D. R. Schaart, "Towards monolithic scintillator based TOF-PET systems: Practical methods for detector calibration and operation", *Physics in Medicine and Biology*, vol. 61, no. 13, pp. 4904–4928, Jul. 2016, ISSN: 1361-6560. DOI: 10.1088/0031-9155/61/13/4904.

[53] G. Borghi, B. J. Peet, V. Tabacchini, and D. R. Schaart, "A 32 mm × 32 mm × 22 mm monolithic LYSO:Ce detector with dual-sided digital photon counter readout for ultrahigh-performance TOF-PET and TOF-PET/MRI", *Physics in Medicine and Biology*, vol. 61, no. 13, pp. 4929–4949, Jul. 2016, ISSN: 1361-6560. DOI: 10.1088/0031-9155/61/13/4929.

[54] A. González-Montoro et al., "Detector block performance based on a monolithic LYSO crystal using a novel signal multiplexing method", *Nuclear Instruments and Methods in Physics Research Section A: Accelerators, Spectrometers, Detectors and Associated Equipment*, New Developments In Photodetection 2017, vol. 912, pp. 372–377, Dec. 2018, ISSN: 0168-9002. DOI: 10.1016/j.nima.2017.10.098.

[55] M. Stockhoff, M. Decuyper, R. Van Holen, and S. Vandenberghe, "High-resolution monolithic LYSO detector with 6-layer depth-of-interaction for clinical PET", *Physics in Medicine and Biology*, vol. 66, no. 15, Jul. 2021, ISSN: 1361-6560. DOI: 10.1088/1361-6560/ac1459.

[56] G. Borghi, V. Tabacchini, S. Seifert, and D. Schaart, "Experimental Validation of an Efficient Fan-Beam Calibration Procedure for -Nearest Neighbor Position Estimation in Monolithic Scintillator Detectors", *Nuclear Science, IEEE Transactions on*, vol. 62, pp. 57–67, Feb. 2015. DOI: 10.1109/TNS.2014.2375557.

[57] F. Müller, D. Schug, P. Hallen, J. Grahe, and V. Schulz, "Gradient Tree Boosting-Based Positioning Method for Monolithic Scintillator Crystals in Positron Emission Tomography", *IEEE*

Transactions on Radiation and Plasma Medical Sciences, vol. 2, no. 5, pp. 411–421, Sep. 2018, ISSN: 2469-7303. DOI: 10.1109/TRPMS.2018.2837738.

[58] P. Carra et al., "A neural network-based algorithm for simultaneous event positioning and timestamping in monolithic scintillators", *Physics in Medicine and Biology*, vol. 67, no. 13, Jun. 2022, ISSN: 1361-6560. DOI: 10.1088/1361-6560/ac72f2.

[59] B. A. Spencer et al., "Performance Evaluation of the uEXPLORER Total-Body PET/CT Scanner Based on NEMA NU 2-2018 with Additional Tests to Characterize PET Scanners with a Long Axial Field of View", *Journal of Nuclear Medicine: Official Publication, Society of Nuclear Medicine*, vol. 62, no. 6, pp. 861–870, Jun. 2021, ISSN: 1535-5667. DOI: 10.2967/jnumed.120.250597.

[60] B. Dai et al., "Performance evaluation of the PennPET explorer with expanded axial coverage", *Physics in Medicine and Biology*, vol. 68, no. 9, p. 095 007, Apr. 2023, ISSN: 1361-6560. DOI: 10.1088/1361-6560/acc722.

[61] G. A. Prenosil et al., "Performance Characteristics of the Biograph Vision Quadra PET/CT System with a Long Axial Field of View Using the NEMA NU 2-2018 Standard", *Journal of Nuclear Medicine: Official Publication, Society of Nuclear Medicine*, vol. 63, no. 3, pp. 476–484, Mar. 2022, ISSN: 1535-5667. DOI: 10.2967/jnumed.121.261972.

[62] I. Alberts et al., "Clinical performance of long axial field of view PET/CT: A head-to-head intra-individual comparison of the Biograph Vision Quadra with the Biograph Vision PET/CT", *European Journal of Nuclear Medicine and Molecular Imaging*, vol. 48, no. 8, pp. 2395–2404, Jul. 2021, ISSN: 1619-7089. DOI: 10.1007/s00259-021-05282-7.

[63] R. L. Smith, L. Bartley, C. O'Callaghan, K. M. Bradley, and C. Marshall, *NEMA NU 2-2018 performance evaluation of a new generation digital 32-cm axial field-of-view Omni Legend PET-CT*, Aug. 2023. DOI: 10.48550/arXiv.2308.06255. arXiv: 2308.06255 [physics].

[64] H. Zhang et al., "Performance Characteristics of a New Generation 148-cm Axial Field-of-View uMI Panorama GS PET/CT System with Extended NEMA NU 2-2018 and EARL Standards", *Journal of Nuclear Medicine*, vol. 65, no. 12, pp. 1974–1982, Dec. 2024, ISSN: 0161-5505, 2159-662X. DOI: 10.2967/jnumed.124.267963.

[65] G. Li et al., "Performance Evaluation of the uMI Panorama PET/CT System in Accordance with the National Electrical Manufacturers Association NU 2-2018 Standard", *Journal of Nuclear Medicine*, vol. 65, no. 4, pp. 652–658, Apr. 2024, ISSN: 0161-5505, 2159-662X. DOI: 10.2967/jnumed.123.265929.

[66] J. S. Karp et al., "PennPET Explorer: Design and Preliminary Performance of a Whole-Body Imager", *Journal of Nuclear Medicine: Official Publication, Society of Nuclear Medicine*, vol. 61, no. 1, pp. 136–143, Jan. 2020, ISSN: 1535-5667. DOI: 10.2967/jnumed.119.229997.

[67] F. P. Schmidt et al., "Impact of the maximum ring difference on image quality and noise characteristics of a total-body PET/CT scanner", *Zeitschrift für Medizinische Physik*, Oct. 2023, ISSN: 0939-3889. DOI: 10.1016/j.zemedi.2023.09.001.

[68] E. Yoshida et al., "Development of a Whole-Body Dual Ring OpenPET for in-Beam PET", *IEEE Transactions on Radiation and Plasma Medical Sciences*, vol. 1, no. 4, pp. 293–300, Jul. 2017, ISSN: 2469-7303. DOI: 10.1109/TRPMS.2017.2703823.

[69] S. A. Zein, N. A. Karakatsanis, M. Issa, A. A. Haj-Ali, and S. A. Nehmeh, "Physical performance of a long axial field-of-view PET scanner prototype with sparse rings configuration: A Monte Carlo simulation study", *Medical Physics*, vol. 47, no. 4, pp. 1949–1957, 2020, ISSN: 2473-4209. DOI: 10.1002/mp.14046.

[70] S. A. Zein, N. A. Karakatsanis, M. Conti, and S. A. Nehmeh, "Monte Carlo Simulation of the Siemens Biograph Vision PET With Extended Axial Field of View Using Sparse Detector Module Rings Configuration", *IEEE Transactions on Radiation and Plasma Medical Sciences*, vol. 5, no. 3, pp. 331–342, May 2021, ISSN: 2469-7303. DOI: 10.1109/TRPMS.2020.3034676.

[71] M. E. Daube-Witherspoon, V. Viswanath, M. E. Werner, and J. S. Karp, "Performance Characteristics of Long Axial Field-of-View PET Scanners with Axial Gaps", *IEEE transactions on radiation*

and plasma medical sciences, vol. 5, no. 3, pp. 322–330, May 2021, ISSN: 2469-7311. DOI: 10.1109/trpms.2020.3027257.

[72] E. Lee, M. E. Werner, J. S. Karp, and S. Surti, "Design Optimization of a Time-Of-Flight, Breast PET Scanner", *IEEE Transactions on Nuclear Science*, vol. 60, no. 3, pp. 1645–1652, Jun. 2013, ISSN: 1558-1578. DOI: 10.1109/TNS.2013.2257849.

[73] T. Zeng et al., "Design and system evaluation of a dual-panel portable PET (DP-PET)", *EJNMMI Physics*, vol. 8, no. 1, p. 47, Jun. 2021, ISSN: 2197-7364. DOI: 10.1186/s40658-021-00392-5.

[74] A. Gonzalez-Montoro et al., "Design and proof of concept of a double-panel TOF-PET system", *EJNMMI physics*, vol. 11, no. 1, p. 73, Aug. 2024, ISSN: 2197-7364. DOI: 10.1186/s40658-024-00674-8.

[75] I. Ozsahin, M. S. Musa, and G. S. P. Mok, "Simulation of a High-Sensitivity Adjustable-FOV PET Scanner", in *2018 IEEE Nuclear Science Symposium and Medical Imaging Conference Proceedings (NSS/MIC)*, Nov. 2018, pp. 1–3. DOI: 10.1109/NSSMIC.2018.8824440.

[76] M. Dadgar, J. Maebe, M. Abi Akl, B. Vervenne, and S. Vandenberghe, "A simulation study of the system characteristics for a long axial FOV PET design based on monolithic BGO flat panels compared with a pixelated LSO cylindrical design", *EJNMMI Physics*, vol. 10, no. 1, p. 75, Dec. 2023, ISSN: 2197-7364. DOI: 10.1186/s40658-023-00593-0.

[77] C. L. Melcher, "Scintillation crystals for PET", *Journal of Nuclear Medicine: Official Publication, Society of Nuclear Medicine*, vol. 41, no. 6, pp. 1051–1055, Jun. 2000, ISSN: 0161-5505.

[78] H. Lee, "Monte Carlo methods for medical imaging research", *Biomedical Engineering Letters*, vol. 14, no. 6, pp. 1195–1205, Nov. 2024, ISSN: 2093-985X. DOI: 10.1007/s13534-024-00423-x.

[79] S. Jan et al., "GATE: A simulation toolkit for PET and SPECT", *Physics in Medicine and Biology*, vol. 49, no. 19, pp. 4543–4561, Oct. 2004, ISSN: 0031-9155. DOI: 10.1088/0031-9155/49/19/007.

[80] M. Stockhoff, S. Jan, A. Dubois, S. R. Cherry, and E. Roncali, "Advanced optical simulation of scintillation detectors in GATE V8.0: First implementation of a reflectance model based on measured data", *Physics in Medicine and Biology*, vol. 62, no. 12, pp. L1–L8, Jun. 2017, ISSN: 1361-6560. DOI: 10.1088/1361-6560/aa7007.

[81] V. Viswanath et al., "GATE simulations to study extended axial FOVs for the PennPET Explorer scanner", in *2017 IEEE Nuclear Science Symposium and Medical Imaging Conference (NSS/MIC)*, Oct. 2017, pp. 1–5. DOI: 10.1109/NSSMIC.2017.8532747.

[82] R. Brun and F. Rademakers, "ROOT — An object oriented data analysis framework", *Nuclear Instruments and Methods in Physics Research Section A: Accelerators, Spectrometers, Detectors and Associated Equipment*, New Computing Techniques in Physics Research V, vol. 389, no. 1, pp. 81–86, Apr. 1997, ISSN: 0168-9002. DOI: 10.1016/S0168-9002(97)00048-X.

[83] *Performance Measurements of Positron Emission Tomographs (PETS)*, https://www.nema.org/standards/view/performance-measurements-of-positron-emission-tomographs-(pets), Nov. 2024.

[84] M.E. Daube-Witherspoon, B. Dai, and J.S. Karp, *Phantom Studies to Characterize Total-Body PET System Performance*, Oral, May 2022.

[85] K. Gong, S. R. Cherry, and J. Qi, "On the assessment of spatial resolution of PET systems with iterative image reconstruction", *Physics in Medicine and Biology*, vol. 61, no. 5, N193–202, Mar. 2016, ISSN: 1361-6560. DOI: 10.1088/0031-9155/61/5/N193.

[86] N. A. Karakatsanis, M. H. Nehmeh, M. Conti, G. Bal, A. J. González, and S. A. Nehmeh, "Physical performance of adaptive axial FOV PET scanners with a sparse detector block rings or a checkerboard configuration", *Physics in Medicine and Biology*, vol. 67, no. 10, May 2022, ISSN: 1361-6560. DOI: 10.1088/1361-6560/ac6aa1.

[87] W. P. Segars, G. Sturgeon, S. Mendonca, J. Grimes, and B. M. W. Tsui, "4D XCAT phantom for multimodality imaging research", *Medical Physics*, vol. 37, no. 9, pp. 4902–4915, Sep. 2010, ISSN: 0094-2405. DOI: 10.1118/1.3480985.

[88] *Deep Learning*, https://www.deeplearningbook.org/.

[89] K. Yan, X. Wang, L. Lu, and R. M. Summers, "DeepLesion: Automated mining of large-scale lesion annotations and universal lesion detection with deep learning", *Journal of Medical Imaging (Bellingham, Wash.)*, vol. 5, no. 3, p. 036 501, Jul. 2018, ISSN: 2329-4302. DOI: 10.1117/1.JMI.5.3.036501.

[90] I. Häggström et al., "Deep learning for [18F]fluorodeoxyglucose-PET-CT classification in patients with lymphoma: A dual-centre retrospective analysis", *The Lancet. Digital health*, vol. 6, no. 2, e114–e125, Feb. 2024, ISSN: 2589-7500. DOI: 10.1016/S2589-7500(23)00203-0.

[91] C. Wang et al., "Data-driven risk stratification and precision management of pulmonary nodules detected on chest computed tomography", *Nature Medicine*, vol. 30, no. 11, pp. 3184–3195, Nov. 2024, ISSN: 1546-170X. DOI: 10.1038/s41591-024-03211-3.

[92] T. Jo, K. Nho, and A. J. Saykin, "Deep Learning in Alzheimer's Disease: Diagnostic Classification and Prognostic Prediction Using Neuroimaging Data", *Frontiers in Aging Neuroscience*, vol. 11, p. 220, Aug. 2019, ISSN: 1663-4365. DOI: 10.3389/fnagi.2019.00220.

[93] X. Yu et al., "A deep learning approach for automatic tumor delineation in stereotactic radiotherapy for non-small cell lung cancer using diagnostic PET-CT and planning CT", *Frontiers in Oncology*, vol. 13, Aug. 2023, ISSN: 2234-943X. DOI: 10.3389/fonc.2023.1235461.

[94] A. V. Dalca, G. Balakrishnan, J. Guttag, and M. R. Sabuncu, "Unsupervised learning of probabilistic diffeomorphic registration for images and surfaces", *Medical Image Analysis*, vol. 57, pp. 226–236, Oct. 2019, ISSN: 1361-8415. DOI: 10.1016/j.media.2019.07.006.

[95] J. Liu et al., "Virtual high-count PET image generation using a deep learning method", *Medical Physics*, vol. 49, no. 9, pp. 5830–5840, Sep. 2022, ISSN: 2473-4209. DOI: 10.1002/mp.15867.

[96] F. M. Muller, J. Maebe, C. Vanhove, and S. Vandenberghe, "Dose reduction and image enhancement in micro-CT using deep learning", *Medical Physics*, vol. 50, no. 9, pp. 5643–5656, 2023, ISSN: 2473-4209. DOI: 10.1002/mp.16385.

[97] F. M. Muller et al., "Image Denoising of Low-Dose PET Mouse Scans with Deep Learning: Validation Study for Preclinical Imaging Applicability", *Molecular Imaging and Biology*, Oct. 2023, ISSN: 1860-2002. DOI: 10.1007/s11307-023-01866-x.

[98] Q. Yang et al., "Low-Dose CT Image Denoising Using a Generative Adversarial Network With Wasserstein Distance and Perceptual Loss", *IEEE Transactions on Medical Imaging*, vol. 37, no. 6, pp. 1348–1357, Jun. 2018, ISSN: 1558-254X. DOI: 10.1109/TMI.2018.2827462.

[99] Y. Huang, A. Preuhs, G. Lauritsch, M. Manhart, X. Huang, and A. Maier, *Data Consistent Artifact Reduction for Limited Angle Tomography with Deep Learning Prior*, Aug. 2019. DOI: 10.48550/arXiv.1908.06792. arXiv: 1908.06792 [eess].

[100] W. S. McCulloch and W. Pitts, "A logical calculus of the ideas immanent in nervous activity", *Bulletin of Mathematical Biology*, vol. 52, no. 1, pp. 99–115, Jan. 1990, ISSN: 1522-9602. DOI: 10.1007/BF02459570.

[101] F. Rosenblatt, "The perceptron: A probabilistic model for information storage and organization in the brain", *Psychological Review*, vol. 65, no. 6, pp. 386–408, Nov. 1958, ISSN: 0033-295X. DOI: 10.1037/h0042519.

[102] Y. Lecun, "Generalization and network design strategies", in *Connectionism in Perspective*, R. Pfeifer, Z. Schreter, F. Fogelman, and L. Steels, Eds., Zurich, Switzerland: Elsevier, 1989.

[103] O. Ronneberger, P. Fischer, and T. Brox, *U-Net: Convolutional Networks for Biomedical Image Segmentation*, May 2015. DOI: 10.48550/arXiv.1505.04597. arXiv: 1505.04597 [cs].

[104] K. Gong, J. Guan, C.-C. Liu, and J. Qi, "PET Image Denoising Using a Deep Neural Network Through Fine Tuning", *IEEE Transactions on Radiation and Plasma Medical Sciences*, vol. 3, no. 2, pp. 153–161, Mar. 2019, ISSN: 2469-7303. DOI: 10.1109/TRPMS.2018.2877644.

[105] S. Kaplan and Y.-M. Zhu, "Full-Dose PET Image Estimation from Low-Dose PET Image Using Deep Learning: A Pilot Study", *Journal of Digital Imaging*, vol. 32, no. 5, pp. 773–778, Oct. 2019, ISSN: 1618-727X. DOI: 10.1007/s10278-018-0150-3.

[106] W. Lu et al., "An investigation of quantitative accuracy for deep learning based denoising in oncological PET", *Physics in Medicine and Biology*, vol. 64, no. 16, p. 165 019, Aug. 2019, ISSN: 1361-6560. DOI: 10.1088/1361-6560/ab3242.

[107] J. Schaefferkoetter et al., "Convolutional neural networks for improving image quality with noisy PET data", *EJNMMI Research*, vol. 10, no. 1, p. 105, Sep. 2020, ISSN: 2191-219X. DOI: 10.1186/s13550-020-00695-1.

[108] H. Liu, J. Wu, W. Lu, J. A. Onofrey, Y.-H. Liu, and C. Liu, "Noise reduction with cross-tracer and cross-protocol deep transfer learning for low-dose PET", *Physics in Medicine and Biology*, vol. 65, no. 18, p. 185 006, Sep. 2020, ISSN: 1361-6560. DOI: 10.1088/1361-6560/abae08.

[109] M. De Summa et al., "Denoising approaches by SubtlePET™ artificial intelligence in positron emission tomography (PET) for clinical routine application", *Clinical and Translational Imaging*, vol. 12, no. 4, pp. 393–402, Aug. 2024, ISSN: 2281-7565. DOI: 10.1007/s40336-024-00625-4.

[110] G. Bonardel et al., "Clinical and phantom validation of a deep learning based denoising algorithm for F-18-FDG PET images from lower detection counting in comparison with the standard acquisition", *EJNMMI Physics*, vol. 9, p. 36, May 2022. DOI: 10.1186/s40658-022-00465-z.

[111] K. Miwa et al., "Innovations in clinical PET image reconstruction: Advances in Bayesian penalized likelihood algorithm and deep learning", *Annals of Nuclear Medicine*, vol. 39, no. 9, pp. 875–898, Sep. 2025, ISSN: 1864-6433. DOI: 10.1007/s12149-025-02088-7.

[112] J. Dong, J. Fu, and Z. He, "A deep learning reconstruction framework for X-ray computed tomography with incomplete data", *PloS One*, vol. 14, no. 11, e0224426, 2019, ISSN: 1932-6203. DOI: 10.1371/journal.pone.0224426.

[113] C.-C. Liu and H.-M. Huang, "Partial-ring PET image restoration using a deep learning based method", *Physics in Medicine and Biology*, vol. 64, no. 22, p. 225 014, Nov. 2019, ISSN: 1361-6560. DOI: 10.1088/1361-6560/ab4aa9.

[114] J. Wang, J. Liang, J. Cheng, Y. Guo, and L. Zeng, "Deep learning based image reconstruction algorithm for limited-angle translational computed tomography", *PloS One*, vol. 15, no. 1, e0226963, 2020, ISSN: 1932-6203. DOI: 10.1371/journal.pone.0226963.

[115] S. Barutcu, S. Aslan, A. K. Katsaggelos, and D. Gürsoy, "Limited-angle computed tomography with deep image and physics priors", *Scientific Reports*, vol. 11, no. 1, p. 17 740, Sep. 2021, ISSN: 2045-2322. DOI: 10.1038/s41598-021-97226-2.

[116] Jens Maebe, "Improvement of Spatial Resolution in Monolithic Detectors for Clinical PET", Ph.D. dissertation, Ghent University.

[117] X. Zhang, R. D. Badawi, S. R. Cherry, and J. Qi, "Theoretical Study of the Benefit of Long Axial Field-of-View PET on Region of Interest Quantification", *Physics in medicine and biology*, vol. 63, no. 13, p. 135 010, Jun. 2018, ISSN: 0031-9155. DOI: 10.1088/1361-6560/aac815.

[118] J. Van Sluis et al., "Performance Characteristics of the Digital Biograph Vision PET/CT System", *Journal of Nuclear Medicine*, vol. 60, no. 7, pp. 1031–1036, Jul. 2019, ISSN: 0161-5505, 2159-662X. DOI: 10.2967/jnumed.118.215418.

[119] Siemens Healthineers, "Biograph Vision PET/CT Brochure", Tech. Rep.

[120] *PET image reconstruction software QETIR*, https://www.ugent.be/ea/ibitech/en/research/medisip/software-lab/software-lab13.htm, Page.

[121] M. Dadgar and P. Kowalski, "GATE Simulation Study of the 24-module J-PET Scanner: Data Analysis and Image Reconstruction", *Acta Physica Polonica B*, vol. 51, no. 1, p. 309, 2020, ISSN: 0587-4254, 1509-5770. DOI: 10.5506/APhysPolB.51.309.

[122] W. Krzemien, A. Gajos, K. Kacprzak, K. Rakoczy, and G. Korcyl, "J-PET Framework: Software platform for PET tomography data reconstruction and analysis", *SoftwareX*, vol. 11, p. 100 487, Jan. 2020, ISSN: 2352-7110. DOI: 10.1016/j.softx.2020.100487.

[123] S. Surti, M. E. Werner, and J. S. Karp, "Study of PET scanner designs using clinical metrics to optimize the scanner axial FOV and crystal thickness", *Physics in Medicine and Biology*, vol. 58, no. 12, pp. 3995–4012, Jun. 2013, ISSN: 1361-6560. DOI: 10.1088/0031-9155/58/12/3995.

[124] M. Gao, M. E. Daube-Witherspoon, J. S. Karp, and S. Surti, "Total-Body PET System Designs with Axial and Transverse Gaps: A Study of Lesion Quantification and Detectability", *Journal of Nuclear Medicine*, vol. 66, no. 2, pp. 323–329, Feb. 2025, ISSN: 0161-5505, 2159-662X. DOI: 10.2967/jnumed.124.267769.

[125] P. Moskal et al., "Simulating NEMA characteristics of the modular total-body J-PET scanner-an economic total-body PET from plastic scintillators", *Physics in Medicine and Biology*, vol. 66, no. 17, Sep. 2021, ISSN: 1361-6560. DOI: 10.1088/1361-6560/ac16bd.

[126] G. Razdevšek et al., "Flexible and modular PET: Evaluating the potential of TOF-DOI panel detectors", *Medical Physics*, vol. n/a, no. n/a, ISSN: 2473-4209. DOI: 10.1002/mp.17741.

[127] T. A. Cabutto, S. P. Heeney, S. V. Ault, G. Mao, and J. Wang, "An Overview of the Julia Programming Language", in *Proceedings of the 2018 International Conference on Computing and Big Data*, ser. ICCBD '18, New York, NY, USA: Association for Computing Machinery, Sep. 2018, pp. 87–91, ISBN: 978-1-4503-6540-6. DOI: 10.1145/3277104.3277119.

[128] J. Guo, H. Qi, Y. Xu, Z. Chen, S. Li, and L. Zhou, "Iterative Image Reconstruction for Limited-Angle CT Using Optimized Initial Image", *Computational and Mathematical Methods in Medicine*, vol. 2016, p. 5 836 410, 2016, ISSN: 1748-670X. DOI: 10.1155/2016/5836410.

[129] Y. Yang et al., "Optimization and performance evaluation of the microPET II scanner for in vivo small-animal imaging", *Physics in Medicine and Biology*, vol. 49, no. 12, pp. 2527–2545, Jun. 2004, ISSN: 0031-9155. DOI: 10.1088/0031-9155/49/12/005.

[130] R. Albert, *Vision: Human and Electronic.* New York: Plenum Press, 1973, ISBN: 978-0-306-30732-4.

[131] W. W. Moses, "Fundamental limits of spatial resolution in PET",

[132] M. EL Katib, E. M. Chakir, R. Sebihi, H. Saikouk, and O. Nhila, "Validation of a Monte Carlo model of the uEXPLORER total-body PET scanner using GATE code", *Radiation Physics and Chemistry*, vol. 210, p. 111 052, Sep. 2023, ISSN: 0969-806X. DOI: 10.1016/j.radphyschem.2023.111052.

[133] H. Bal et al., "Improving PET spatial resolution and detectability for prostate cancer imaging", *Physics in medicine and biology*, vol. 59, no. 15, pp. 4411–4426, Aug. 2014, ISSN: 0031-9155. DOI: 10.1088/0031-9155/59/15/4411.

[134] I. Polycarpou, C. Tsoumpas, A. P. King, and P. K. Marsden, "Impact of respiratory motion correction and spatial resolution on lesion detection in PET: A simulation study based on real MR dynamic data", *Physics in Medicine and Biology*, vol. 59, no. 3, pp. 697–713, Feb. 2014, ISSN: 1361-6560. DOI: 10.1088/0031-9155/59/3/697.

[135] P. Cheebsumon et al., "Effects of image characteristics on performance of tumor delineation methods: A test-retest assessment", *Journal of Nuclear Medicine: Official Publication, Society of Nuclear Medicine*, vol. 52, no. 10, pp. 1550–1558, Oct. 2011, ISSN: 1535-5667. DOI: 10.2967/jnumed.111.088914.

[136] F. Hofheinz et al., "An automatic method for accurate volume delineation of heterogeneous tumors in PET", *Medical Physics*, vol. 40, no. 8, p. 082 503, Aug. 2013, ISSN: 2473-4209. DOI: 10.1118/1.4812892.

[137] J. Yan, J. Schaefferkoetter, M. Conti, and D. Townsend, "A method to assess image quality for Low-dose PET: Analysis of SNR, CNR, bias and image noise", *Cancer Imaging*, vol. 16, no. 1, p. 26, Aug. 2016, ISSN: 1470-7330. DOI: 10.1186/s40644-016-0086-0.

[138] G. Muehllehner, "Effect of resolution improvement on required count density in ECT imaging: A computer simulation", *Physics in Medicine and Biology*, vol. 30, no. 2, pp. 163–173, Feb. 1985, ISSN: 0031-9155. DOI: 10.1088/0031-9155/30/2/005.

[139] J. Nuyts, S. Z. Pour, S. Noë, G. Schramm, and A. Rezaei, "An analytical model for comparing the effective sensitivity of different PET systems", in *2023 IEEE Nuclear Science Symposium, Medical Imaging Conference and International Symposium on Room-Temperature Semiconductor Detectors (NSS MIC RTSD)*, Nov. 2023, pp. 1–1. DOI: 10.1109/NSSMICRTSD49126.2023.10338481.

[140] L. Kaufman, D. Shosa, L. Crooks, and J. Ewins, "Technology Needs in Medical Imaging", *IEEE Transactions on Medical Imaging*, vol. 1, no. 1, pp. 11–16, Jul. 1982, ISSN: 1558-254X. DOI: 10.1109/TMI.1982.4307543.

[141] A. Morey, F. Noo, and D. J. Kadrmas, "Effect of Using 2 mm Voxels on Observer Performance for PET Lesion Detection", *IEEE Transactions on Nuclear Science*, vol. 63, no. 3, pp. 1359–1366, Jun. 2016, ISSN: 1558-1578. DOI: 10.1109/TNS.2016.2518177.

[142] D. J. Kadrmas, M. E. Casey, M. Conti, B. W. Jakoby, C. Lois, and D. W. Townsend, "Impact of time-of-flight on PET tumor detection", *Journal of Nuclear Medicine: Official Publication, Society of Nuclear Medicine*, vol. 50, no. 8, pp. 1315–1323, Aug. 2009, ISSN: 0161-5505. DOI: 10.2967/jnumed.109.063016.

[143] Maya Abi Akl, *Deep learning image denoising for a cost-effective WT-PET design with sparse detector coverage*, Oral, Isola d'Elba, Italy, May 2024.

[144] *PMOD: PET Image Analysis and Kinetic Modeling Software*, Zurich, Switzerland.

[145] W. Schneider, T. Bortfeld, and W. Schlegel, "Correlation between CT numbers and tissue parameters needed for Monte Carlo simulations of clinical dose distributions", *Physics in Medicine & Biology*, vol. 45, no. 2, p. 459, Feb. 2000, ISSN: 0031-9155. DOI: 10.1088/0031-9155/45/2/314.

[146] J. P. J. Carney, D. W. Townsend, V. Rappoport, and B. Bendriem, "Method for transforming CT images for attenuation correction in PET/CT imaging", *Medical Physics*, vol. 33, no. 4, pp. 976–983, Apr. 2006, ISSN: 0094-2405. DOI: 10.1118/1.2174132.

[147] K. Simonyan and A. Zisserman, *Very Deep Convolutional Networks for Large-Scale Image Recognition*, Apr. 2015. DOI: 10.48550/arXiv.1409.1556. arXiv: 1409.1556 [cs].

[148] D. P. Kingma and J. Ba, *Adam: A Method for Stochastic Optimization*, Jan. 2017. DOI: 10.48550/arXiv.1412.6980. arXiv: 1412.6980 [cs].

[149] N. Seyyedi, A. Ghafari, N. Seyyedi, and P. Sheikhzadeh, "Deep learning-based techniques for estimating high-quality full-dose positron emission tomography images from low-dose scans: A systematic review", *BMC Medical Imaging*, vol. 24, no. 1, p. 238, Sep. 2024, ISSN: 1471-2342. DOI: 10.1186/s12880-024-01417-y.

[150] S. Xue et al., "A cross-scanner and cross-tracer deep learning method for the recovery of standard-dose imaging quality from low-dose PET", *European Journal of Nuclear Medicine and Molecular Imaging*, vol. 49, no. 6, pp. 1843–1856, May 2022, ISSN: 1619-7089. DOI: 10.1007/s00259-021-05644-1.

[151] B. Vervenne, J. Maebe, and S. Vandenberghe, "Feasibility Study of a Rectangular CT Geometry for High Throughput Total-Body PET-CT",

[152] F. Muller et al., "Deep Learning enabled CT-less Attenuation and Scatter Correction for Multi-Tracer Whole-Body PET Imaging", *Journal of Nuclear Medicine*, vol. 65, no. supplement 2, pp. 241 351–241 351, Jun. 2024, ISSN: 0161-5505, 2159-662X.

[153] A. J. Reader and B. Pan, "AI for PET image reconstruction", *The British Journal of Radiology*, vol. 96, no. 1150, p. 20 230 292, Oct. 2023, ISSN: 0007-1285, 1748-880X. DOI: 10.1259/bjr.20230292.